



The
University
Of
Sheffield.

Characterising Contraction in a Tissue-Engineered
Buccal Mucosa Model with Raman Spectroscopy

By:

Marcela Garcia

Under the supervision of

Dr. Ihtesham ur Rehman

Prof. Sheila MacNeil

November 2018

A thesis submitted in partial fulfilment of the requirements for the degree of Doctor
of Philosophy.

Dedication

This thesis is dedicated to my family, to my best friend, and to my significant other:

- To my parents and brother for always supporting me in every step of the way. You guys are my world.
- To Daniela Lazaro for those scientific (and not so scientific) conversations, and for sharing endless discussions and ideas that would work out for the better of our projects. Raman gave me a best friend for life.
- To Nathan Kucko for his endless patience on dealing with my never-ending Raman stories and non-working experiments. For his good sense of humour when things were chaotic and for coming up with new terms such as: “don’t be reticulous”, and “don’t be a dRaman Queen”. God bless his soul.

To all of you, THANK YOU for being by my side and showing your support during these four years. It means the world to me.

Abstract

Graft contracture of tissue engineered buccal mucosa models has been monitored and characterised with Raman Spectroscopy. Tissue engineered buccal mucosa grafts have been used clinically for the reconstruction of head and neck cancer and for extraoral applications such as replacement of scarred tissue in the urethra. However, both in the laboratory and clinically, these 3D models exhibit contraction compromising the proper functionality of the surrounding tissues. Graft contraction continues to be a poorly understood clinical problem and what is needed ideally is a better understanding of the underlying biochemical mechanism behind contraction. Since studying collagen crosslinking biochemically is technically difficult, assays are tedious and not very reliable, Raman spectroscopy was elected as the technique of choice to characterise and monitor the process of contraction. In this research project, the process of contraction was characterised as a function of time before and after incorporation of β -APN drug. The use of multivariate analysis (MVA) techniques highlighted the increase of α -helix triple structure as a function of time and extent of crosslinking. A reduction of α -helix formation was also noticed after incorporation of β -APN drug and inhibition of contraction. Together with this, formation of β -sheet structure was also highlighted by the statistical analysis after inhibiting crosslinking of collagen fibres. Together with this, the amide III region was also identified as a biomarker for the progression of contraction in all three layers of the oral mucosa graft. A turnover of the $I_{1335}/I_{1245} \text{ cm}^{-1}$ doublet was noticed as crosslinking increased. No turnover was seen after incorporation of β -APN drug into the experiment. This region is representative of the peptidic bond of the polypeptide chains. Findings represent a stepping stone towards a better understanding behind the nature of this process. It opens up the possibility of considering the participation of these biomarkers, as a complementary route of collagen cross-linking progression, coupled with the important role that lysyl-oxidase (LOX) enzyme plays on it during the process of contraction.

Acknowledgements

I strongly appreciate and feel very grateful with:

Dr. Ihtesham ur Rehman and Prof. Sheila MacNeil for their constant support, help and guidance. Dr. Anthony Bullock for his constant encouragement and patience. Daniela Lazaro for the endless brainstorming about Raman spectroscopy, for encouraging and motivating me during this research project.

To both my research groups who helped me through the experiments. To Chris Hillary and Sabiniano Roman for their help when starting this project. To Ceyla Yorucu, Chandra Talari, Saad Quassim, David James and Thermo Scientific team who trained me and guide me through becoming a competent user in Raman Spectroscopy.

To everyone in KRI for making daily life such a nice and pleasant environment.

To Armourers and Brasiers for providing me with funding towards conferences and short courses.

Special gratitude towards CONACyT for its financial investment towards my PHD research.

Table of Contents

1	LITERATURE REVIEW	1
1.1	ORAL MUCOSA.....	2
1.1.1	ORAL EPITHELIUM.....	3
1.1.2	BASEMENT MEMBRANE.....	5
1.1.3	LAMINA PROPIA: EXTRACELLULAR MATRIX	6
1.1.3.1	THE COLLAGENOUS DOMAIN	8
1.1.3.2	THE NON-COLLAGENOUS DOMAIN.....	9
1.2	WOUND HEALING	13
1.3	RAMAN SPECTROSCOPY: THEORY AND PRINCIPLES	21
1.3.1	INSTRUMENTATION	25
1.4	RAMAN SPECTROSCOPY AND COLLAGEN STRUCTURE	30
1.5	SPECTRAL DATA ACQUISITION.....	30
1.6	CHARACTERISATION OF COLLAGEN MOLECULES USING RAMAN SPECTROSCOPY	35
1.7	STUDIES OF COLLAGEN CHANGES DUE TO PHYSIOLOGICAL PROCESSES.....	40
1.8	STUDIES OF COLLAGEN CHANGES DUE TO COLLAGEN MODIFICATION AND PROCESSING.....	55
1.9	STUDIES OF COLLAGEN CONTRACTION IN SKIN AND ORAL MUCOSA GRAFTS	50
1.10	SUMMARY.....	65
2	HYPOTHESIS.....	67
3	AIMS AND OBJECTIVES	67
4	MATERIALS AND METHODS	68
4.1	PRODUCTION OF A TEBM MODEL	68
4.1.1	ORAL BIOPSY	68

4.1.2	ISOLATION OF ORAL KERATINOCYTES	68
4.1.3	ISOLATION OF ORAL FIBROBLASTS.....	70
4.1.4	PREPARATION OF DE-EPIDERMISED DERMIS	71
4.1.5	PREPARATION OF TEBM MODEL.....	71
4.1.6	PREPARATION OF A TEBM MODEL WITH β -APN.....	73
4.1.6.1	PREPARATION OF β -APN STOCK SOLUTION.....	73
4.2	EXPERIMENTAL DESIGN	74
5	CHARACTERISATION OF CONTRACTION IN A TEBM MODEL	76
5.1	DIMENSIONAL ANALYSIS	76
5.2	TISSUE PROCESSING.....	79
5.3	HAEMATOXYLIN AND EOSIN STAINING	82
5.4	RAMAN SPECTROSCOPY	82
5.4.1	SPECTRAL PROFILES OF CONTRACTION	84
5.4.2	MULTIVARIATE ANALYSIS METHODS	85
6	RESULTS AND DISCUSSION	91
6.1	DIMENSIONAL ANALYSIS	92
6.2	HISTOLOGICAL ANALYSIS	95
6.3	RAMAN SPECTROSCOPY CHARACTERISATION	96
6.3.1	EPITHELIUM LAYER	97
6.3.2	PAPILLARY LAYER	110
6.3.3	RETICULAR LAYER.....	120
6.4	SUMMARY	128
7	CONTRACTION IN A TEBM MODEL WITH B-APN	130
7.1	RESULTS & DISCUSSION.....	130
7.1.1	DIMENSIONAL ANALYSIS	131
7.1.2	HISTOLOGICAL ANALYSIS	134
7.1.3	RAMAN SPECTROSCOPY CHARACTERISATION	135
7.1.3.1	EPITHELIUM LAYER.....	136
7.1.3.2	PAPILLARY AND RETICULAR LAYER	143

7.2	SUMMARY.....	158
8	CONCLUSION AND FUTURE WORK	159
9	APPENDIX.....	163
10	REFERENCES.....	179

List of Figures

FIGURE 1. HELICAL POLYPEPTIDE CHAIN OF COLLAGEN TYPE I MOLECULE.....	7
FIGURE 2. EXTENSIONS AT THE END OF THE COLLAGENOUS REGION PLAY AN IMPORTANT ROLE IN FACILITATING COLLAGEN MOLECULES TO STAGGER TOGETHER TO PRODUCE A COLLAGEN FIBRIL SINCE THEY CHEMICALLY CROSSLINK AND CAN BIND TO OTHER MOLECULES. ¹³	10
FIGURE 3. A FIBRE-LIKE STRUCTURE OF COLLAGEN TYPE I. A SCHEMATIC REPRESENTATION OF THREE DIFFERENT STRUCTURES TOWARDS THE FORMATION OF A COLLAGEN FIBRE [THIS FIGURE HAS BEEN ADAPTED FROM CANELÓ ET AL. ¹⁹]......	12
FIGURE 4. WOUND HEALING STAGES, INCLUDING IMPORTANT CELLS, GROWTH FACTORS AND PRO-INFLAMMATORY CYTOKINES PARTICIPATING IN THE PROCESS.....	20
FIGURE 5. SEQUENTIAL REPRESENTATION OF THE STAGES INVOLVED WOUND HEALING.	21
FIGURE 6. SCHEMATIC REPRESENTATION OF THE SCATTERING OUTCOMES IN RS. (ADAPTED FROM COLTHUP ET AL. 1990).....	23
FIGURE 7. SCHEMATIC REPRESENTATION OF THE THEORY AND INSTRUMENTATION OF RAMAN SPECTROSCOPY (ADAPTED FROM CORNELL).	27
FIGURE 8. RAMAN SPECTRA OF COLLAGEN STRUCTURE, AN AVERAGE OF 60 SPECTRA. THE THREE MAIN SPECTRAL REGIONS THAT FREQUENTLY REFLECT MAIN PEAKS INVOLVED IN CONFORMATIONAL CHANGES.	36
FIGURE 9. SCHEMATIC REPRESENTATION OF THE THREE MAIN STEPS TOWARDS PREPARING A TEBM MODEL..	73
FIGURE 10. SIX TEBM SAMPLES IN A SIX-WELL PLATE. EACH 3D SAMPLE IS REPRESENTING A TIME-INTERVAL.	75

FIGURE 11. EXPERIMENTAL DESIGN EXPLAINING HOW SAMPLES WERE REPRESENTING A SPECIFIC TIME POINT, AND HOW THEY WERE PHOTOGRAPHED EVERY TIME A TIME POINT WAS REACHED.....	77
FIGURE 12. MEASUREMENT OF THE SURFACE AREA WAS DONE WITH IMAGE J..	78
FIGURE 13. MEASURING CONTRACTION AS A FUNCTION OF TIME..	79
FIGURE 14. RAMAN CHARACTERISATION OF TEBM MODEL. TWENTY RANDOM POINTS COLLECTED PER LAYER PER SAMPLE (TIME POINT).....	84
FIGURE 15. SYSTEM TEMPLATE USED TO ORGANISE AND ANALYSE SPECTRAL DATA PER LAYER.....	88
FIGURE 16. COMPARISON TEMPLATE OF CONTROL TEBM VS TEBM/ β -APN MODEL. THIS SYSTEM CORRESPONDS TO THE ANALYSIS OF SPECTRAL DATA.....	89
FIGURE 17. EXPERIMENTAL DESIGN FOR RAMAN DATA WITH THE MAIN VARIABLES CONSIDERED FOR THE ANALYSIS OF THE SPECTRAL DATA. ..	90
FIGURE 18. DIGITAL IMAGE OF SAMPLE #4 SHOWING THE EXTENT OF CONTRACTION FROM THE STARTING POINT AT DAY 0 UP UNTIL DAY 14 OF <i>IN VITRO</i> CULTURE.....	92
FIGURE 19. PERCENTAGE OF REMAINING SURFACE AREA AS A FUNCTION OF TIME..	94
FIGURE 20. UNPAIRED T-TEST STATISTICAL ANALYSIS OF SURFACE AREA OF CONTROL MODEL AS A FUNCTION OF TIME.....	94
FIGURE 21. HISTOLOGICAL IMAGES (TAKEN WITH 20X OBJECTIVE) OF ALL FOUR TEBM MODELS.....	96
FIGURE 22. RAMAN CHARACTERISATION OF CONTRACTION IN THE EPITHELIUM LAYER AT DIFFERENT TIME POINTS.....	98
FIGURE 23. PCA OF LIPIDS REGION (3100-2600 CM^{-1}) AT THE INITIAL STAGE OF CONTRACTION..	101
FIGURE 24. PCA OF LIPIDS REGION (3100-2600 CM^{-1}) AT THE FINAL STAGE OF CONTRACTION..	101
FIGURE 25. A) PCA SCORE PLOT OF THE AMIDE I REGION: ACCORDING TO THE PCA ANALYSIS, SPECTRAL DATA FROM DAY 0 AND DAY 3 ARE MOSTLY SEPARATED BY PC-2 AND PC-4 LOADINGS.....	104

FIGURE 26. PCA SCORE PLOT OF THE AMIDE I REGION: ACCORDING TO THE PCA ANALYSIS, SPECTRAL DATA FROM DAY 3 AND DAY 7 ARE MOSTLY SEPARATED BY PC-2 AND PC-3.....	105
FIGURE 27. A) PCA SCORE PLOT OF THE AMIDE III REGION: ACCORDING TO THE PCA ANALYSIS, SPECTRAL DATA FROM DAY 0 AND DAY 3 ARE MOSTLY SEPARATED BY PEAKS AT 1336 AND 1245 CM^{-1}	107
FIGURE 28. CA OF AMIDE III REGION ON DAY 0 AND DAY 3 OF CONTRACTION IN A TEBM MODEL.....	108
FIGURE 29. A) PCA SCORE PLOT OF THE AMINO ACIDS REGION: ACCORDING TO THE PCA ANALYSIS, SPECTRAL DATA FROM DAY 0 AND DAY 3 ARE MOSTLY SEPARATED BY PEAKS AT 920 AND 873 CM^{-1}	110
FIGURE 30. RAMAN CHARACTERISATION OF CONTRACTION IN THE PAPILLARY LAYER AT DIFFERENT TIME POINTS.....	111
FIGURE 31. A) PCA SCORE PLOT OF THE AMIDE III REGION: ACCORDING TO THE PCA ANALYSIS, SPECTRAL DATA FROM DAY 0 AND DAY 3 ARE MOSTLY SEPARATED BY PEAKS AT 1274 AND 1244 CM^{-1}	115
FIGURE 32. A) PCA SCORE PLOT OF THE AMIDE III REGION: ACCORDING TO THE PCA ANALYSIS, SPECTRAL DATA FROM DAY 3 AND DAY 7 ARE MOSTLY SEPARATED BY PEAKS AT 1334 AND 1244 CM^{-1}	116
FIGURE 33. A) AMINO ACIDS REGION: PCA ANALYSIS, SPECTRAL DATA FROM DAY 3 AND DAY 7 ARE MOSTLY SEPARATED BY PEAKS AT 869 AND 854 CM^{-1}	118
FIGURE 34. CA OF AMIDE III REGION ON DAY 0 AND DAY 14 OF CONTRACTION IN A TEBM MODEL.....	119
FIGURE 35. RAMAN CHARACTERISATION OF CONTRACTION IN THE RETICULAR LAYER AT DIFFERENT TIME POINTS.....	121
FIGURE 36. A) PCA SCORE PLOT OF THE AMIDE I REGION: ACCORDING TO THE PCA ANALYSIS, SPECTRAL DATA FROM DAY 3 AND DAY 7 ARE MAINLY SEPARATED BY PEAKS AT 1655, 1613, AND 1606 CM^{-1}	123
FIGURE 37. PCA SCORE PLOT OF THE AMIDE II REGION: ACCORDING TO THE PCA ANALYSIS, SPECTRAL DATA FROM DAY 3 AND DAY 7 ARE MOSTLY SEPARATED BY PC-1 AND PC-2.....	125

FIGURE 38. A) PCA SCORE PLOT OF THE AMIDE III REGION: ACCORDING TO THE PCA ANALYSIS, SPECTRAL DATA FROM DAY 3 AND DAY 7 ARE MOSTLY SEPARATED BY PEAKS AT 1335 AND 1243 CM^{-1}	127
FIGURE 39: B-APN-CONTAINING TEBM MODEL. SAMPLE #4 SHOWING THE EXTENT OF CONTRACTION AT DAY 0, 3, 7 AND 14.....	132
FIGURE 40. REMAINING SURFACE AREA AS A FUNCTION OF TIME IN B-APN-CONTAINING TEBM MODELS.....	133
FIGURE 41. UNPAIRED T-TEST STATISTICAL ANALYSIS OF SURFACE AREA OF CONTROL VS DRUG MODEL AS A FUNCTION OF TIME.....	134
FIGURE 42. HISTOLOGICAL IMAGES OF B-APN-CONTAINING TEBM MODELS AT DIFFERENT TIME POINTS.	135
FIGURE 43. RAMAN CHARACTERISATION OF CONTRACTION IN A TEBM/B-APN MODELS IN THE EPITHELIUM LAYER AT DIFFERENT TIME POINTS..	137
FIGURE 44: A) PCA SCORE PLOT (LEFT) AND LOADINGS (RIGHT) OF THE 1510-1390 SPECTRAL REGION.	141
FIGURE 45. A) PCA SCORE PLOT (LEFT) AND LOADINGS (RIGHT) OF THE 1510-1390 SPECTRAL REGION..	142
FIGURE 46. PCA SCORE PLOT (LEFT) AND LOADINGS (RIGHT) OF THE 1800-1510 CM^{-1} SPECTRAL REGION IN THE PAPILLARY LAYER..	145
FIGURE 47. PCA SCORE PLOT (LEFT) AND LOADINGS (RIGHT) OF THE 1800-1510 CM^{-1} SPECTRAL REGION IN THE RETICULAR LAYER. A) PCA FOR DAY 7.).	148
FIGURE 48. PCA SCORE PLOT (LEFT) AND LOADINGS (RIGHT) OF THE 1390-1140 CM^{-1} SPECTRAL REGION IN THE PAPILLARY LAYER.	151
FIGURE 49. CA OF AMIDE III REGION ON DAY 7 OF CONTRACTION ON BOTH, TEBM & TEBM/B-APN MODEL.....	152
FIGURE 50. PCA SCORE PLOT (LEFT) AND LOADINGS (RIGHT) OF THE 1390-1140 CM^{-1} SPECTRAL REGION IN THE RETICULAR LAYER.....	153
FIGURE 51. PCA SCORE PLOT (LEFT) AND LOADINGS (RIGHT) OF THE 980-600 CM^{-1} SPECTRAL REGION IN THE PAPILLARY LAYER.....	156
FIGURE 52. PCA SCORE PLOT (LEFT) AND LOADINGS (RIGHT) OF THE 980-600 CM^{-1} SPECTRAL REGION IN THE RETICULAR LAYER.	157
FIGURE 53. PCA OF AMIDE III REGION IN THE EPITHELIUM LAYER.....	171

FIGURE 54. PCA OF AMIDE I REGION IN THE EPITHELIUM LAYER.	172
FIGURE 55. PCA OF AMINO ACIDS REGION IN THE EPITHELIUM LAYER	173
FIGURE 56. PCA OF AMIDE III REGION IN THE PAPILLARY LAYER.....	174
FIGURE 57. PCA OF AMINO ACIDS REGION IN THE PAPILLARY LAYER.	175
FIGURE 58. PCA OF AMIDE III REGION IN THE RETICULAR LAYER..	176
FIGURE 59. PCA OF AMINO ACIDS REGION IN THE RETICULAR LAYER.....	177
FIGURE 60. CA OF AMIDE III REGION ON DAY 3 OF CONTRACTION IN BOTH TEBM & TEBM/B-APN GROUPS.	178

List of Tables

TABLE 1. COMPARISON OF RAMAN SPECTROSCOPY METHODS AND ITS CURRENT APPLICATIONS	29
TABLE 2. STRATEGIES AND DIFFERENT ALGORITHMS COMMONLY USED FOR APPROPRIATE ANALYSIS OF SPECTRAL DATA.	33
TABLE 3. TECHNIQUES USED FOR COLLAGEN CHARACTERISATION	34
TABLE 4. MAIN SPECTRAL PEAKS THAT REFLECT CONFORMATIONAL CHANGES IN COLLAGEN STRUCTURE.	37
TABLE 5. EXAMPLES OF CLINICAL CONDITIONS ALTERING THE MOLECULAR STRUCTURE OF COLLAGEN.	45
TABLE 6. STUDIES ON CONTRACTION OF SKIN AND ORAL MUCOSA GRAFTS.....	55
TABLE 7. STEPS AND SCHEDULE FOR TISSUE PROCESSOR LEICA TP1020.....	80
TABLE 8. DEWAXING PROTOCOL FOR RAMAN SPECTROSCOPY BASED ON MIAN <i>ET AL.</i> 2014	81
TABLE 9. DEWAXING PROTOCOL FOR H&E STAINING	82
TABLE 10. RAMAN SPECTROSCOPY PARAMETER	83
TABLE 11. PERCENTAGE OF CONTRACTION IN A TEBM MODEL (AND ITS TRIPLICATES). THE AVERAGE REMAINING SURFACE AREA WAS CALCULATED BY INCLUDING ALL THE AVAILABLE MEASUREMENTS PER TIME POINT.....	93
TABLE 12. AVERAGE AND SD VALUES FOR THE REMAINING SURFACE AREA CALCULATED AT EACH TIME POINT IN A B-APN-CONTAINING TEBM MODEL.....	132

Abbreviations

Ag	Silver
AGE	Advanced Glycation End product
ALI	Air Liquid Interface
Au	Gold
β -APN	β -Amino propionitrile
BM	Basement Membrane
CA	Cluster Analysis
CCD	Charged Coupled Device
COL	Collagenous Region
DALY's	Disability adjusted life years
DED	De-epidermised Dermis
DEJ	Dermal Epidermal Junction
DEW	Diabetic Elderly Women
DMEM	Dulbeccos Modified Eagle's Medium
DMSO	Dimethyl Sulphoxide
DOPA	Di-Oxo-Phenylalanine
DPD	Deoxypyridinoline
DT	Difco Trypsin
D ₂ O	Deuterium Oxide
ECM	Extracellular Matrix
EDC	1-Ethyl-3-(3-Dymethylaminopropyl)
EGF	Epidermal Growth Factor

FACIT's	Fibrillar-Associated with Interrupted Triple-helix
FCS	Fetal Calf Serum
FGF	Fibroblast Growth Factor
FTIR	Fourier Transformed Infrared Spectroscopy
GA	Glutaraldehyde
Gly	Glycine
HEW	Healthy Elderly Women
HTA	Human Tissue Authority
Hyp	Hydroxyproline
HYW	Healthy Young Women
H&E	Haematoxylin and Eosin
IGF	Insulin-like Growth Factor
IMS	Industrial Methylated Spirits
LOX	Lysyl Oxidase Enzyme
LTQ	Lysyl-Tyrosyl-Quinone
LWD	Long Work Distance
MMP	Matrix-Metalloproteinase
MVA	Multivariate Analysis
NC	Non-Collagenous
NHS	N-HydroxySuccinimide
O.F.	Oral Fibroblasts
O.K.	Oral Keratinocytes
PBS	Phosphate Buffer Saline

PC	Principal Component
PCA	Principal Component Analysis
PDGF	Platelet-Derived Growth Factor
Phe	Phenylalanine
Prl	Pyrrole
PYD	Pyridinoline
REC's	Research Ethics Committee's
RH	Relative Humidity
RS	Raman Spectroscopy
SERS	Surface-Enhance Raman Spectroscopy
TEBM	Tissue-Engineering Buccal Mucosa
TG	Triglycerides
TGF-B	Transforming Growth Factor Beta
TNF	Tumour Necrosis Factor
VEGF	Vascular Endothelial Growth Factor
WHO	World Health Organisation



INTRODUCTION & LITERATURE REVIEW

1 LITERATURE REVIEW

Due to their versatility, tissue-engineered buccal mucosa grafts have been used not only for intraoral applications –to repair cleft palates or for reconstructive surgery in head and neck cancer- but also in extraoral applications to replace scarred tissue in the urethra. However, when applied clinically in the patient, tissue-engineered buccal mucosa grafts exhibit contraction and at some point can undergo fibrosis down the line that can lead to incorrect functionality of the tissue. These contractions and fibrosis of the oral mucosa graft continue to develop after it has been implanted at the injury site, resulting in approximately 40% of contraction after just 1 month. Recent studies in skin and oral mucosa have shown that this contraction might be a result of the cross-linking of collagen primarily induced by keratinocytes. To tackle this problem, pharmaceutical agents have been applied to oral mucosa grafts in order to reduce contraction, β -APN being the most common. Although, while it may be true that these drugs can significantly reduce the extent of contraction, their biochemical pathway and interaction with the collagen cross-linking remains unclear. Having a clear understanding of the mechanism behind contraction at the cellular level and the effects of potential drug candidates to reduce this phenomenon is of utmost importance. Currently, there is no method available to accurately measure the crosslinking of collagen at the biochemical level, as conventional assays are tedious and not very reliable (Electrochemiluminescence ECLIA to indirectly measured collagen synthesis



INTRODUCTION & LITERATURE REVIEW

through the concentration of amino terminal propeptide of type I (P1NP), and Sircol soluble collagen assay). Raman spectroscopy offers a feasible alternative to overcome these limitations. This technique has already established a spectral profile of particular bonds in the collagen molecule. Therefore, it can easily identify biochemical differences occurring in the collagen molecule at different stages of contraction. The use of vibrational spectroscopy would be of great help when analysing the different degrees of contraction in order to establish a database of the natural phenomenon of contraction. Once this is done, it would be interesting to analyse the biochemical pathway and interaction of β -APN with collagen molecules and to relate each spectral profile to the different extents of contraction.

1.1 ORAL MUCOSA

The oral mucosa is a tissue of the mucous membrane family. In general, the mucous membrane is a moist tissue lining all cavities within the human body. In the oral cavity, this moisture mucous lining is also known as oral mucosa and is responsible for protecting all internal tissues inside the mouth by acting as a barrier and preventing them from being exposed to the exterior environment.¹

Oral mucosa is formed of two main layers, (i) the oral epithelium and (ii) the lamina propia or connective tissue. According to the region, oral mucosa can be connected or adhered to deeper structures through a loose connective tissue known as the submucosa.² These three layers of the oral mucosa closely



INTRODUCTION & LITERATURE REVIEW

resemble the anatomy of skin, where the oral epithelium corresponds to the epidermis, the lamina propria to the dermal layer and the submucosa to the hypodermis.

While it may be true that the oral mucosa is mainly formed of three general layers, this lining membrane also exhibits some histological alterations depending upon its location within the oral cavity. For instance, the oral mucosa that lines both maxillaries is known as the masticatory mucosa. Exposure to continuous friction due to chewing forces stimulates the mucosa to develop structural variations in order to withstand these mechanical forces.³ Thus, a keratinised layer on the uppermost layer of the oral epithelium is formed.

On the other hand, lining mucosa is barely exposed to mechanical forces, thus being characterised by a non-keratinised epithelium. Exposure to only mild forces makes this type of mucosa more flexible and distensible, rendering it easier to adjust to any movement caused by deeper structures. Since the lining mucosa is found to be covering everywhere else apart from the masticatory and specialised region, it represents 60% of the oral mucosa within the oral cavity.¹ Therefore, this is the type of oral mucosa that will be further discussed in this report.

1.1.1 ORAL EPITHELIUM

Non-keratinised oral epithelium is the outermost tissue and the first barrier against the oral environment. As every tissue, the oral epithelium is formed by



INTRODUCTION & LITERATURE REVIEW

a group of cells working in a coordinated manner and organised in four different layers:

Stratum basale layer is the boundary between the lamina propia and the epithelium layers. It is formed by cuboidal squamous epithelial cells tightly packed and uniformly distributed along the basement membrane, attaching to the latter one by a link between hemidesmosomes and laminins. Usually one to two cells thick, keratinocytes in this layer originate from a stem cell population that have a high proliferative capacity. When keratinocytes are meant to differentiate, a transformation in their anatomical structure takes place, resulting in the detachment of their hemidesmosomes, the ending of their cell division capacity and thus their migration to the outermost layers.⁴

Stratum spinosum layer is formed by all keratinocytes that have migrated towards the uppermost layers. Usually a few cells thick and adopting a spinous morphology, these cells start exhibiting a significant eosinophilic cytoplasm and a considerable reduction of their nucleus as they start progressing to the outermost layers.⁵

Intermediate layer is where cell's morphology is no longer spinous, and they lack the capacity for producing keratin. Keratohyaline granules are hardly present and keratin filaments are randomly distributed in between the epithelial cells. By forming a network within the intermediate layer, keratin filaments



INTRODUCTION & LITERATURE REVIEW

anchor to desmosomes keeping cells closely attached side-by-side and hence transmitting tensile strength to the epithelium.

Superficial layer is the uppermost layer of the non-keratinised epithelium. Lacking stratum granulosm and stratum corneum, the superficial layer allows the epithelium to be pliable and able to withstand both shielding and tensile forces.⁶

1.1.2 BASEMENT MEMBRANE

Also known as the basal lamina, the basement membrane is a corrugated layer connecting both the epithelium and lamina propia. The corrugated-like shape increases the surface area and leads to the formation of what is known as rete ridges. The uppermost region of the lamina propia interlaces between the multiple ridges increasing the area of attachment along the epithelium and connective tissue.⁷ Since the epithelium has no capillary vessels, attachment to the lamina propia allows the epithelium to receive enough nutrients from the bloodstream in order to continue functioning. The basement membrane mainly comprises of two parts:

Lamina lucida: the layer where basal cells get attached through hemidesmosomes. It also contains a high number of glycoproteins and anchoring filaments that go through it trespassing the lamina lucida as opposed to hemidesmosomes.



INTRODUCTION & LITERATURE REVIEW

Lamina densa: underlies and supports the lamina lucida. It contains loops of anchoring fibrils made of collagen type VII, in which collagen type I and III go throughout the tissue interlinking to the lamina densa creating a flexible loose connection.⁸ Laminin and collagen type IV are also present in lamina densa.

1.1.3 LAMINA PROPIA: EXTRACELLULAR MATRIX

All connective tissues are composed of two main components, (i) resident cells and an (ii) extracellular matrix (ECM) structure.

Cells living in the connective tissue are responsible for their own synthesis and preservation. They ensure their maintenance by producing an ECM structure, which mainly consists of different types of secreted proteins working in a highly organised and coordinated manner. The ECM is not only produced to give structural support to resident cells but also to provide both mechanical and biochemical properties to the connective tissue in general.⁹

As mentioned before, there are different types of proteins forming the ECM, with collagen being the most abundant and main constituent of the connective tissue⁶). As a protein, collagen is a macromolecule comprised of several amino acids acting as building blocks to form a polymer chain. Polymerisation of amino acids takes place through a condensation reaction resulting in a polypeptide chain and a molecule of water as a by-product. The amino group (NH₂) of amino acid A binds to the carboxyl group (COOH) of amino acid B resulting in the formation of an amide bond (O=C-NH), also known as a peptide

bond. A protein containing more than three amino acids (i.e. more than three peptide bonds) is considered a polypeptide chain.¹⁰

This macromolecule is a protein comprising mainly of repetitive proline-rich tripeptide domains in which the three main amino acids are glycine, proline and hydroxyproline (Gly-X-Y).¹⁰ These tripeptide domains then polymerise together and form a long polypeptide chain. If this is the case, the C=O group of residue A binds to the NH group of the residue C leading to the formation of a right-handed helical polypeptide chain **Figure 1**.

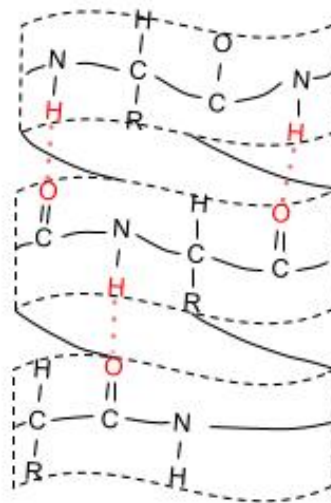


Figure 1. Helical polypeptide chain of collagen type I molecule. The C=O group of residue A binds to the NH group of residue C, resulting in the formation of a helical polypeptide chain. [This figure has been adapted from Rashid et al.¹¹]

Subsequently, three α -polypeptide chains become wound together forming a triple helical structure of collagen resulting in a fibre-like structure. It is this fibre-like structure that makes it easy for collagen to produce a highly

interconnected network throughout the ECM, contributing to the structural integrity and biochemical properties of the connective tissue.¹²

1.1.3.1 THE COLLAGENOUS DOMAIN

The term collagenous is assigned to any protein that is composed of a triple helical structure derived from three polypeptide chains coiled up together to form a right-handed triple helix structure, irrespective of the type of collagen molecule.¹²

Having a glycine residue at every third position along the polypeptide chain is the main prerequisite for this helix structure to be formed.⁹ Glycine is the smallest amino acid; its side group is only formed by a hydrogen atom, which occupies little to no space when compared to the side groups of other amino acids. Hence, glycine residues are positioned towards the centre of the triple helix, placing the bulkier side groups on the outside and thus keeping the structure tightly packed around a central axis.¹⁰

In order to stabilise the triple helical molecule, different amino acids, such as, proline or lysine can undergo hydroxylation due to enzymatic activity.⁹ Derived amino acids like hydroxyproline and hydroxylysine can then make intramolecular bonds with the hydrogen atom of glycine resulting in a chemically bonded triple helical molecule.¹⁰ Collagen molecules can measure

approximately 1.5 nm in diameter and around 300 nm in length, containing around 1000 amino acids in total.¹³

Finally, it should be noted that while it may be true that all collagen molecules contain at least one collagenous domain within its structure, non-collagenous motifs also play an important role in the conformation of each molecule. Thus, every collagen molecule is mainly composed of both collagenous (COL) and non-collagenous (NC) domains.

1.1.3.2 THE NON-COLLAGENOUS DOMAIN.

Apart from the triple-helix structure, a collagen molecule will also contain non-collagenous domains, which also play an important role in the structural properties of tissues. The C-propeptide region, for instance, is the non-collagenous domain located at one end of the triple helical structure. It is known as NC1 and strongly induces the formation of the triple helix structure.¹³ At the other end, the N-propeptide domain, also referred as NC2, is responsible for regulating the fibril diameters. When synthesising a collagen molecule, these non-collagenous domains are part of the procollagen structure, a precursor of the collagen molecule. However, to convert procollagen into a mature and functional collagen molecule, proteolytical cleavage of both C- and N-propeptide sections are required to take place. This cleavage leads to the formation of non-collagenous domains at both ends of the triple-helical structure that are referred to as C- and N- telopeptides.¹³

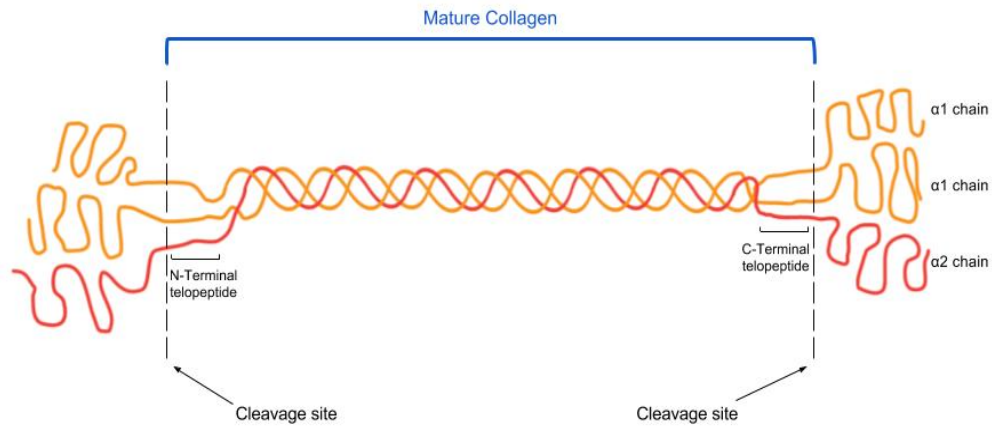


Figure 2. Extensions at the end of the collagenous region play an important role in facilitating collagen molecules to stagger together to produce a collagen fibril since they chemically crosslink and can bind to other molecules.¹³

As mentioned in the previous section, a collagen molecule is composed of both COL and NC domains. Biomechanical properties and classification of collagen molecules are dependent upon both the length and quantity of these domains.¹⁴ For instance, collagen type I, II and III all contain a long triple helical region with short NC domains at both ends. Due to their standard structure, they tend to form collagen fibrils that range between 10 to several hundred nanometres in diameter, causing them to be classified as fibril-forming collagens.¹⁵ In contrast, collagen IV and VII both contain a short triple helical structure interrupted by NC domains, where different molecules link together forming a network structure.¹⁶ These particular features allocate both collagen IV and VII in the network formation group.¹³

To date, 26 different types of collagen have been identified and classified into different groups depending on their supramolecular organisation and main structure.¹⁶ Some of the more common classification groups for collagen are fibril-forming, fibrillar-associated with interrupted triple-helix (FACITs), basement membrane and finally network-forming collagens. Fibril-forming collagens comprise collagen types I, II, III, V and XI. They generally measure between 10 to 300 nm in diameter and are produced by the connection of multiple collagen molecules in a specific ‘quarter stagger’ structure.^{17,18} More specifically, they exhibit a specific striation feature every 67 nm as one-quarter of each molecule is overlapped and staggered into another collagen molecule from a different row, as illustrated in **Figure 3**. Collagen fibrils can also assemble between one another to produce a collagen fibre, which is a few micrometres in diameter. Collagen type I and III are usually found together in several different tissues such as skin, cornea and lamina propria of the oral mucosa.¹³

The basement membrane collagen group consists of collagen type IV and VII. When compared to the fibrillar forming collagen, collagen IV and VII are significantly longer in length. They exhibit a few discontinuities within the COL domain, which leads to the formation of NC domains instead. However, in these two types of collagens, the N-terminal extension is referred as 7S domains while the C-terminal extension is referred to as NC1 domains. Both regions strongly induce crosslinking of different molecules. Collagen type IV and VII are usually found together in the basement membrane of the oral mucosa and skin forming

a network structure. In fact, collagen type IV links with three other molecules through their 7S domains, meaning that the crosslinking of multiple tropocollagens is possible through disulphide bonds.¹⁹

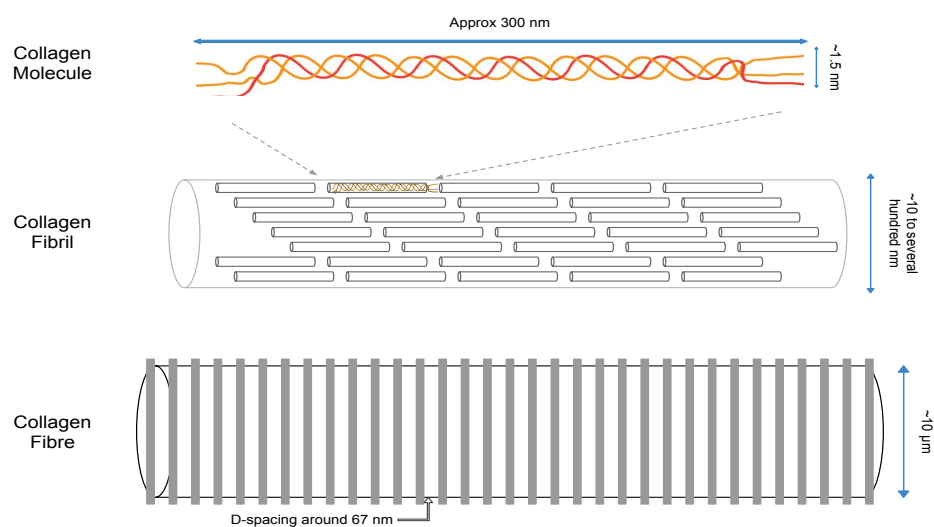


Figure 3. A schematic representation of the structure of fibre-like structure of collagen type c I across length scales. Three different structures towards the formation of a collagen fibre [This figure has been adapted from Caneló et al.²⁰].

While it is true that several techniques exist that can characterise collagen molecule, only a few can analyse the molecular alterations in collagen. It is also true that these techniques require a labelling agent and are destructive to the sample being analysed. Raman spectroscopy is a label-free and non-invasive technique that can probe into the sample and interact with the molecules, which allows for specific information about the sample integrity.²¹ Further, this spectroscopic technique allows the analysis of molecules in an aqueous solution, significantly broadening the applicability of Raman to a wide range of samples.

The aforementioned characteristic is unique in the sense that it gives Raman spectroscopy more of an advantage over Fourier-Transform Infrared (FTIR) and other spectroscopic techniques, which cannot analyse samples in an aqueous solution. Plus, there are certain vibrational modes that are active and detectable with Raman spectroscopy but not with FTIR. This only applies for symmetrical molecules, which can go through a change in polarizability but will lack the presence of a dipole since the vibration is symmetric around the central atom.²² Therefore, Raman spectroscopy has been widely used to characterise different types of collagen structures. Some studies have used pure collagen, more specifically collagen type I, IV²³ and VII²⁴, to establish a spectral profile that is unique to each molecule. Other studies have analysed biochemical changes in collagen molecules from different sites of the human body including collagen modification in eyes²⁵, breasts²⁶⁻²⁷, lungs²⁸, skin²⁹ and epithelium.³⁰ However, with respect to collagen crosslinking there is little known about utilising Raman spectroscopy to analyse this in soft tissues. Crosslinking of collagen fibres occurs during wound contraction as a normal physiological phenomenon during the wound healing process. It is believed that wound healing process plays a role in contraction of both skin and oral mucosa in vitro models, which is why a comprehensive description of the whole process is described below.

1.2 WOUND HEALING

Injury of soft tissue is often comprised of (i) cell death at the injury site, (ii) loss of the extracellular matrix integrity and (iii) disruption of blood vessels

continuity.¹⁰ These three scenarios lead to the formation of a wound, which in response the body activates a set of different biochemical stages that represents an overall of the wound healing process. These interdependent phases work in a coordinated manner and overlap in time resulting in the formation of new tissue and hence wound closure.

Within the wound healing process there are different stages that can be explained individually for an easier understanding, and can refer to in **Figure 4** and **Figure 5**.

Haemostasis Stage. When blood vessels are damaged, blood coagulation process is initiated as a defensive mechanism and so platelets will transport to the wound through the circulatory system. A blood clot, made of fibrin and blood cells is formed at the injury site to (i) protect the wound site from the exterior and (ii) act as a temporary matrix network so cells can adhere and migrate through it.¹⁰ At the same time, platelets will induce migration of inflammatory leukocytes by releasing both transforming growth factor-beta (TGF- β) and platelet-derived growth factor (PDGF).^{31,32} These two chemical mediators not only act as chemo attractants but also as mitogens and motogens to induce tissue-specific cells reproduction and proliferation, respectively.^{33,10}

Inflammatory Stage. While platelets continue to release many other growth factors, migration of leukocytes to the injury site initiates the inflammatory stage. Neutrophils and macrophages remove the remnants of damaged tissue



INTRODUCTION & LITERATURE REVIEW

from the wound site -including dead cells, cellular debris and any other foreign particle such as bacteria- by phagocytosis.

Apart from cleaning the injury site, leukocytes play an important role in promoting cell proliferation. Macrophages for instance, attract fibroblast to the wound site by the released of specific growth factors such as PDGF and fibroblast growth factor (FGF) (both known to be not only chemo attractants but also mitogens of fibroblast cells).^{10,34} Additionally, neutrophils attract tumour necrosis factor (TNF) and monocytes by releasing specific chemical mediators such as cytokines (e.g. interleukin-1). Thus, by providing chemical stimuli at the injury site, the cell proliferation stage gets initiated.

Cell Proliferation Stage. With new cells invading the injury site, a significant amount of growth factors are released by different cells in a simultaneously manner. To balance the excess of chemical mediators at the injury site, proteolytic proteins eliminate growth factors that were initially released by platelets at this stage of the wound healing process. Hence, the remaining growth factors being an important part of the cell proliferation stage are (i) FGF, (ii) insulin-like growth factor (IGF), (iii) epidermal growth factor (EGF), and (iv) vascular endothelial growth factor (VEGF).¹⁰

Since chemical mediators induce cell migration and proliferation to the injury site, they are known to be the way of communication between cells and their



INTRODUCTION & LITERATURE REVIEW

external environment. Chemical signals from growth factors and cytokines interact with the cell resulting in the manifestation of receptors at the cell membrane.³⁴ These cell adhesion molecules or so-called receptors, are usually proteins playing an essential role in cell migration as they served as a link between the cells and their surroundings. Integrins is one of the most important proteins when referring to cell migration.

As mentioned before, the wound healing process as well as any other mechanism within the human body are a series of coordinated processes that work in a highly organized manner. When cells need to attach to the fibrin and fibronectin network, the adhesive domains within this mesh are upregulated rendering easier for integrins -located at the cell membrane- to attach³⁵. Hence, one extreme of the integrin molecule is linked to the fibrin domain while the other extreme is connected to the interior of the cell. A balanced adhesion-strength is ideal as a weak adhesion to matrix proteins would not withstand forces caused by cells during migratory movement and a strong adhesion might impede migration of cells through the fibrin mesh.³⁶ To facilitate migration of cells even more, different proteases such as MMPs, collagenase and serum-derived plasmin are abundant at the wound site, in particular wound edges. Attachment of proteases to cell-membrane receptors allows cells to pass through the fibrin mesh by cleaving the protein-based structures.³⁵

Production of ECM. The formation of the ECM is a controlled process regulated by both (i) extracellular matrix cells and (ii) growth factors. For instance, while remnants of matrix proteins are being cleaved by specific proteases, cells at wound edges are replacing them with new matrix proteins. However, in order for cells to reach the centre of the wound, EGF is released to stimulate the fabrication of fibronectin.³⁷ Once the adhesive protein is synthesised all over the injury site, cells start migrating inward for wound closure. When fibroblasts interact with a TGF- β , synthesis of glycosaminoglycan, collagen and fibronectin take place. The production of extracellular matrix proteins leads to an accumulation of collagen from the edge of the wound inward.^{10,34}

Neovascularization Stage. As expected from any living organism, cells need oxygen and nutrients to properly function. Hence, vascularisation supply to the newly formed extracellular matrix wound bed is up most important. A significant amount of cells and growth factors are concentrated in the extracellular matrix milieu. In a hypoxic atmosphere, macrophages and endothelial cells produce both FGF and VEGF's.³⁸ Release of these specific chemical mediators enhances the synthesis of new capillaries into the newly formed ECM wound bed. Once the wound site is all covered with new tissue, angiogenesis stage is concluded.

Granulation Tissue Stage. In conjunction with cells and extracellular matrix milieu, neovascularization of the wound site gives the injury site a pink granular appearance. As a result to the formation of new capillaries, cell activity as well as other components such as proteins are significantly increased. Proteoglycans, collagens and many other growth factors are expressed at this stage of the wound healing process. Towards the end of the granulation process, wound contraction occurs due to compression of the ECM. While it may be true that the mechanism behind this situation remains unclear, it has been established that fibroblasts develop a myofibroblast phenotype with integrin receptors on their membranes.³⁹ By binding to matrix proteins like collagen, the actin-rich cytoskeleton of these cells exerts a contractile force to pull the collagen fibres together leading to wound contraction.³⁶

Remodelling Stage. Once myofibroblasts have forced a connection between themselves, margins of the wound site are finally drawn together. Myofibroblasts are no longer needed after wound contraction and thus, apoptosis of these cells occurs resulting in the initiation of remodelling phase⁴⁰

At this stage during the wound healing process, a significant amount of collagen fibres, among other proteins, are accumulated at the granulation tissue. As part of the remodelling stage, collagen fibres arrangement is altered in different ways. For instance, regulation of collagen synthesis and collagen degradation takes place, allowing the organism to produce as many collagen fibres



INTRODUCTION & LITERATURE REVIEW

(specialised to each tissue) as needed.³⁸ MMP's are the proteolytic enzymes responsible for collagen degradation at the wound site.

One of the mechanisms of wound healing is for the edges of the wound to try to close in what has been described as a purse string effect. In loose skinned animals like cats and dogs this skin slides over the underlying fat and muscle and this works very well to rapidly reduce the area of the wound. However human skin anatomy is different than the anatomy from animal skin, and in humans' skin is connected to the underlying connective tissue and muscle. Accordingly, the same mechanism contraction pulls on the underlying tissues. This is seen to the greatest extent when skin grafts are used to restore barrier function in badly burned patients. These grafts quite often contract and fibrose to the extent that they can severely limit joint movement if grafts are placed over joints. This loss in mobility as well as the poor aesthetic outcome can quite often result in later secondary reconstructive surgery. While a significant amount of research has been devoted to this phenomenon, a better understanding of the biochemical pathway of contraction in soft tissue remains unclear

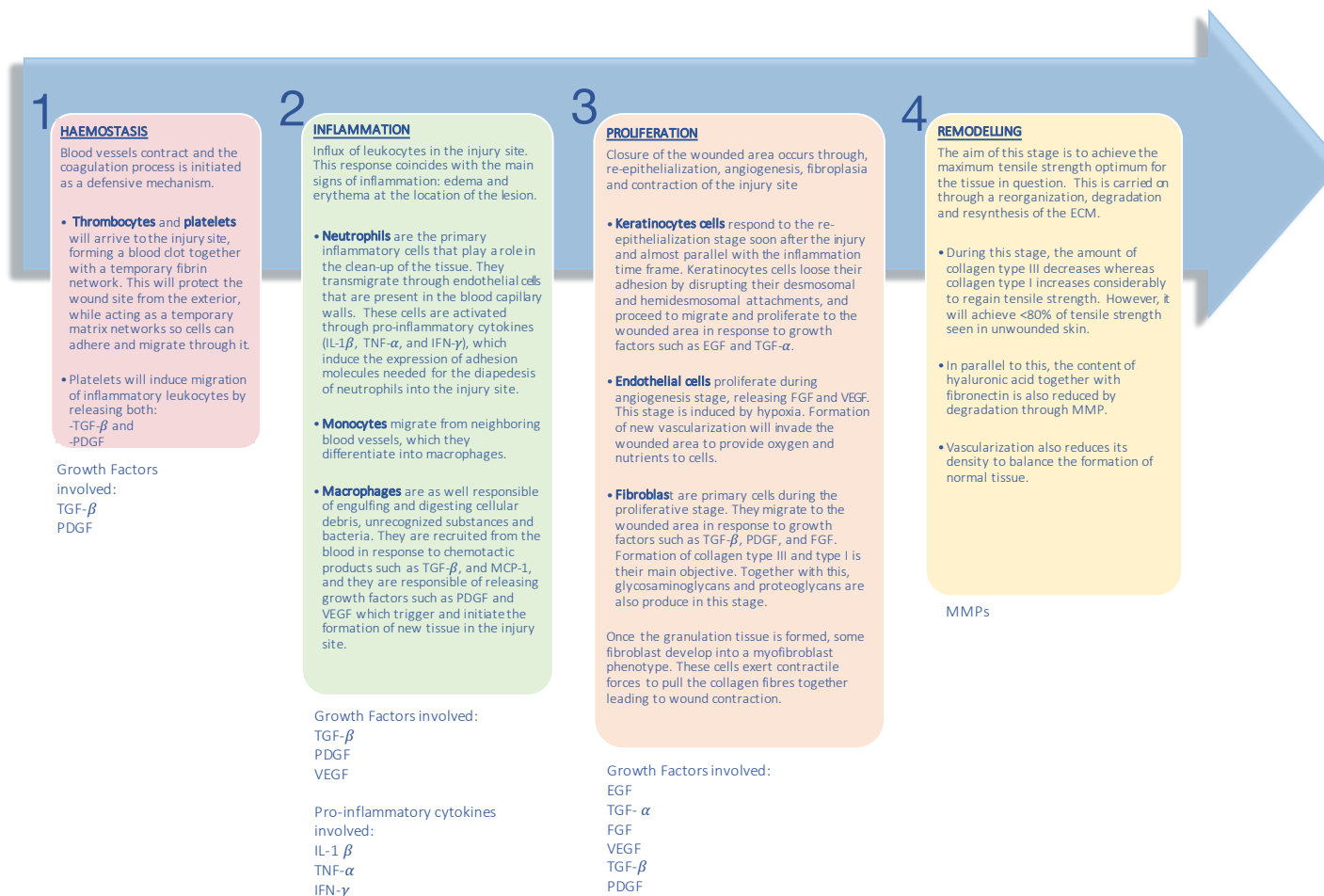


Figure 4. Wound healing stages, including important cells, growth factors and pro-inflammatory cytokines participating in the process.^{41,42,31}

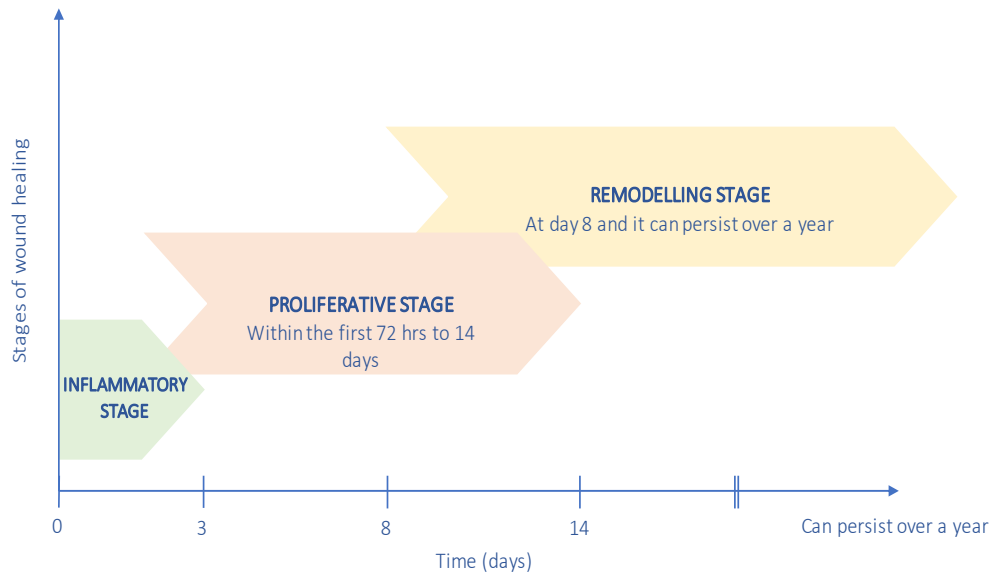


Figure 5. Sequential representation of the stages involved wound healing.^{35,41}

This literature review looks at a compilation of studies where Raman spectroscopy has been widely used to study the molecular alterations of collagen found in soft and hard tissues. This technique has been used to study collagen crosslinking as part of the mineralisation process of bone.

1.3 RAMAN SPECTROSCOPY: THEORY AND PRINCIPLES

A photon can be defined as the quantum of light. In Latin, “quantum” means the smallest amount of physical energy that can stand independently as a unit of matter. Therefore, a photon is the fundamental unit of energy conforming light.

The natural essence of light, as a form of electromagnetic radiation, is to travel throughout space in form of electromagnetic waves. These waves keep a



INTRODUCTION & LITERATURE REVIEW

constant distance between each other's crest and this distance is known as the wavelength and it is measured in nanometers (nm). The longer the distance between each crest the longer the wavelength and thus, the lower the frequency.

There are several sources emitting energy towards the space. However, each of these sources will emit electromagnetic radiation at a specific constant wavelength. For instance, visible light will always travel within a wavelength range of 400 to 700 nm, whereas X-rays will travel in a wavelength between 0.1 and 10 nm. The different sources of electromagnetic radiation and their corresponding wavelength conforms the wide range of what it is known as the spectrum of light.

RS is a technique that employs monochromatic light within the visible range (400 to 700 nm) of the electromagnetic spectrum.⁴³ This means that the wavelength and frequency of the electromagnetic source remains constant while shooting a monochromatic incident laser beam towards the sample. After interacting with the sample, radiation can induce the vibration of chemical bonds that will be expressed as single peaks in the Raman spectrum.⁴⁴ Peaks will reflect in different ways according to the type of vibration taking place. A chemical bond can vibrate in six different ways: symmetric and asymmetric stretching, rocking, twisting, scissoring and wagging.

When in room temperature, almost all electrons from the molecules are found to be in their lowest energy state,²² this lowest point of energy within the

electron cloud is also known as **ground state**. When the incident beam is shooting towards the sample, photons will interact with molecules making electrons go from the ground state to a higher level of energy. During this interaction between energy and electrons three possible outcomes can take place, according to **Figure 6**.

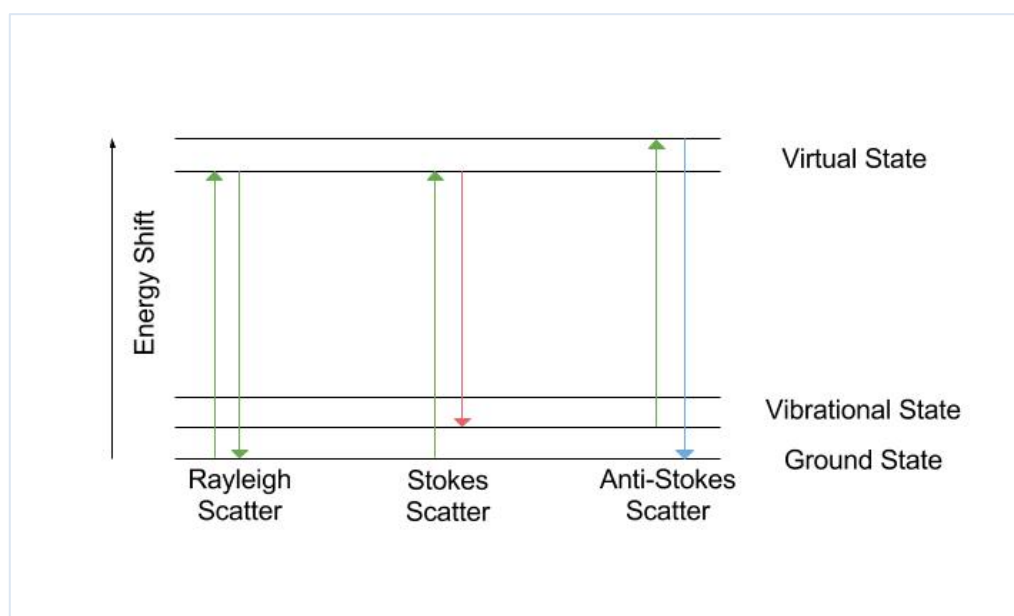


Figure 6. Schematic Representation of the Scattering Outcomes in RS. (Adapted from Colthup et al. 1990)

If the electron goes back to its original state, the photon will transfer back into the laser beam and thus the wavelength and frequency of the scattered beam will remain the same as in the incident beam. This is known as the **Rayleigh effect** or elastic scattering.⁴⁴ Since only one in one billion photons interacts with the electron cloud of the molecule, most photons have no impact on the energy

levels of electrons making this effect the most common outcome.⁴⁵ This can be understood as follow:

Rayleigh Effect:

$$V_{\text{Incident beam}} = V_{\text{Scattered beam}}$$

Since the electron is such a light particle, the interaction between the photon and the electron in the molecule is quite subtle. Still if the photon has an impact in the energy state of the electron, the scattered beam will have a notorious gain or loss of energy that will immediately reflect in a change of both frequency and wavelength of the scattered radiation, leading to a subtle change in colour of the scattered laser beam.⁴⁵ This phenomenon is known as **Raman shift** or inelastic radiation, which pertains to the difference in energy between the scattered and the incident beam as a result to the gain or loss of energy in the electron⁴⁴. It can be understood as follow:

Raman Effect:

$$V_{\text{Incident beam}} \neq V_{\text{Scattered beam}}$$

This effect comprises two remaining possible outcomes. If after interacting with the photon, the electron goes down to an energy level lower than that of the initial state, a transfer of energy into the scattered photon has occurred.⁴⁶ The scattered beam has more energy now than the incident beam, which will immediately reflect in an increased of frequency and thus shorter wavelength

leading to a change in colour of the scattered laser beam.⁴⁴ This is known as **Anti-Stoke shift** or blue shifting and can be represented as follow:

Anti-Stoke Shift:

$$\text{Energy}_{\text{Final vibrational level}} - \text{Energy}_{\text{Initial vibrational level}} = X_{\text{Energy transferred}}$$

$$V_{\text{Incident beam}} + X_{\text{Energy transferred}} = V_{\text{Scattered beam}} > V_{\text{Incident beam}}$$

In the contrary, if when interacting with the electron, the photon transfers energy into the molecule, electrons will go down to an energy level higher than the ground state. The loss of energy from the scattered beam entails the elongation of the wavelength and hence a decrease in frequency. This is known as **Stokes shift** or red shifting⁴⁴ and can be presented as follow:

Stokes Shift:

$$V_{\text{Incident beam}} - X_{\text{Energy transferred}} = V_{\text{Scattered beam}} < V_{\text{Incident beam}}$$

Stoke shifts are way more common than anti-stoke shifts when in room temperature since almost all molecules are expected to be in their ground state. Therefore, after interacting with the photon, the number of electrons being excited to an energy level higher than the ground state is significantly higher.

1.3.1 INSTRUMENTATION

The most common instrument setup used in Raman spectroscopy is the Charged Coupled Device (CCD) based dispersive spectrometer. A schematic

representation of this setup is shown in **Figure 7**. The laser line is directed into the spectrometer towards the beam expander increasing its diameter in relation to the magnification of the objective being selected. The now expanded beam is then reflected off from strategically placed mirrors to an optical filter and from there directed towards the sample. Once the incident beam interacts with the sample, the scattered radiation is reflected into the spectrometer and is directed towards the optical filters.⁴⁷ As mentioned before, almost all of the scattered radiation contains the same frequency and wavelength as in the incident beam. Entailing a significantly higher intensity of Rayleigh scatter when compared to Raman scatter; as only a small fraction of the scattered radiation pertains to the Raman effect. Therefore, it is upmost importance to remove Rayleigh signals from the scattered radiation, as high intensities would mask the Raman signal in the spectrum rendering it impossible to be analysed.

As part of the instrumentation, Raman spectroscopy utilises two types of filters to separate Rayleigh from Raman scattering:

Notch Filter: It separates Rayleigh scattering from Raman scattering by absorbing the laser line wavelength. This filter allows all wavelengths (Stokes and Anti-Stokes signals) outside the laser line range to pass through towards the detector.

Edge Filters: It retains all wavelengths within a specific threshold region, including the laser line wavelength. One of the edges might be considerably

close to the Rayleigh wavelength. This filter only transmits one type of Raman scattering, either Stokes or Anti-Stokes. Stokes signal (longer wavelength) requires long band pass filter, and Anti-Stokes signal (shorter wavelength) requires a short band pass filter.

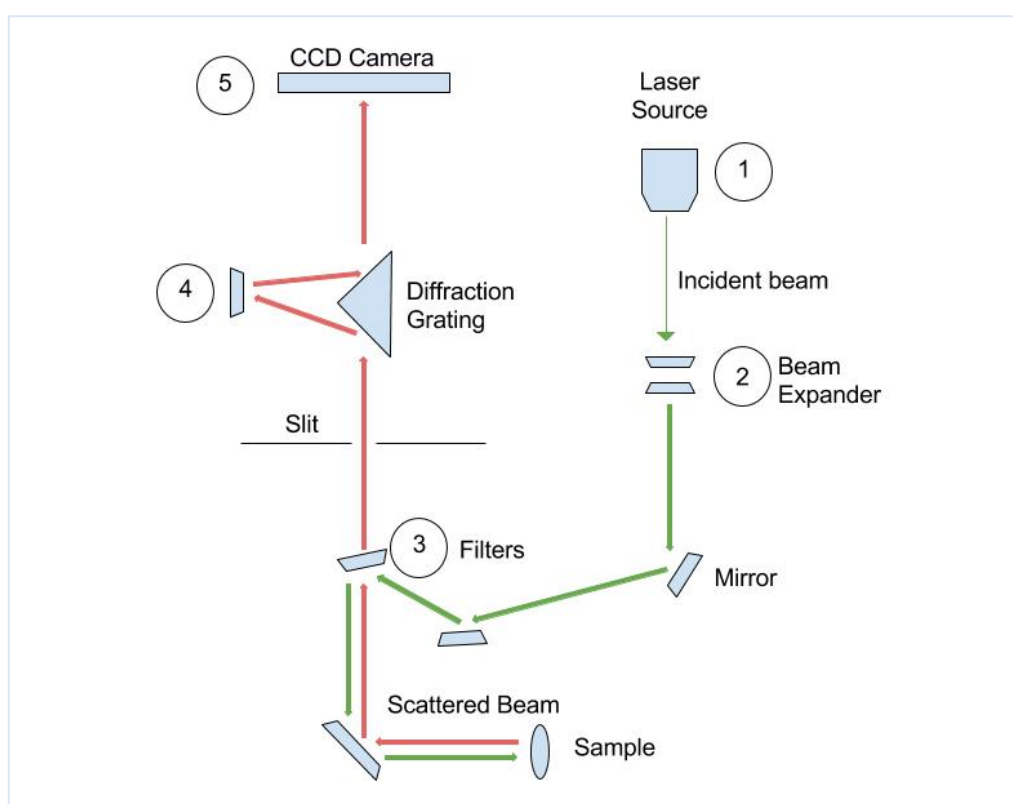


Figure 7. Schematic Representation of the Theory and Instrumentation of Raman Spectroscopy (Adapted from Cornell).

The entire scattered radiation that goes through the filters towards the detector reaches what is known as the diffraction grating. As its name says, the diffraction grating separates the Raman signal into individual wavelengths allocating them into specific grating lines according to the angle they have been spread out. These wavelengths get reflected towards the CCD detector. A CCD



INTRODUCTION & LITERATURE REVIEW

detector is a two-dimensional array of pixels. Each pixel receives an upcoming wavelength according to its specific angle. Same wavelengths will be dispersed at the same angle hence detected by the same pixel, which will reflect in intensity and position when interpreting a Raman spectrum.

Depending on the application, Raman spectroscopy has a variety of techniques or methods that can facilitate the production and collection of data when analysing specific hypothesis.⁴⁸ These technologies can be seen in **Table 1**, together with their most current applications and limitations.



Table 1. Comparison of Raman spectroscopy methods and its current applications.^{48,49}

Raman methods	Applications	Current limitations
Raman fibre-optic probe	In vivo probes for disease detection	Heterogenous nature of tumours. Raman probe can only analyse a single area of the target tissue, within a tumour lesion there will be non-uniform areas of normal cells, cancerous cells and dysplastic cells. If the area analysed by the probe is not the most cancer-developed area, there is room for misclassification.
Conventional Raman spectroscopy	Ex vivo and in vitro studies	Low axial resolution High background Non-expensive Simple to use Point-line or array imaging
Confocal Raman spectroscopy	Ex vivo and in vitro studies	It has high axial resolution Deep tissue analysis <500 μ m Long acquisition times
Surface Enhanced Raman spectroscopy	In vitro studies	It requires biomarkers It requires surface enhancers Long acquisition time Heterogenous intensity of the signal Low background
Coherent Anti-Stokes Raman	Ex vivo and in vitro studies	High spatial resolution Expensive Difficult to implements Short acquisition time



1.4 RAMAN SPECTROSCOPY AND COLLAGEN STRUCTURE

Raman spectroscopy is a vibrational technique that has been used to analyse the progress of different cancers. Different stages during the carcinoma process have been identified in breast cancer, lung cancer, oral cancer and melanoma, etc.. Since this technique has proven good results by detecting spectral differences reflecting biochemical changes during a process, it has been widely recognised as an efficient monitoring tool. Being non-invasive, label-free and real-time technique Raman spectroscopy has also been used to analyse the progress of a tissue-engineered oral mucosa in vitro. As there is no need to label the 3D model, no external component can influence the biochemical interactions within the cells leading to a natural monitoring of the tissue growth.

1.5 SPECTRAL DATA ACQUISITION.

To exploit the technique to its full potential it is important to recognise and consider a number of parameters that can influence the quality and efficiency of the spectral data acquisition. Optimising these parameters is ultimately dependent on the type of equipment available and the type of answer that the spectroscopist is looking for. Sample preparation is the first parameter that should be taken into consideration when using Raman spectroscopy. While it may be true that little or no sample preparation is required when analysing homogeneous materials, this is not the case for samples that have an organic nature. Consideration of how the sample must be presented to the equipment is



INTRODUCTION & LITERATURE REVIEW

most important. A proper analysis of what the operator is looking for when analysing the sample helps shed light on several preparation methods that can improve the outcome of the spectra.²² In some instances, challenges like intrinsic fluorescence will arise when analysing specific type of samples. Fluorophores are molecules that significantly vibrate when they are exposed to short wavelengths of electromagnetic radiation. In response, most of the samples will reflect back emitting light that will travel in longer wavelengths of energy. This phenomenon reflects poorly in the spectra and therefore corrections are usually needed. In most cases, correcting the fluorescence through a mathematical algorithm available in the operating software is the way to go. Others have resorted to using the photo-bleaching feature that will disable the fluorophores in the sample after prolonged exposure to the laser. Here it is important to consider the type of laser being used. Near UV and visible light contain a higher amount of energy that will induce a reaction from the fluorophores in the sample. It has been reported that in most of the cases, switching to longer wavelengths of electromagnetic radiation will minimize fluorescence interference in the spectral data acquisition process.⁵⁰

Another important parameter to consider is the use of appropriate sample holders. Dependent upon the type of samples, in this case biological samples, there are a few substrates that are most commonly used despite the effect they may have on the raw spectral data. Sample holders made of CaF₂, MgF₂, and glass are the most common type used. The first two are ideal substrates when analysing samples which are thicker than <20µm. Their reflective peaks at 320

and 405 cm^{-1} can easily be subtracted without compromising the integrity of the spectral data. On the other hand, samples with a thickness of $\geq 20\mu\text{m}$ can be analysed using conventional glass substrates rendering them more cost-effective than the first two. However, glass slides are reflected in the raw spectra as three intense and broad bands spread across the whole spectral range. To avoid invading the quality of the data, it is recommended that the axial resolution is improved by ensuring adequate tissue thickness. This can be achieved by using high N.A. objectives or increasing the thickness of the tissue as indicated previously.⁵¹

The number of scans used is an important variable in the spectral acquisition process. It goes hand in hand with the time exposure and the quality of data.

These parameters are highly dependent upon the sample being analysed. They should be adjusted and tailored to each experiment. However, close attention should be paid to the integrity of the sample. Longer exposure of samples to the incident beam can sometimes increase the temperature of the sample and affect its nature and particular characteristics.

Once spectral data has been produced and collected, handling and proper interpretation of the results is up most importance. For this bioinformatics plays a role⁵² and there are a variety of techniques that can be used and have been displayed in TABLE 2.

Table 2. Strategies and different algorithms commonly used for appropriate analysis of spectral data.^{48, 49}

Approaches on how to do analysis of spectral data	Research question being addressed	Algorithm characteristics	Chemometric MVA technique
Exploratory analysis of the data	Is there any relationship between samples?	No need of prior information. Unsupervised methods can be used.	Principal component analysis (PCA) Dendograms Self-organising Map (SOM)
Sample classification	Can samples be classified into different groups?	Requires previous information. Prediction of unseen samples for cluster formation. Supervised method can be used. Requires validation.	Partial least squares-DA (PLS-DA) Support vector machines (SVM) Linear discriminant analysis (LDA)
Quantitative analysis of the data	Can spectral data be correlated with specific variables?	A quantitative prediction in previously not seen samples is allowed in relation to a continuous variable	PCA Principal component regression PCR Support vector regression SVR
Explanatory analysis	Is there a difference in physical or in chemical state of the samples?	Identifies the spectral differences as a function of group Unsupervised method	Based on loading vectors: PCA,LDA,CA,PCR



Table 3. Techniques used for collagen characterisation

	Techniques for Collagen Characterisation	The sort of Information they can deliver	Studies Applying these Techniques	Limitations
Microscopy Techniques	Transmission Electron Microscopy	Morphology, Topography	53 54	Sample preparation
	Scanning Electron Microscopy	Topography	55 53 56	Requires dehydration
	Atomic Force Microscope	Information of Molecular topography	57 58	Specialised equipment
Spectroscopic Techniques	Circular Dichroism	Secondary and tertiary structure	59 60 61	Deconvolution is tedious due to software limitations
	Mass Spectroscopy	Mass	62 63 64	Specialised equipment for information about mass range
	FTIR Spectroscopy	Biochemical information	65	High absorption of water compromises quality of signals
	Raman Spectroscopy	Biochemical information	66	Intensity of fluorescence compromises quality of signals



LITERATURE REVIEW.

Characterisation Of Collagen Molecule Using Raman Spectroscopy

1.6 CHARACTERISATION OF COLLAGEN MOLECULES USING RAMAN SPECTROSCOPY

Raman spectroscopy is highly sensitive mainly to two different secondary structures within the collagen macromolecule: the α -helix and the β -sheet structure.⁶⁷ A secondary structure reveals information on how polypeptide chains are being folded, resulting in the formation of any of the above-mentioned structures. A single polypeptide chain that contains the glycine-X-Y motif mainly forms the α -helix structure (abundant in collagen type I and III). To stabilise this structure, hydrogen bonding occurs between the –NH group of one residue and the C=O group of another amino acid within the same chain. On the contrary, multi-stranded polypeptide chains that can be arranged in a parallel or antiparallel direction mainly form a β -sheet secondary structure (abundant in collagen type IV and VII). This structure is stabilised by cross-strand hydrogen bonding between the C=O group of one strand and the –NH group of another strand.⁶⁷ It is only logical to expect more variations in the β -sheet structure than in the α -helix structure,⁶⁸ as collagen fibrils are unique in the presence of the secondary structure. Generally, these secondary structures provide both stability and structure to the collagen fibrils. In Raman spectroscopy, the frequency of the Amide I and Amide III bands can usually detect differences in secondary structures. This region along with lipids and proline and hydroxyproline regions are the three main regions frequently

involved in the conformational changes of collagen structure **Figure 8, Table 4.** Based on an algorithm on the secondary structure of collagen molecule developed by Chou and Fasman,⁶⁹ 19% of the polypeptide chain represents a β -sheet conformation and 18% represents an α -helix structure, which is in accordance with McColl et al..⁶⁷

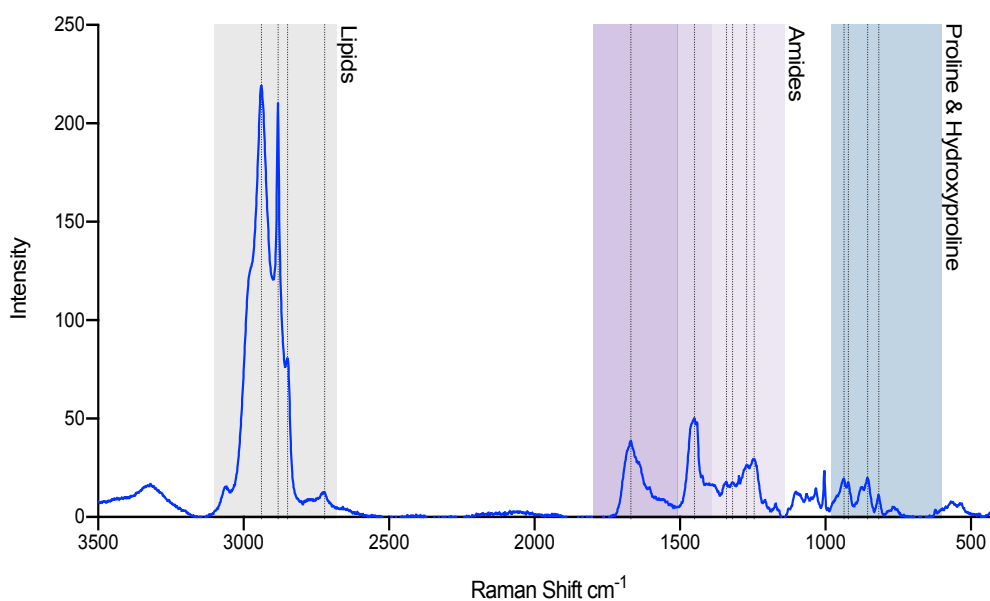


Figure 8. Raman spectra of collagen structure, an average of 60 spectra. The three main spectral regions that frequently reflect main peaks involved in conformational changes.

Table 4. Main spectral peaks that reflect conformational changes in collagen structure.

	Raman shift	Assignment	Reference
Lipids	2939	C-H vibration	27
	2882	CH ₂ asymmetric stretching	27
	2849	CH ₂ symmetric stretching	27
	2722	C-H stretching vibration	27
Amides I, II, III	1669	C=O stretching of amide bond (peptide bond)	2770
	1450	NH ₂ deformation of amide bond (peptide bond)	2770
	1340	CH ₂ scissoring	2770
	1319	CH ₃ , CH ₂ twisting	2770
	1271	N-H deformation of amide bond (peptide bond)	2770
Proline & Hydroxyproline	1245	C-N stretching of amide bond (peptide bond)	2770
	936	C-C stretching of protein backbone	2771
	922	C-C stretching of Pro/Hydro ring	2771
	855	C-C stretching of Pro/Hydro ring	2771
	817	C-C stretching of protein backbone	2771

Furthermore, these structures reflect an Amide I band at 1672 and 1650 cm⁻¹, respectively,^{72,67} This correlates with the findings of Kreplak et al. who reported an Amide I band at 1655 cm⁻¹ that indicated the presence of an α -helix structure, a shoulder at 1630 cm⁻¹ and a 1675 cm⁻¹ peak related to the β -sheet structure.⁷³



LITERATURE REVIEW.

Characterisation Of Collagen Molecule Using Raman Spectroscopy

Kreplak et al. employed, for the first time, the characterisation of collagen I fibrils from an *in vitro* rat-tail model using surface-sensitive Raman spectroscopy (SERS). Although the conformational order of a collagen molecule had already been well established, the presence and prevalence of aromatic side chains for this protein was a topic that remained unclear. Therefore, silver (Ag) and gold (Au) nanoparticles were attached to collagen fibres in order to enhance the Raman signal of the samples. Findings showed that Raman spectra were quite sensitive to the exposure of aromatic side chains on the fibril's surface. Residues in the helical structure of collagen were reflected at 1000 cm^{-1} for phenylalanine (Phe) and 1605 cm^{-1} for both phenylalanine and tyrosine (Tyr). Additionally, Amide I and III were reflected at 1655 cm^{-1} and 1268 cm^{-1} , respectively. Deformations of CH_3 and CH_2 were reflected at 2933 and 1447 cm^{-1} while the stretching vibration of NH appeared at 3320 cm^{-1} . It was also noted that Au nanoparticles enhanced the Raman signal by 10^5 whereas Ag particles enhanced the signal by 10^4 . The peaks presented in this study were the Amide bands, COO- groups and CH vibrations. Finally, the Amide I peak also reflected a shoulder at 1630 cm^{-1} , characteristic of a triple-helix secondary structure.⁷⁴

Collagen type I represents almost 90% of all collagen in the dermal layers of skin and is mainly responsible for providing tensile strength to the soft tissue. Skin is also composed of 10% of collagen type IV that is located primarily in the basement membrane of the epithelium layer. Due to its structural



LITERATURE REVIEW.

Characterisation Of Collagen Molecule Using Raman Spectroscopy

conformation, this type of collagen is responsible for maintaining the stability and integrity of this layer. However, since it represents such a small percentage of the total collagen present in soft tissue, it has not drawn much attention from the spectroscopic field. Nguyen et al. were the first to characterise collagen type IV with Raman spectroscopy. They used conventional Raman spectroscopy to characterise the molecular conformation of both collagen type I and IV with their respective spectral profile.²³ While comparing collagen type I with collagen type IV, Nguyen et al. reported that the Raman spectral differences reside in both the intensities and the frequency of the bands.

For instance, Amide I, Amide III, and spectral bands 856, 875, 920 and 938 cm^{-1} reflected a higher intensity in collagen type IV than for collagen type I. This observation was also seen in the 1004 and 1033 cm^{-1} peaks that corresponded to the phenylalanine ring vibrations. With respect to the phenylalanine intensities, these differences might indicate a lower content of phenylalanine in collagen type I when compared to type IV. It could also suggest that a different structural arrangement could exist between both proteins at the level of the phenylalanine residues.²³

Moreover, the localised difference in the intensity ratio of the Amide III bands I_{1271}/I_{1246} indicated a difference between both proteins in the distribution of proline amino acids. This corresponds to the observation that I_{1246} indicates the presence of proline rich regions whereas the I_{1271} suggests proline poor regions



LITERATURE REVIEW.

Characterisation Of Collagen Molecule Using Raman Spectroscopy

⁷⁵. Furthermore, the reflectance of Amide I at 1668 and 1673 cm^{-1} clearly indicates a different distribution of the X and Y residues when comparing collagen type I to collagen type IV, respectively. Raman spectra also identified spectral peaks characteristic of the collagen type IV molecule. Well-defined peaks in the 510 and 540 cm^{-1} bands (S-S vibration) were indicative of the presence of disulphide bridges.⁷⁶ It is also believed that the band at 815 cm^{-1} , with higher intensity in collagen I than in collagen IV, may indicate the presence of glucosyl-galactosyl-hydroxylsyl in or on leucine crosslinks occurring in tropocollagens.⁷⁷ This feature correlates with the triple-helical structure of the collagen type I. Complementary to this, the epidermis, dermis and dermal-epidermal-junction (DEJ) were also analysed, and their spectral profiles were compared in order to decipher the main differences. When skin was analysed, this 815 cm^{-1} band was visible in the dermal layer but not in the epithelium layer which correlates with the fact that the dermal layer is mainly composed of collagen type I.

1.7 STUDIES OF COLLAGEN CHANGES DUE TO PHYSIOLOGICAL PROCESSES

There are many factors that can damage collagen structure. Collagen is a protein that is affected by different physiological processes such as, chronological aging, enzymatic reactions, wound healing and many other processes that have been listed in **Table 5**. During chronological aging for example, degradation of



LITERATURE REVIEW.

Characterisation Of Collagen Molecule Using Raman Spectroscopy

collagen type I occurs, which is why the proportion of collagen type I is reduced and appears more widely spread over the dermal layers. Additionally, the amount of collagen type IV also gets degraded.²³ Dermal collagen plays a crucial role in repairing and/or regenerating the existing tissue maintaining tissue integrity and thus keeping physiological processes on track. However, factors such as age, UV exposure and disease have been proven to affect certain properties of the collagen molecule.⁷⁸⁻⁷⁹ However, what is occurring at the biochemical level of this molecule remained unclear,⁸⁰ thus requiring further work. To understand in more detail the progression of a disease mainly due to changes in the collagen structure, a technique that can identify subtle alterations is very much needed. Raman spectroscopy can easily pick up on the conformational changes of the secondary structure and hydrogen bonding of collagen for example. These changes are reflected in the shift of frequency positions and width of both Amide I and Amide II bands.⁸⁰ Dehring et al. for example, used the Amide III region as a biomarker to measure collagen damage as a function of time. They reported that the Amide III region at 1235 cm^{-1} represented the bending vibration of NH_2 in a random coil and the peak at 1265 cm^{-1} indicated the bending vibration of NH_2 in an α -helix structure. In their work they used these two band areas to calculate the area ratio of the amide III region and they reported that the older the specimen in question the higher the area ratio of the Amide III region, indicating a higher content of disordered collagen fibres.²⁵ This was seen in the collagen of both a 20-month-old wild type mouse and a 12 to 14 months transgenic mouse, when compared to a



LITERATURE REVIEW.

Characterisation Of Collagen Molecule Using Raman Spectroscopy

standard 12 to 14 months wild type specimen. Additional to this, changes in the secondary structure of collagen proteins are readily detected by Raman spectroscopy. Irrespective of whether these changes are caused by a mechanical, environmental or chemical factor, they will be reflected in a shift of band position.

In another study, Dehring et al.²⁵ explained the aging process as a chemical factor that caused the crosslinking of collagen fibres resulting in an increase in a disordered secondary structure in the protein molecule. This is in agreement with the shifts to higher wavenumbers seen in both the 20-month wild type at 1235 cm^{-1} and the transgenic mouse at 1236 cm^{-1} , when compared to the standard 12 to 14-month wild type at 1231 cm^{-1} band. These changes in band position due to structural changes in the secondary structure of the collagen molecule are in agreement with the spectral data reported by Zhang et al.,⁸⁰ who suggested that changes in collagen behaviour might be related to collagen hydration. It was also believed that as age increases, so does the content of bulk water in soft tissues whereas the content of collagen-bound water decreases. However, while there have been studies focused on measuring the bulk water content of skin tissue, the question of water bound specifically to collagen is more challenging to study.

Aiming to characterise spectral features of collagen-bound water, Zhang et al. employed confocal Raman microscopy to analyse both collagen type I and intact



LITERATURE REVIEW.

Characterisation Of Collagen Molecule Using Raman Spectroscopy

skin tissue, by using different relative humidity (RH) levels and by recording the exchange of H₂O to deuterium oxide (D₂O).⁸⁰ They found in both type I collagen and skin tissue that the frequency shift of Amide I band goes down as the RH value increases. Complementary to this, the frequency shift of Amide III band reflected an upshift.

These observations correlate with the well-established theory that when a hydrogen atom binds to another atom from a *stretching* vibration, a downshift in frequency is seen, whereas an upshift happens when it involves an atom from the *bending* vibration. However, in the D-H exchange measurements, the Amide I band suffered a downshift as the exposure time to D₂O kept increasing. The 1665 to 1657 cm⁻¹ downshift is suggested to be due to the H-D exchange at the carbonyl-hydrogen bonding of Amide I. The Amide III band also reflected some changes due to the D-H exchange. For instance, a shoulder right next to the 1003 cm⁻¹ band, on the lower frequency side, was formed along with a decrease in intensity of the Amide III band.⁷¹ These spectral observations might be a consequence of the N-H to N-D exchange. Furthermore, they also reported that as RH values kept increasing, so did the intensity of the 938 cm⁻¹ bands.

This observation correlates with the results obtained from the dermis of pig skin. This statement is also supported by the findings of Xiao et al.,⁸¹ where they showed that the intensity of the 938 cm⁻¹ band reduces as the temperature and dehydration increases. Furthermore, when Raman analysis of the H-D exchange



LITERATURE REVIEW.

Characterisation Of Collagen Molecule Using Raman Spectroscopy

in both pure collagen type I and pigskin dermis was conducted, it was found that the peak intensity at 938 cm^{-1} decreases as the exposure time to D_2O increases. These findings correlate with already reported spectral data that the intensity of the 938 cm^{-1} bands can reflect information and keep track of the collagen-bound water content in skin tissue.

Collagen I goes through post-translational modifications after a certain period of time specifically the hydroxylation of lysine or proline residues as well as the glycosylation of hydroxylysine, and here a lysine derivative can be explored.⁸² They are usually a by-product of some physiological and pathological processes, such as aging and diabetes mellitus.⁸³ The most common modification is the non-enzymatic glycation of specific lysine residues within the collagen type I molecule. The bonding of a sugar to a lysine residue triggers a series of complex chemical rearrangements that lead to the production of irreversible advanced glycation end products (AGE's).⁸⁴

Table 5. Examples of clinical conditions altering the molecular structure of collagen.

		Clinical Conditions	Compromised Tissue	Studies with Raman Spectroscopy
Physiological Conditions	Age-related conditions	Ageing	Bone Cartilage Skin	Ager et al., 2005 ⁸⁵ Dehring et al., 2006 ²⁵ Nguyen et al., 2013 ⁸⁶
		Glycosylation	Skin	Gilbert et al., 2013 ⁷¹ Pererira et al., 2017 ⁸⁷
		Dehydration	Cartilage Skin	Fields et al., 2017 ⁸⁸
		Mineralization	Bone	Paschalis et al., 2001 ⁸⁹ Buckley et al., 2012 ⁹⁰
Pathological Conditions	Wound contraction	Wound healing (wound contraction)	Skin	Zhang et al., 2011 ⁹¹ Hao. Liu et al., 2016 ⁹² Yan et al., 2017 ⁹³ Sun et al., 2018 ⁹⁴
		Skin graft contraction	Skin	
		Glycosylation (disease related, e.g. Diabetes Mellitus)	Skin	Guilbert et al., 2013 ⁷¹ Pereira et al., 2015 ⁹⁵



LITERATURE REVIEW.

Characterisation Of Collagen Molecule Using Raman Spectroscopy

These series of modifications and AGE's immediately reflect upon the properties of collagen type I, resulting in a loss of flexibility of the triple-helix structure and hence rigidity of the molecule.⁹⁶ Failure to reduce over glycosylation can lead to diseases, such as scurvy and osteogenesis imperfecta respectively.^{97,98} Even though a fluorimetric assay is the most common technique employed to quantify the amount of AGE's present in the glycation process,⁹⁹ the molecular changes occurring during the this process remained unclear. Experiments performed in this area aimed to achieve a clearer understanding of the physiopathology process of ageing.⁹⁵ The increasing presence of AGE's in skin during aging or age-related diseases, such as diabetes mellitus is well documented.¹⁰⁰ M. Guilbert et al. used Raman microspectroscopy to characterise native and *in vitro*-glycated collagen I to identify to what extent these post-translational modifications affect structural features of collagen. This study showed that the Amide I band remained in the same frequency shift as the glycation doses increased. This statement supported that no conformational change occurred in the triple-helical structure of collagen I during glycation. Additional to this, most of the spectral bands showed an increase in intensity as glycation doses increased, except for the 470 cm^{-1} and 1556 cm^{-1} bands. These spectral bands are representative of the proline and hydroxyproline/proline rings respectively. The reduction of intensity of these bands reflected a clear alteration in the exposure of proline residues within the collagen type I molecule upon the glycation process. This experimental design



LITERATURE REVIEW.

Characterisation Of Collagen Molecule Using Raman Spectroscopy

resembled the pathophysiological process of glycation occurring in the human body. In fact, the concentration of glucose used in this experiment represented the sugar concentration within the bloodstream of, for example, patients with severe diabetes mellitus (50 mM).^{101,102} However, the findings of Pereira et al. differ from those of Guilbert et al., Pereira et al. used confocal Raman spectroscopy to characterise the non-enzymatic glycation in skin tissue from diabetic elderly women (DEW), healthy elderly women (HEW) and healthy young women (HYW). Results indicated the presence of a protein adduct, Pentosidine and Glucosepane, which are the main AGE's responsible for the transformation of skin structure.⁹⁵ These adducts were reflected in the proline/hydroxyproline (800-1000 cm^{-1}) and also in the Amide I and Amide III region. It is important to mention that the glycation of collagen molecules ends up with the formation of AGE's.^{103,104} Furthermore, prior to this study, Glenn et al. characterised the presence of AGE's in Bruch's membrane (of the cornea) with confocal Raman microscopy. Raman spectra reflected the presence of AGE's adducts in the extracellular proteins. These findings correlate with the study of Sell et al., who verified the same procedure. It is worth mentioning that these non-enzymatic AGE's can follow two paths: the first one by producing free radicals, and hence leading to tissue damage; the second one by inducing crosslinking of proteins, such as collagen type I, and thus contributing to skin damage.⁹⁵ These structural changes in collagen type I produce a protein denaturation and a resistance to degradation, which would normally occur by



LITERATURE REVIEW.

Characterisation Of Collagen Molecule Using Raman Spectroscopy

MMP.^{105,106} Collagen type I goes through a structural rearrangement resulting in the exposure of proline and hydroxyproline amino acids.

As mentioned before, the extracellular matrix in skin is mainly formed of a collagen mesh that gives stability and integrity to the soft tissue, and also acts as a cytoskeleton structure for cell adhesion. This is why this protein has such an important role during wound healing process in skin. When scar formation occurs, it is well known that the morphology of scar tissue is significantly different to that of normal skin. For a start, collagen fibres in the scar tissue are more tightly packed and oriented in a parallel manner. However, the morphology of collagen gets more complicated as scars can differ from one another.^{107,108} It has been well documented that formation of collagen fibres takes place during the early stages of the wound healing process, which leads to the formation of scar tissue. Finding a trace of newly regenerated collagen fibres should therefore be possible during the early stages of wound healing. Currently, there is a real need to characterise the regeneration of collagen fibres during this process in order to establish the most appropriate treatment against dysfunctional scar formation. This is important as the formation of extensive scar tissue can reduce patient mobility -as in extensive skin graft contractions which often follow burn injuries- and obviously it can be cosmetically disfiguring. In 2016, Hao Liu et al. used Raman spectroscopy to characterise the regeneration and morphology of collagen formation at different time points during the wound healing process by calculating the band area ratio of



LITERATURE REVIEW.

Characterisation Of Collagen Molecule Using Raman Spectroscopy

1665/1445 cm^{-1} bands and monitoring collagen levels present in wound beds. The 1665 cm^{-1} band expressing the presence of collagen content through the stretching vibration of the carbonyl group $\nu(\text{C}=\text{O})$ or amide I. The 1445 cm^{-1} band is representing the scissoring vibration of CH_2 , coming from the total matrix of the wound sample. When calculated, the area ratio of these two peaks kept increasing as a function of time, indicating that collagen levels were higher by the latter stages of the healing process. This method coupled with Principal Component Analysis (PCA) indicated a clear separation of groups based on different stages of dealing wound healing. However, although an indication of collagen levels as a function of time is considered valuable information, an in-depth description of how secondary structures of this protein are affected during the wound healing process is still needed.

The ECM of skin tissue is mainly composed of collagen type I and collagen type III. In uninjured skin tissue, the conformational ratio of collagen type I to collagen type III is about 85% to 10% respectively. Due to the morphology of both types of collagen, collagen type I provides tensile stiffness to the skin while collagen type III shows more distensible properties. These properties are the main reason why the content of collagen III is higher than collagen I during the early stages of the wound healing process.⁹² In pathological processes such as diabetes, the production of collagen is inevitably delayed and so is the healing process of any injury. These disturbances result in a delayed re-epithelisation due to a defective migration and proliferation of keratinocytes and fibroblasts,



LITERATURE REVIEW.

Characterisation Of Collagen Molecule Using Raman Spectroscopy

giving the appearance of a domino effect. Therefore, treatments to promote collagen production and healing particularly in diabetic wounds are needed. Yan et al. used Raman microspectroscopy to characterise normal, diabetic and MSC-treated diabetic wounds at different time points of the wound healing process. These experiments were carried out to characterise and validate the use of MSC as a treatment for diabetic wounds. With this study they concluded that the band area ratio of $1665/1445\text{ cm}^{-1}$ provides information about collagen accumulation at different time points of wound healing process. Using PCA as the analytic method, different healing groups clustered according to the ratio of the previous bands mentioned. The difference in area ratio allowed for a separation between wound samples of different healing time points. These findings indicated that the progress of collagen accumulation in wound healing process can be monitored by Raman spectroscopy.

1.8 STUDIES OF COLLAGEN CONTRACTION IN SKIN AND ORAL MUCOSA GRAFTS

Burn injuries are among the most traumatic injuries across the world and are listed as the 4th most common trauma worldwide.^{109,110} They are considered a global public health problem, being responsible for nearly 180,000 deaths per year.¹¹¹ In 2004, ~11 million people worldwide were victims of severe burn injuries requiring medical attention,¹¹¹ and only in the UK, ~13,000 people are



LITERATURE REVIEW.

Characterisation Of Collagen Molecule Using Raman Spectroscopy

admitted in the hospital per year due to burn injuries.¹¹² This traumatic injury is considered one of the main leading causes of disability-adjusted life-years (DALYs).

In patients with extensive skin loss (due to burn or traumatic injuries in general), large areas of skin grafts are the treatment of choice. However, it has been well-reported that even after implantation of the skin graft to the surface area of a wound, contraction of the graft continues to occur. This contraction of the skin graft after implantation is an unfortunate event that often results in decreased mobility -due to the heavily contracted skin- and very visible skin deformities that can seriously affect the patient's confidence particularly in young children.¹¹³

While a significant amount of research has been devoted to study the contraction of skin grafts, a better understanding of the biochemical pathway of contraction in soft tissues remains unclear Error! Reference source not found.. During the wound healing process, crosslinking of collagen fibres occurs as part of the normal physiological phenomenon of wound contraction. While it may be true that skin grafting has proven to reduce wound contraction when implanted in wounds, they have also shown a degree of contraction that sometimes results in joint mobility. This phenomenon is not only seen in skin grafts but unfortunately is also present in oral mucosa grafts.



LITERATURE REVIEW.

Characterisation Of Collagen Molecule Using Raman Spectroscopy

Due to its versatility, oral mucosa grafts have been widely used for both intraoral and extraoral applications such as repair of cleft palate or reconstructive surgery for head and neck cancer and also to repair scarred tissue in the urethra. However, both clinically and in the laboratory, this contraction of skin and oral mucosa grafts continues to advance while culturing and even after implantation at the injury site.

Contraction in a full-thickness TEBM model is a reduction in the surface area of the graft with concomitant thickening (i.e. no overall reduction in mass). This contraction is most vigorous when the tissue-engineered graft is not properly secured. Suturing of the edges massively reduces the extent of the contraction. In fact, in 2001, Chakrabarty et al. explored the nature of contraction occurring in an in vitro tissue-engineered skin model, as well as different methods to reduce or avoid this phenomenon. The thickness of the dermal matrix used, the number of keratinocytes and fibroblasts added, and the methodology of sterilising the dermis were all examined for their impact on contraction of these engineered skin models. One interesting fact was that within a few days of contraction, the epidermal keratinocyte layer were removed leading to the relaxation of the underlying dermis and thus going back to its pre-contracted original thickness and surface area.⁴⁰ Moreover, it was also noticed that increasing the number of keratinocytes seeded increased the degree of contraction. This observation was also confirmed when using collagen gels as a dermal matrix.¹¹⁴ It was then shown and concluded that fibroblasts had little to



LITERATURE REVIEW.

Characterisation Of Collagen Molecule Using Raman Spectroscopy

no influence over this process. Which led to the hypothesis that contraction of these 3D skin models is mainly due to keratinocytes exerting contractile forces over the dermal layer,⁴⁰ irrespective of the sterilisation method used on the de-epidermised dermis (DED). Not to mention that the methodology of sterilising the dermis did affect contraction essentially in a way in which, the stiffer the dermis the less they contracted and the softer the dermis the more they contracted.

Furthermore, Chakrabarty et al. measured the dermal mass of the DED before and after seeding both keratinocytes and fibroblast on the dermal matrix. Despite the number of cells being seeded, dermal mass remained constant throughout the whole process whereas dermal thickness increased while contraction was occurring. This strongly suggested that collagen fibres were not being degraded but instead being rearranged in a different way.⁴⁰ This observation goes in agreement with findings from Harrison et al., who used a pharmacological approach to identify any possible evidence for collagen synthesis, breakdown or rearrangement of collagen fibres.¹¹³ Therefore, in order to investigate the mechanism behind contraction, pharmacological agents targeting collagen crosslinking, synthesis and degradation rates were used and their effects related to the degree of contraction observed. Briefly, incorporation of vitamin C into the cultured models resulted in a significant increase in contraction. At the same token, contraction was significantly reduced when culturing these models in low-calcium medium.¹¹⁵ Data from this study also



LITERATURE REVIEW.

Characterisation Of Collagen Molecule Using Raman Spectroscopy

showed how the extent of contraction significantly increased when adding other pharmacological agents into the culture medium, such as estrogens (e.g. Estrone and 17β -estradiol), MMP-2 and MMP-9 activity. Additionally to this, and in order to inhibit the effect that these drugs were having in contraction, Chakrabarty et al. experimented with Galardin, a broad-spectrum inhibitor for MMP agents; however, it was found to be ineffective in influencing contraction. Therefore, based on these studies, it appeared that collagen fibres underwent covalent crosslinking to each other over time eventually rendering contraction an irreversible process. This is well supported with previous literature stating that LOX enzyme promotes the crosslinking of collagen fibres and studies with β -APN, a plant-derived agent known to inhibit lysyl oxidase activity, showed that contraction could be reduced to a significant degree by inclusion of this drug in the tissue-engineered skin model as it was developing.¹¹³

Graft contraction continues to be a poorly understood clinical problem and a better insight into the underlying biochemical mechanism behind contraction is still very much needed.

Table 6. Studies on contraction of skin and oral mucosa grafts.

	Clinical Conditions	Studies of Graft Contraction
Application of Skin Graft	Burn Injuries Traumatic Injuries	Thornton et al., 2008 ¹¹⁵ Harrison et al., 2008 ¹¹² Harrison et al., 2006 ¹¹³ Schneider et al., 2006 ¹¹⁶ Chakrabarty et al., 2001 ⁴⁰
Application of Oral Mucosa Graft	Treatment of Head and Neck Cancer Reconstruction of Cleft Palate Reconstruction of Urethral Strictures	Osman et al., 2015 ¹¹⁷ Patterson et al., 2011 ¹¹⁸ Bhargava et al., 2008 ¹¹⁹ Bhargava et al., 2004 ¹²⁰ Ueda et al., 1986 ¹²¹ Freedlander et al., 1982 ¹²²

1.9 STUDIES OF COLLAGEN CHANGES DUE TO

COLLAGEN MODIFICATION AND PROCESSING.

Collagen, as previously stated, is present in the extracellular matrix of all tissues and provides tissue integrity to enhance its mechanical responsiveness. Micromolecular changes occurring in the collagen molecule can have a strong impact on the proper function of the tissue. Heart valve leaflets, for example, are mainly composed of three different layers: the ventricularis, the spongiosa and the fibrosa. The latter layer is mostly formed of collagen and it is responsible



LITERATURE REVIEW.

Characterisation Of Collagen Molecule Using Raman Spectroscopy

for providing stiffness and strength to the leaflets during diastolic movements. Degenerative modifications in this layer could easily compromise the functionality of the aortic valve. In this scenario and to ensure the proper functionality of the heart valve allograft, monitoring the tissue before implantation is currently available. However, these techniques only detect macroscopic damages, which is why detection of micro-molecular defects is still very much needed. Layland et al. utilised Raman spectroscopy to analyse conformational changes occurring in aortic valve tissues after cryopreservation aiming to identify any structural change or damage as a response to the allograft preservation methods. The porcine aortic valve leaflets were exposed to collagenase (a degrading enzyme) for different periods of time. The longer the leaflets were exposed to the enzyme, the more the spectral intensities were reduced. Layland et al. analysed all Raman data with the multivariate analysis method (MVA) known as PCA. They found out that the longer the leaflet samples were exposed to collagenase, the more separated the groups would be. The Raman data of leaflets exposed to collagenase for 17 hours were clearly separated from the data belonging to the non-treated samples. This separation was more obvious after 17hrs than after 15 min. The bands at 938, 1244, 1272 and 1664 cm^{-1} were the peaks considered when comparing these groups. It was concluded that the reduction in intensities was related to the degradation of collagen. It is also believed that reduction of intensities could be due to collagen fibres being less dense when treated with collagenase.



LITERATURE REVIEW.

Characterisation Of Collagen Molecule Using Raman Spectroscopy

Both, excessive and/or insufficient crosslinking of collagen fibres are a serious problem that can result in several different diseases (e.g. Fibrosis and ED syndrome, respectively). As everything, a balance must be kept for the proper functionality of any soft and hard tissue. Without the formation of a collagen mesh in the ECM, attachment of cells would not be possible, and tissues would lack stability and tissue integrity. At the moment, there are many collagen-based biomaterials available for clinical applications but to improve their immunogenic and mechanical properties, they have undergone several chemical procedures. One of these chemical methods normally involves crosslinking with glutaraldehyde (GA).⁷⁰ While a few authors have investigated the process behind the GA and collagen bonding, the chemistry behind this remains unclear.^{123,124} Raman spectroscopy can identify specific biochemical changes occurring in a specific molecule. Interactions with other molecules lead to the formation of different functional groups that can easily be reflected on the Raman spectra. Accordingly, M. Jastrzebska et al. used Raman spectroscopy to analyse both (i) Achilles tendon isolated collagen and (ii) glutaraldehyde-stabilised porcine pericardium to see if Raman spectra could pick up on the chemical bonds formed by this glutaraldehyde-collagen mechanism. M. Jastrzebska et al. identified four types of chemical bonds in this study, ether-type bond, amide NH with an aldehyde group, secondary amines through Schiff base intermediates and Pyridinium-type cross-links.

Ether groups:



LITERATURE REVIEW.

Characterisation Of Collagen Molecule Using Raman Spectroscopy

These bonds are reflected in Amide I, Amide III, 1094 cm^{-1} and $1300\text{-}1330\text{ cm}^{-1}$ spectral regions. The Amide I band reflected a reduction in intensity after collagen type I was exposed to glutaraldehyde. This reduction in intensity was thought to be due to the formation of an ether type bond between the aldehyde group of the GA molecule and the C=O group of the peptidic bond. This reaction might need the presence of an H_2O molecule in order to take place. Aside from the discrepancy in intensity, an upshift of Amide I was also observed after being in contact with a GA molecule. In native collagen type I, Amide I and Amide III were reflected at 1655 cm^{-1} and $1247/1269\text{ cm}^{-1}$ respectively. However, after exposure to GA molecule, Amide I was reflected at a frequency of 1664 cm^{-1} whereas Amide III was downgraded to $1243/1266\text{ cm}^{-1}$. It has been well-documented that when a hydrogen atom is bonded to an atom from a stretching vibration, this bond is reflected by a downshift. However, if the hydrogen binds to a bending vibration bond it would be reflected as an upshift. The formation of an ether type bond at the level of the C=O group gives no space available for hydrogen bonding. This theory justifies the findings of an upshift and downshift of Amide I and Amide III respectively and indirectly correlates with Zhang et al. findings as well. Furthermore, the downshift observed in Amide III bands correlate with the findings obtained from Gniadecka et al. work ¹²⁵. In their study, a downshift of the amide III band was properly identified when analysing photo-aged skin. This spectral feature was explained as a higher extent of protein folding. Other studies have shown that the amount of crosslinks in a collagen molecule increased after exposure of skin to UV light ¹²⁶¹²⁷¹²⁸.



LITERATURE REVIEW.

Characterisation Of Collagen Molecule Using Raman Spectroscopy

Another distinct observation between the non-treated and glutaraldehyde-treated pericardium tissue relies on the intensity of the spectral range of 1300 to 1330 cm^{-1} . An increment in the intensity band was reported after pericardium tissue was exposed to glutaraldehyde. This increase in intensity may be reflecting the CH bending from an aldehyde group before the formation of an ether type bond. Similar behaviour is observed in the 1094 cm^{-1} band that is expressing the asymmetric stretching vibration of the C-O-C bond. It is only logical to assume that since the C-O-C is the functional group of the ether type bond, after exposure to the GA molecule, the formation of this bond has considerably increased and so does the intensity of the 1094 cm^{-1} band.

Secondary amides:

These are observed in spectral ranges of 1266-1272 cm^{-1} and 3200 to 3700 cm^{-1} . Within the 1266 to 1272 cm^{-1} spectral range, the deformation of N-H group of the peptidic bond is expected to be reflected. In both collagen and pericardium tissue there is a decrease in intensity in the N-H deformation of Amide III region. M. Jastrzebska suggested that this spectral feature could be explained by the bonding between the carbonyl group C=O from the GA molecule to the NH of the peptidic bond of collagen, forming a secondary amide type of bond. In fact, this statement also reflects on the decrease in intensity of the 3324 cm^{-1} band, which represents the symmetric vibration of the NH group



LITERATURE REVIEW.

Characterisation Of Collagen Molecule Using Raman Spectroscopy

Secondary amine groups through Schiff base intermediates:

It has been well-documented that primary amines (NH_2) of both lysine and hydroxylysine residues can bind to the aldehyde group of an external molecule through the formation of a Schiff base. This statement is supported by the work of M. Jastrzebska et al., where the scissoring vibration of the primary NH_2 from the lysine and hydroxylysine amino acids showed a poor intensity in the 1555 to 1575 cm^{-1} spectral band. Additional to this, the unstable formation of a Schiff base leads to the formation of a secondary amine, which not only justifies the previous finding, but it is a characteristic reaction of the crosslinking occurring in collagen, which is reflected by a decrease in the intensity of the 1555 to 1575 cm^{-1} spectral band.

In tissue engineering applications, collagen-based scaffolds are commonly used due to the properties that collagen provides to human tissues. An example of a collagen-based scaffold would be the three-dimensional collagen hydrogels that are widely used in the bioengineering field¹²⁹⁻¹³⁰ and that can be produced through a wide variety of experimental designs and/or under crosslinking methods to provide more durability to these in vitro models. Hwang and Lyubovitsky et al. have previously used characterisation methods such as second harmonic generation (SHG), fluorescence spectroscopy and transmission electron microscopy (TEM) to provide a basic understanding of the structural effects of collagen crosslinking, polymerisation temperature and



LITERATURE REVIEW.

Characterisation Of Collagen Molecule Using Raman Spectroscopy

initial collagen concentration in 3D collagen hydrogels respectively.¹³¹ However, additional information at the molecular level about the molecular effects that these factors can cause in hydrogel scaffolds is still very much needed. Hence to cover this gap, Hwang and Lubovitsky et al. used Raman spectroscopy to monitor structural changes in collagen hydrogels after exposure to the factors previously mentioned. The crosslinking reagents used were glycerinaldehyde, 1-Ethyl-3-(3-dymethylaminopropyl) carbodiimide (EDC), and EDC/N-hydroxysuccinimide (NHS).

Findings showed that out of all three reagents, glycerinaldehyde caused the most distinctive modifying effect at the molecular level of collagen. For the control collagen hydrogels, peaks in the spectral region of 800 to 1000 cm^{-1} were reflected at 814, 846, 871, 921 and 936 cm^{-1} .¹³¹ After collagen hydrogels were exposed to glycerinaldehyde, the 814 cm^{-1} peak became sharpened and an increase in the intensity of the 936 cm^{-1} band located in the 936/921 doublet was clearly noticed. These spectral differences might be due to an increase in the packing organisation of the hydroxyproline/proline residues and the backbone of collagen protein. The 814 cm^{-1} bands remained in the same frequency as in collagen hydrogels, indicating no conformational change of the protein backbone after glycation. Additionally, bands at 846 and 871 cm^{-1} detected in the collagen hydrogel sample had an increase in frequency after samples were exposed to glycerinaldehyde (855 and 877 cm^{-1}). These spectral bands correlate with the findings of Frushour and Koenig where collagen from bovine Achilles



LITERATURE REVIEW.

Characterisation Of Collagen Molecule Using Raman Spectroscopy

tendon was analysed and ν (C-C) of proline and hydroxyproline rings were reflected at 856 and 876 cm^{-1} , respectively.¹³²

Furthermore, Amide III region also indicated spectral differences after crosslinking of collagen. The shift in frequencies of the Amide III bands, 1241/1268 cm^{-1} reflects conformational changes in the secondary structure of collagen. After being exposed to crosslinking reagent glyceraldehyde, these peaks were shifted at 1247/1283 cm^{-1} . Spectral differences in the Amide III band sheds light over the secondary structure of collagen protein. These shifts in frequencies might be a result of a drastic reorganisation of the orientation of the collagen fibres during crosslinking.^{131,133}

There was also an increase in intensity in the CH bending mode at 1450 cm^{-1} and the appearance of 1468 cm^{-1} band in the glycated samples. Changes in intensities of the former peak might be an indication of changes in the amount or length of the CH groups of arginine and lysine residues and the latter peak might indicate modifications around these two amino acids.¹³⁴ It is believed that these changes occur because the amino group $-\text{NH}_2$ of lysine or arginine, which can easily react with the aldehyde group of the glyceraldehyde component. An increase in intensity was also seen in the 1604 cm^{-1} band after exposure to glyceraldehyde. Stretching vibrations from the C=C bond in the phenylalanine and tyrosine aromatic rings were reported at 1604 cm^{-1} . These residues can easily react to form AGE's. In fact, it was believed that an increase in the



LITERATURE REVIEW.

Characterisation Of Collagen Molecule Using Raman Spectroscopy

formation of arginine-hydroxy-triosidine and lysine-hydroxy-triosidine¹³⁵ directly reflected in the intensity of 1604 cm^{-1} , which suggested the formation of AGE's adducts.¹³⁶

Collagen type I is a fibril-like molecule composed of triple helical structured fibrils arranged in a staggered array with characteristic gaps known as the D-period.¹⁷ At least in bone, collagen type I represents 90% of its organic matrix, and the mineralisation process usually starts in the D-period gaps. These structural characteristics increase the tensile strength and toughness of the bone itself by promoting the crosslinking of collagen. Lysyl oxidase (LOX) is an enzyme that covalently binds to lysyl and hydroxylysyl residues of the collagen molecule producing an aldehyde compound.¹³⁷ However, these enzymatic covalent crosslinks are less frequent in aging and in diabetes or osteoporosis.¹³⁸ It is believed that exercise induces favourable changes to collagen molecules reflecting in an increase in maintaining collagen in its normal morphology.¹³⁹ This by increasing the activity of lysyl oxidase as a balance to β -APN-driven changes in collagen. However, it is still unclear what conformational changes occur at the nanoscale level in the collagen molecule and how these changes may affect bone strength and fracture resistance. Hammond and Wallace used Raman spectroscopy to characterise, at the nanoscale level, the conformational changes of collagen type I from left tibiae tissue caused by exercise and β -APN treatment in a eight-week-old female mice.¹⁴⁰



LITERATURE REVIEW.

Characterisation Of Collagen Molecule Using Raman Spectroscopy

Collagen type I in bone tissue undergoes several post-translational modifications that lead to a specific type of crosslinking. This crosslinking plays an important role when it comes to the mineralisation process of bone tissue. When crosslinking of collagen is altered, so is its structure and thus its mechanical and structural properties reflect poorly on bone tissue.^{141,142} An alteration in the crosslinking pattern at the microscopic level can be enough to compromise the mechanical properties, even if there is no alteration in the inorganic matrix component.¹⁴² Hence, this is why crosslinking of collagen is considered to play a crucial role in the quantification of bone strength for both animals and humans.¹⁴³⁻¹⁴⁴ Post-translational modifications play a crucial role in the normal crosslinking of the collagenous matrix.

Recent studies of crosslinked collagen and tissue models were characterised with FTIR to detect spectral bands for PYD and DPD.¹⁴⁵ The ratio of these bands was calculated with a method described by Paschalis et al. Later on, this method was applied to Raman spectroscopy by Mandair et al. although it has not been properly recognised to date.^{146,147} Therefore in this study, S. Gamsjaeger et al. reproduced the same experimental procedure as Paschalis et al. but using Raman spectroscopy instead.¹⁴⁸ It was found that bone tissue that didn't contain an apparent trivalent crosslink content had no 1660 cm^{-1} band in their second derivative spectrum. Additionally, all samples showing a 1660 cm^{-1} band exhibited a linear correlation between the area of that peak and the content of PYD in the fractions analysed. Furthermore, it was also found that fractions of



LITERATURE REVIEW.

Characterisation Of Collagen Molecule Using Raman Spectroscopy

peptides with enriched pyrrole (PRL) didn't exhibit a 1660 cm^{-1} band in their second derivative spectrum. These findings support the idea that the 1660 cm^{-1} is characteristic of the trivalent-collagen cross-linking of PYD. This method was also tested in whole tissues such as human bone, dentin, and predentin and porcine skin. It is important to mention that the dermis of skin contains a different type of crosslinks to bone. Even though both tissues are formed mainly of collagen type I, there is no hydroxylation of the lysine residues of the telopeptides in skin, hence there is a lack of PYD crosslinks.^{149,150}

1.10 SUMMARY

Raman spectroscopy offers considerable potential for the analysis of conformational changes in collagen, which occur in progressive physiological processes, such as, wound healing and ageing as well as pathologies involving connective tissues and following the impact of diabetes on normal wound healing and ageing. This characterisation technique is a non-invasive technique allowing the sample to undergo many other types of characterisation methods. In addition, minimal sample preparation and in some cases no sample preparation is required. Raman spectroscopy has already established a spectral profile of particular bonds in collagen molecule. Therefore, it can easily identify biochemical differences occurring in collagen at different stages of a physiological and/or pathological process.



LITERATURE REVIEW.

Characterisation Of Collagen Molecule Using Raman Spectroscopy

This literature review points out the main regions (lipids, amides and hydroxyproline and proline regions) that are frequently involved in the conformational changes of collagen. This has been achieved by probing into different stages of a process obtaining a spectral profile specific for each stage. By comparing all biochemical profiles, the biochemical differences among different stages can be established obtaining an insight into the biochemical pathway of a disease.



MATERIALS AND METHODS

Production of a TEBM Model

2 HYPOTHESIS

Will Raman spectroscopy identify biochemical changes occurring in the process of contraction as a function of time?

3 AIMS AND OBJECTIVES

1. Produce TEBM models and analyse the degree of contraction with Raman Spectroscopy.
2. Establish a spectral profile of a control model at different time intervals of contraction.
3. Incorporate β -APN into the models and monitor the effect it has on the contraction of models.
4. Establish a spectral profile of the drug-containing models at the time intervals of contraction.
5. Construct a chemometric modelling system to analyse spectral data.

4 MATERIALS AND METHODS

4.1 PRODUCTION OF A TEBM MODEL

The production of a TEBM model involves a long process of preparation beforehand. For an easier understanding this process can be described under the next main topics.

4.1.1 ORAL BIOPSY

Fresh human buccal mucosa tissue was obtained from an oral biopsy procedure after obtaining Research Ethics Committee's (RECs) authorisation and patient's approval. The oral biopsy was obtained and worked with under the license of Human Tissue Authority (HTA) 12179. It was cut into $\sim 0.5 \text{ cm}^2$ and it was kept for two hours in a solution containing (i) phosphate buffer saline (PBS), (ii) $100 \mu\text{g/mL}$ streptomycin and (iii) $1.2 \mu\text{g/mL}$ of fungizone. Following this, the sample was then transferred to a universal tube containing 0.1% (w/v) Difco trypsin (DT) solution and left overnight in the fridge for fresh tissue samples at 4°C . After being incubated overnight in trypsin solution, oral keratinocytes (O.K.) and oral fibroblasts (O.F.) were ready to be isolated from the biopsy.

4.1.2 ISOLATION OF ORAL KERATINOCYTES

Oral keratinocytes were isolated following Goberdhan *et al.* protocol,¹⁵¹ which is a modification from Rheinwald and Green's method.¹⁵² This process is



MATERIALS AND METHODS

Production of a TEBM Model

explained in detail in references stated above. Briefly, after identifying the epithelium from the dermis, the oral biopsy was gently placed in a Petri dish with a 5mL of Green's medium (composition of this medium can be found in Appendix section 9.1) to keep the sample hydrated. With the epithelium facing up, a corner of the dermis was pinched and slightly pressed against the Petri dish with a scalpel; this was used as an anchor site when trying to remove the epithelium. The oral epithelium was gently peeled off from the lamina propia with a pair of forceps. Oral keratinocytes were obtained by softly scraping with a scalpel blade the top region of the papillary surface and the bottom layer of the oral epithelium. Each sample was scratched for 5 minutes to make sure most keratinocytes were in the medium. Once this was done, the epithelial layer was discarded and the lamina propia was set aside for future oral fibroblasts isolation. Subsequent to this and in order to promote cell expansion, cell suspension was then placed in a universal tube and centrifuge at 1000rpm during 5min. Since the supernatant was still cloudy, it was transferred to a new universal tube and centrifuged again at 1000rpm/5min (this with the main purpose of keeping every possible cell from the biopsy). The pellet left in the first universal tube was then suspended with 10mL of Green's medium and then transferred to a T75 flask, which surface was previously covered by a feeder layer of i3T3 fibroblast. The pellet obtained from the second universal tube was then suspended in 2mL of Green's medium and finally incorporated into the T75 flask. Primary cells were nourished and cultured in Green's medium -which was changed every two to three days- until reaching around 80% confluence. After seven days, primary oral keratinocytes had covered most of the available



MATERIALS AND METHODS

Production of a TEBM Model

surface area and were ready to be subcultured. The latter was carried on by washing the substrate with 0.02% EDTA for 5 min in the incubator, followed by a quick rinse with 10mL of PBS and finally replacing these two with an aliquot of 0.1% trypsin to detach cells from the plastic. Cells were stored in trypsin for 5 minutes in an incubator at 37°C followed by the standard protocol for passaging cells. Cells were split in 1:3 ratio for passage 1 and 1:4 ratio for passage 2. Protocol for passage of cells has been added to Appendix section, 9.4. After cell expansion, cells were stored in liquid nitrogen, Appendix section 9.5.

4.1.3 ISOLATION OF ORAL FIBROBLASTS

To isolate oral fibroblast from the biopsy, the dermis set aside after removing the epithelium was then rinsed with PBS. Further to this, dermis was then placed in a Petri dish with 5mL of fibroblast medium and grinded continuously with the scalpel blade until it was properly minced. It was then transferred to a T25 flask with 10mL of 0.5% collagenase A. Minced dermis was then kept overnight in an incubator at 37°C to allow collagenase to cleave all collagen fibres. Next day, suspension was transferred to a universal tube and centrifuged at 2000rpm/10min. The remaining pellet was suspended in 5mL of fibroblast medium and then transferred to a T25 flask. The supernatant was placed in a second universal tube and centrifuged again at 2000rpm/10min. The remaining pellet was then suspended with 5mL of fibroblast medium. Cell suspension was then added into the T25 flask and stored in the incubator at 37°C/5CO₂. Primary fibroblasts were cultured in fibroblast medium and passaged to a T75 flask after



MATERIALS AND METHODS

Production of a TEBM Model

reaching 80% confluence. Cells were split at 1:2 ratio for all passages done. After cell expansion, cells were stored in liquid nitrogen.

To produce an *in vitro* oral mucosa model, oral keratinocytes and oral fibroblast were used at passage 3 and passage 5, respectively.

4.1.4 PREPARATION OF DE-EPIDERMISED DERMIS

To prepare the de-epidermised dermis (DED), human cadaveric skin (Euroskin) previously sterilised and preserved in glycerol was placed into a plastic flask container with 1M of NaCl and kept for over 24 hours in the incubator at 37°C. To completely remove any remaining glycerol, skin was then stored in PBS for over 72 hours, replacing the PBS every 24 hours. After washing off the glycerol, the epithelium was then easily removed from the dermis and the latter was then cut in small squares of 2cm² size. To produce the *in vitro* oral mucosa model, a total of six samples (six DED squares) were prepared and placed in a six-well plate. The rest were transferred to a container with Green's medium and stored in the incubator. A protocol of this process can be followed in the Appendix section 9.3.

4.1.5 PREPARATION OF TEBM MODEL

Six DED samples were placed in a six-well plate with the papillary surface facing upwards. Six sterile metal rings were allocated on top and on the centre of each DED sample and slightly pressed down to make a seal between the DED and the stainless-steel ring. For each well plate, the surface area outside the



MATERIALS AND METHODS

Production of a TEBM Model

metal ring was then covered with Green's medium and subsequent to this, 3×10^5 oral keratinocytes and 1.5×10^5 oral fibroblasts (composition of this medium can be found in Appendix section 9.2) were seeded simultaneously inside the metal ring. The remaining space within the metal ring was then filled up with Green's medium until reaching a cell suspension of $\sim 500 \mu\text{L}$. All six samples were left in the medium and placed in the incubator at 37°C for the first 24 hours. At the next day, medium within the ring was carefully replaced with fresh medium and the experiment was placed back into the incubator. Twenty-four hours later, metal rings were carefully removed, and the seeded area was carefully excised with a scalpel. Samples were then kept in the incubator for 24 hours more. The next day, each sample was then placed onto metal grids raising them to an air-liquid-interface (ALI). This was considered day 0 of the experimental design.

The ALI stage was reached by replacing the medium with fresh Green's medium making sure that the undersurface of the DED was in contact with the medium and the top surface was directly exposed to the air. These three stages can be seen in **Figure 9**. All six samples were placed back in the incubator and cultured for 28 days and medium was replaced every two to three days.

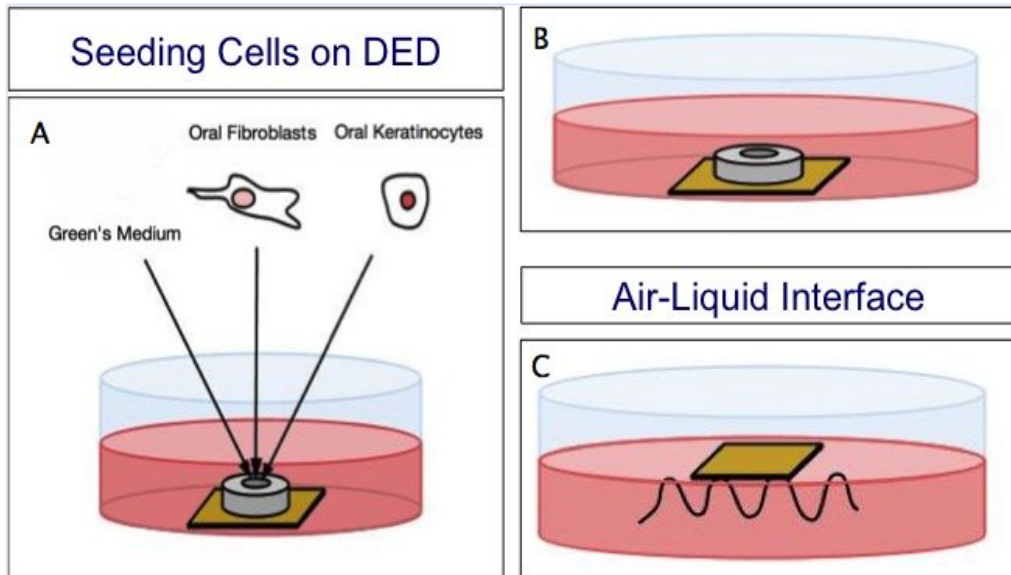


Figure 9. Schematic representation of the three main steps towards preparing a TEBM model. A) Seeding of both O.K. and O.F. within the metal ring. B) Dermal matrix is kept submerged for ~48 to 72 hours. C) Dermal matrix is raised to an ALI.

4.1.6 PREPARATION OF A TEBM MODEL WITH β -APN

To produce the *in vitro* oral mucosa samples with β -APN, the same procedure described in section 4.5 was followed. However, once samples were raised to an ALI, a solution of Green's medium containing 200 μ g/mL of β -APN was used during the rest of the experiment every time medium needed to be replaced (instead of using only Green's media).

4.1.6.1 PREPARATION OF β -APN STOCK SOLUTION



MATERIALS AND METHODS

Production of a TEBM Model

To inhibit contraction in the *in vitro* oral mucosa samples, a solution of medium with 200 μ g/mL of β -APN was added, but to do this, a 10mL of 20mg/mL stock solution was prepared following the steps described below:

1. 0.2g (200mg) of β -APN was weight into a universal tube.
2. 10 mL of Green's medium was added.
3. The solution was shaken until dissolved and then filter sterilised.
4. It was then stored at 4°C

To make a solution of medium with 200 μ g/mL β -APN, a 1:100 dilution of the 20mM β -APN stock solution in medium was performed. For example, 300 μ l of β -APN stock were added when using a 30000 μ l of media.

4.2 EXPERIMENTAL DESIGN

In order to characterise contraction as a function of time, six TEBM samples were made, each of them representing a time point previously established, as can be seen in **Figure 10**.

At day 0 –when samples were raised to an ALI– all six models were individually photographed in order to keep a record of their original diameter. Additional to this, sample 1 (representing day 0) was then fixed in 3.7% formaldehyde for 24 hours to be further prepared for both histological and Raman analysis. All this was done to characterise and keep track of the initial state of contraction at day 0 of ALI. The whole process was repeated at each different time point and all remaining samples were photographed every time a time point was reached. For



instance at day 3, five pictures were taken, respectively to the remaining time points. Sample 1 was no longer in the six-well plate since day 0 was already being characterised. This experiment was done in triplicate leading to 18 samples in total.

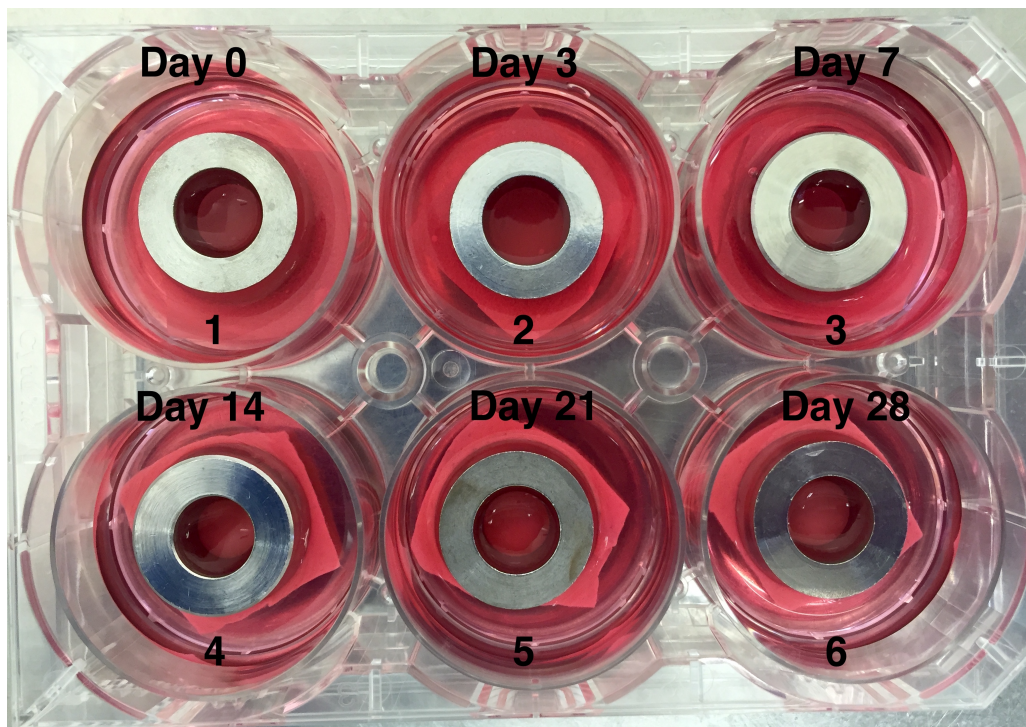


Figure 10. Six TEEM samples in a six-well plate. Each 3D sample is representing a time-interval. Sample 1 representing day 0; Sample 2 representing day 3; Sample 3 representing day 7, and so on until sample 6 representing day 28. All experiments were done in triplicates



5 CHARACTERISATION OF CONTRACTION IN A TEBM MODEL

5.1 DIMENSIONAL ANALYSIS

To measure contraction as a function of time, each individual sample was photographed with a camera placed vertically above the six-well plate. A ruler was placed right next to the sample in order to set a scale bar and be able to use it as a reference when calibrating the image **Figure 13**. Images were opened in ImageJ software to calculate the surface area. The perimeter of the sample was carefully traced on the screen and by using the “analyse feature” the area of the delimited sample was calculated based on the scale bar previously established. The area calculated at day 0 was established as the starting point of contraction and therefore it was set as 100% of the remaining surface area. The area calculated for the remaining time points was reported based on this initial measurement. Once the areas of all time points were calculated, data was transferred to Excel software and plotted as remaining surface area as a function of time.

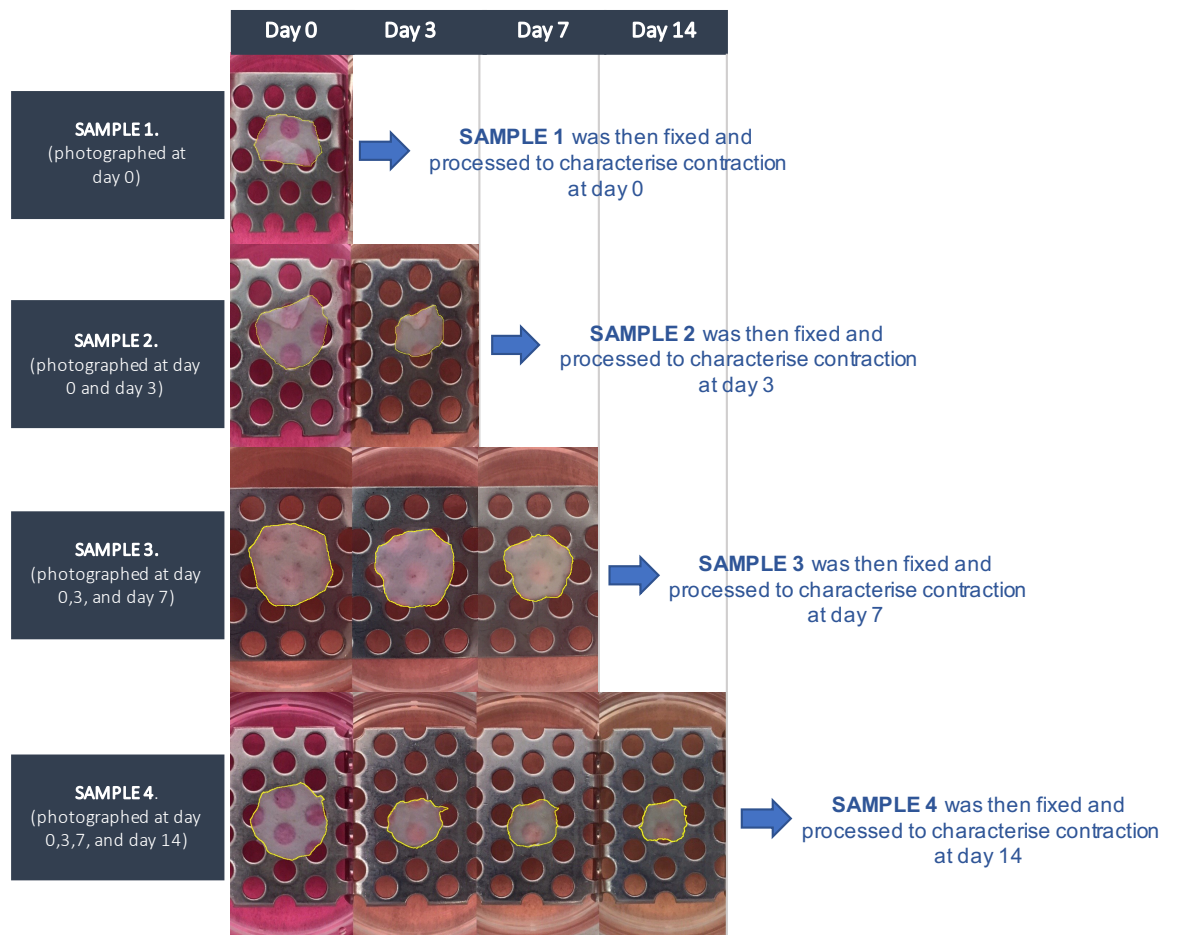


Figure 11. Experimental design explaining how samples were representing a specific time point, and how they were photographed every time a time point was reached. Samples were then fixed to be further analysed once they had reached the time points they were representing. This is why the sample variation.

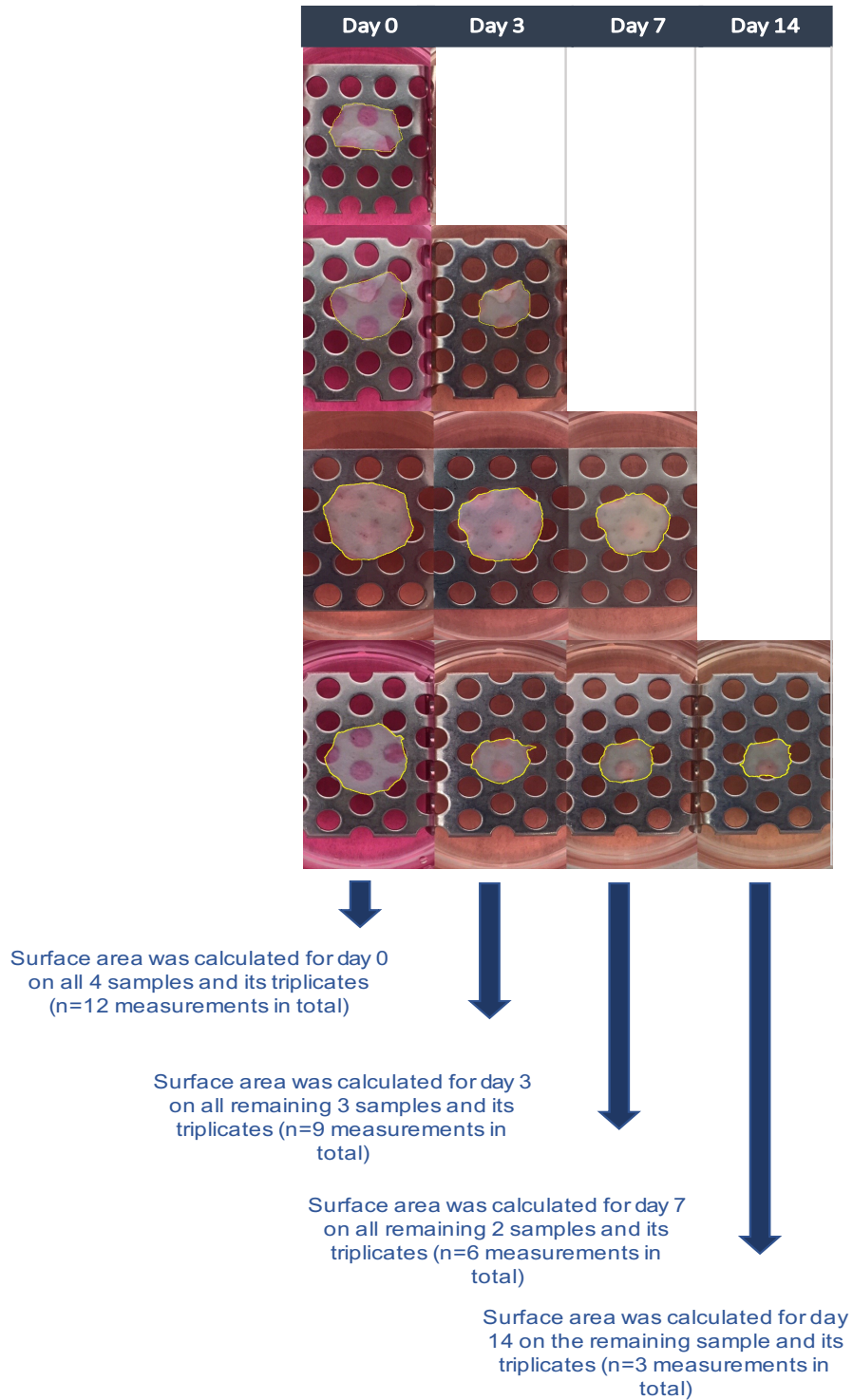


Figure 12. Measurement of the surface area was done with Image J. All samples were photographed at each timepoint. At the starting point of contraction (day

0) all samples were available and hence $n=12$ photographs were obtained to measure surface area for day 0. At day 3, $n=9$ samples were photographed (since samples representing day 0 were already been fixed and processed for further analysis). At day 7, $n=6$ and at day 14 $n=3$. All these was done in triplicates. The absolute average and SD for each time point has been display in Table 11 and Table 12.

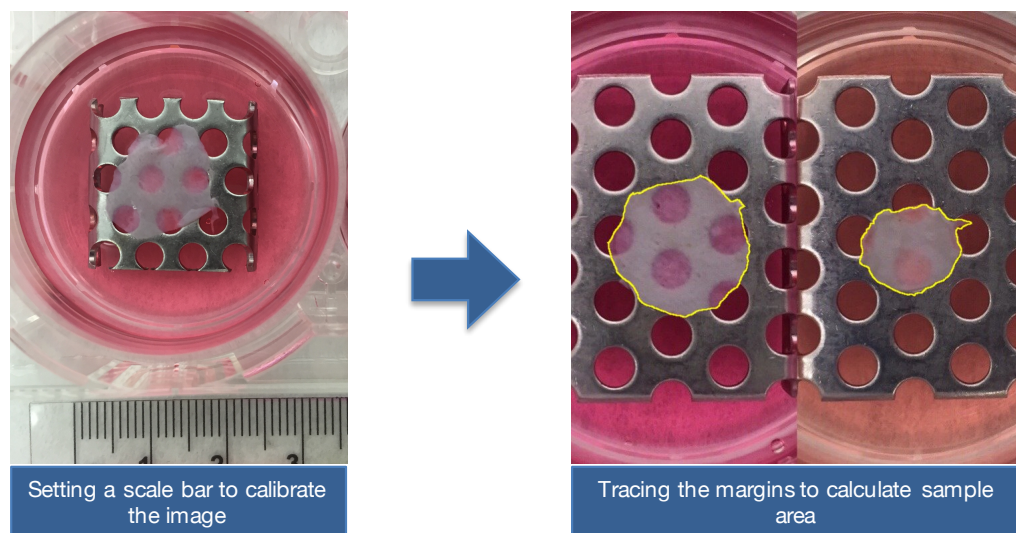


Figure 13. Measuring contraction as a function of time. In the image on the left, a ruler was used as a reference unit of measurement to set a scale and calibrate the image. In the image on the right, the perimeter of the sample was traced using ImageJ software to calculate the surface area at different time points.

5.2 TISSUE PROCESSING

After being fixed in formaldehyde, all six TEBM samples were placed carefully in grey tissue cassettes and labelled accordingly. To replace the water content



MATERIALS AND METHODS

Characterisation of Contraction

in a TEBM Model

within the tissue, samples were wax embedded with a tissue processor Leica TP1020. Therefore, samples were submitted to different alcohol concentrations. After samples were dehydrated, they were then transferred to xylene solution to displace the amount of alcohol within the tissue. To finalize the process, samples are then embedded in paraffin containers to replace the xylene content with wax, **Table 7**. Samples were then removed from the cassettes and they were individually set up in a vertical plane inside metal boxes to get wax embedded. Samples were then cooled on iced surface in a Leica EG1160 (embedding centre) equipment to finally form wax blocks. It is important to mention that samples representing day 21 and day 28 contracted so much that after dehydrating and wax embedding them, they became quite brittle and very difficult to handle. After careful consideration it was then decided that day 21 and day 28 were not crucial for the culturing system of the engineered grafts and so it was decided to continue with only four remaining time points instead of six.

Table 7. Steps and schedule for tissue processor Leica TP1020.

Step	Time
70% IMS (x2)	1 hour each
80% IMS	1.5 hour
85% IMS	1.5 hour
90% IMS	1.5 hour
95% IMS	1.5 hour
100% IMS (x2)	1.5 hour each
Xylene (x2)	1.5 hour each
Paraffin wax (x2)	2 hour each



MATERIALS AND METHODS

Characterisation of Contraction

in a TEBM Model

Following wax embedding, and using a microtome Leica RM2145, tissue sections were cut in 6 μ m and 20 μ m thickness to be used in Haematoxylin and Eosin (H&E), and RS, respectively. For H&E staining, the 6 μ m samples were dewaxed following the protocol described in **Table 9**. For Raman characterisation, dewaxing of the 20 μ m samples was done following the protocol described in **Table 8**. This protocol is different than the one used for H&E staining because samples utilized for Raman analysis were thicker (20 μ m), which required longer time in xylene and alcohol solutions to remove as much as possible the amount of wax.

Table 8. Dewaxing protocol for Raman spectroscopy based on Mian *et al.* 2014

Dewaxing Protocol	
Xylene	30 min
100% Ethanol	5 min
70% Ethanol	5 min
50% Ethanol	5 min
Distilled Water	1 min

Table 9. Dewaxing protocol for H&E staining

Dewaxing Protocol	
Xylene	3 min
100% IMS	1 min
70% IMS	30 sec
Distilled Water	1 min
Haematoxylin	1.5 min
Tap Water	4 min
Eosin	5 min
Tap Water	dunk
Tap Water	dunk
70% IMS	dunk
100% IMS	30 sec
Xylene	dunk

5.3 HAEMATOXYLIN AND EOSIN STAINING

All samples were stained with both H&E following the protocol described in **Error! Reference source not found.** Immediately after, stained tissue sections were mounted and sealed off with cover slips and left to dry for further analysis with Raman Spectroscopy

5.4 RAMAN SPECTROSCOPY

To analyse samples with RS, wax was removed from the sample slide by using the protocol established in Mian et al. ¹⁵³. The protocol is described in detail in **Table 8**. After all four TEBM samples were dried, they were analysed with RS



MATERIALS AND METHODS

Characterisation of Contraction

in a TEBM Model

Thermo DXR Raman Microscope using a laser wavelength of 532 nm diode laser and employing a 50x LWD objective. All samples were analysed under the same parameters previously established. This can be found in **Table 10**. For each sample, twenty random points per layer were analysed making a total of 60 spectra per sample **Figure 14**. These spectra were further compared to H&E stained section images.

Table 10. Raman spectroscopy parameter

Raman Spectroscopy Parameters	
Exposure Time	10 sec
Sample Exposure	20 sec
Corrections	Fluorescence
Laser Power	10 mW
Aperture	25 μ m pinhole
Objective	50x lwd

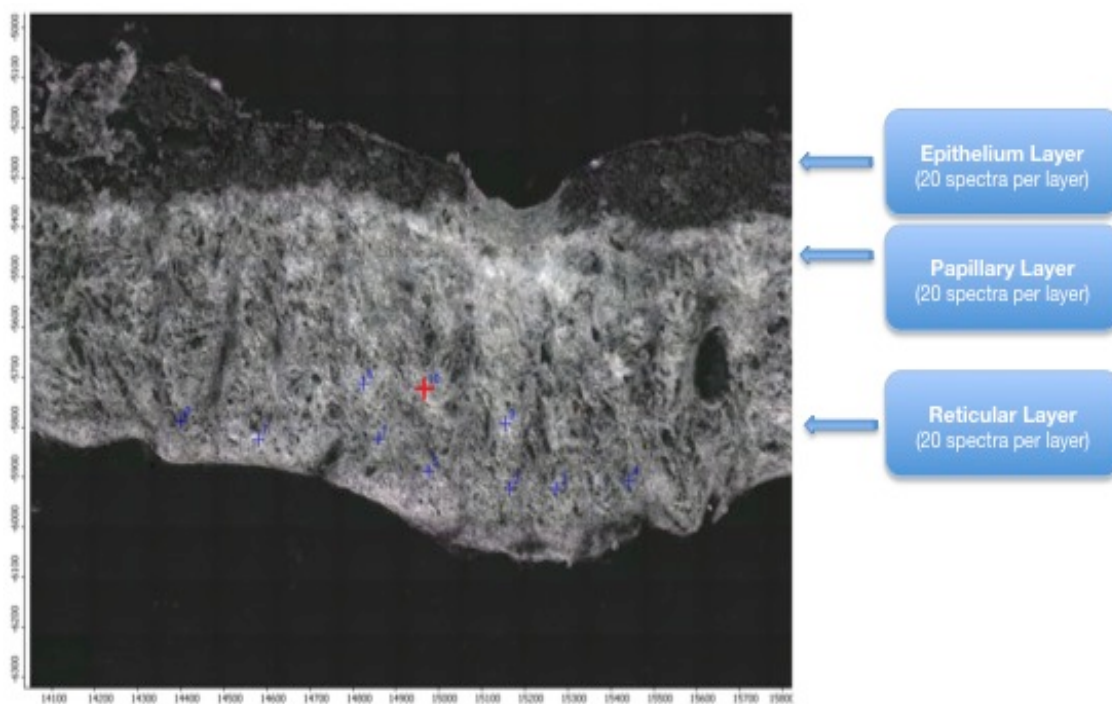


Figure 14. Raman characterisation of TEBM model. Twenty random points collected per layer per sample (time point).

5.4.1 SPECTRAL PROFILES OF CONTRACTION

Establishing Spectral Profiles of Contraction as a Function of Time.

Fluorescence correction (polynomial 6), wax subtraction and baseline correction were performed on all spectra using OMNIC™ Software (Thermo Scientific Nicolet, U.S.A.). For each time point of contraction, with and without β -APN, a spectral profile of each layer (epithelium, papillary and reticular) was obtained by calculating the average of 60 spectra collected from a specific layer within a specific timepoint (this number includes triplicates). This was



MATERIALS AND METHODS

Characterisation of Contraction

in a TEBM Model

performed by using OMNIC and Prism7 Softwares (GraphPad Software, U.S.A.).

5.4.2 MULTIVARIATE ANALYSIS METHODS

Principal Component Analysis (PCA). To understand what is occurring with the *in vitro* oral mucosa grafts as a function of time, it is important to interpret as accurately as possible the information contained in the large amount of spectral data collected. However, an extensive amount of information hidden within that spectral data is to be expected and detecting differences within large amount of spectra can be too complex and sometimes impossible for the eye to identify. PCA is an unsupervised multivariate analysis method that will identify how, where, or at which point samples differ from one another. It also highlights the variables that are mostly responsible for these differences, and whether or not those variables have a co-dependent relationship between them. In this research project, all the spectral data was processed and analysed using The Unscramble X 10.2™ Software (Camo Software, Oslo, Norway). Using PCA method, data was analysed considering variables such as type of samples, time points, spectral regions and layer of the oral mucosa, as it can be seen in **Figure 17**. Previous to the PCA analysis all data was processed using the same conditions: Standard Normal Variate (SNV), offset baseline correction and Savitzky-Golay smoothing.



MATERIALS AND METHODS

Characterisation of Contraction

in a TEBM Model

Organisation of Spectral Data. To analyse all spectral data in an organised manner, a combination of variables were considered to cover three main fronts. To find how the data was different from one another, the type of sample was the variable of choice (e.g. grafts contracting naturally and/or grafts contracting under the influence of β -APN). To find at which point samples differed from one another, different time points were the variable in charge (i.e. contraction at day 0, day 3, day 7, day 14, etc.). Furthermore, to identify where did the spectral data differ between them, spectral regions were the variables of choice (e.g. lipids, amides, hydroxyproline and proline, fingerprint region, etc.). Taking into consideration these three variables, the multivariate analysis of the spectral data was organised and can be visualized in **Figure 15** and **Figure 16**. This template was applied in each of the three layers of the oral mucosa model for both experiments.

Cluster Analysis (CA). To corroborate the similarities and differences found by PCA, spectral data was also submitted to a Cluster analysis method. Cluster analysis is an unsupervised multivariate analysis method that aims to group samples into specific number of clusters based on their similarities. This method organises data into different groups, which reflect useful or relevant information. In this instance for example, contraction as a pathological process occurring in the oral mucosa model could have some spectral variations over a specific amount of time. Cluster analysis was applied on this spectral data to detect how these spectral variations organised it selves in different clusters. The



MATERIALS AND METHODS

Characterisation of Contraction

in a TEBM Model

Wards method was the method of choice for the cluster analysis. This analysis calculates the existing difference between one specific sample and the cluster centroid and also between two samples. In this way, a set of samples randomly allocated in different clusters will reallocate into the cluster that has the shortest distance between the sample's value and the cluster centroid.

Day 14	Day 7	Day 3	Day 0		
				General	Day 3
				Fingerprint	
				Amides	
			E,	Amide I	
				Amide II	
			E, P,	Amide III	
			E,	Nucleic Acids & Aminoacids	
			E,	Lipids	
				Hydroxyproline & Proline	
				General	Day 7
				Fingerprint	
				Amides	
			E, R	Amide I	
			R	Amide II	
			P, R,	Amide III	
			P	Nucleic Acids & Aminoacids	
				Lipids	
				Hydroxyproline & Proline	
				General	Day 14
				Fingerprint	
				Amides	
				Amide I	
				Amide II	
				Amide III	
				Nucleic Acids & Aminoacids	
			E,	Lipids	

Figure 15. System template used to organise and analyse spectral data per layer. E: indicates regions that were discussed in the epithelium layer. P: is marking regions discussed in papillary layer. R: indicating regions discussed in reticular layer. This system was applied on every layer for both TEBM and TEBM with β -APN).

Timepoints. Contraction in oral mucosa models with β -APN						
Day 14	Day 7	Day 3	Day 0			
				General	Day 0	Timepoints. Contraction in oral mucosa models withouth β -APN
				Fingerprint		
				Amides		
				Amide I		
				Amide II		
				Amide III		
				Nucleic Acids & Aminoacids		
				Lipids		
Hydroxyproline & Proline						
		P E P P E		General	Day 3	
				Fingerprint		
				Amides		
				Amide I		
				Amide II		
				Amide III		
				Nucleic Acids & Aminoacids		
				Lipids		
Hydroxyproline & Proline						
	P, R E P, R P, R			General	Day 7	
				Fingerprint		
				Amides		
				Amide I		
				Amide II		
				Amide III		
				Nucleic Acids & Aminoacids		
				Lipids		
Hydroxyproline & Proline						
P, R P, R P, R				General	Day 14	
				Fingerprint		
				Amides		
				Amide I		
				Amide II		
				Amide III		
				Nucleic Acids & Aminoacids		
				Lipids		
Hydroxyproline & Proline						

Figure 16. Comparison template of control TEBM vs TEBM/ β -APN model. This system corresponds to the analysis of spectral data. E: indicating regions analysed by the epithelium layer. P: regions discussed in the Papillary layer. R: regions discussed in the Reticular layer.

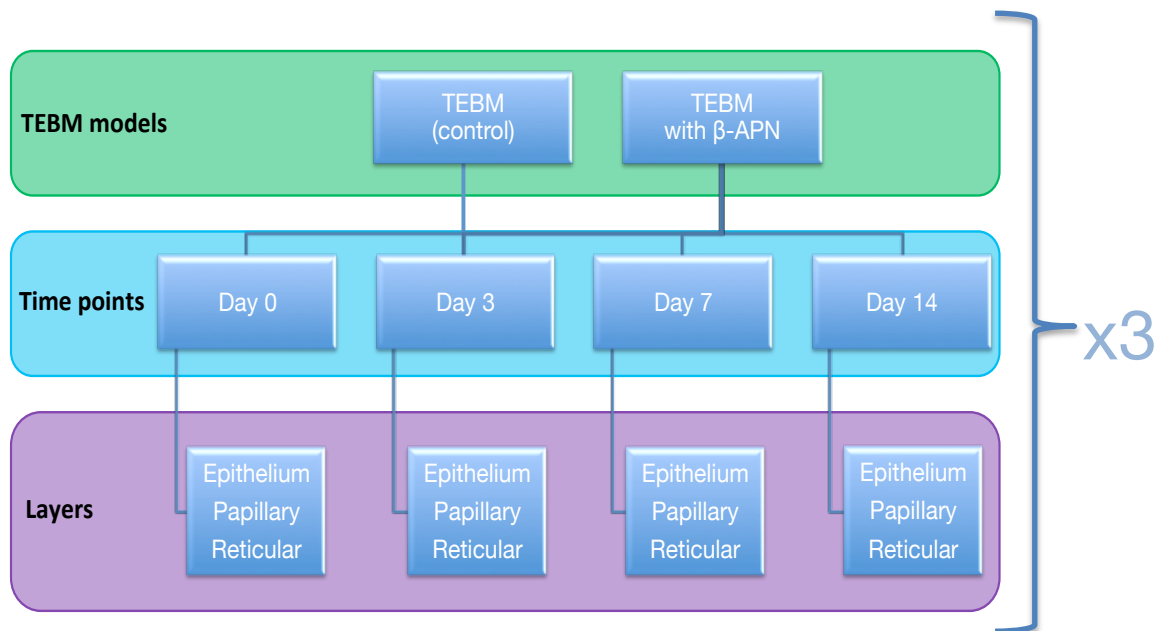


Figure 17. Experimental design for Raman data with the main variables considered for the analysis of the spectral data.



RESULTS & DISCUSSION.

Characterising Contraction in a TEBM Model with Raman Spectroscopy

6 RESULTS AND DISCUSSION

Due to their versatility, tissue-engineered buccal mucosa grafts have been used not only for intraoral applications, to repair cleft palates or for reconstructive surgery in head and neck cancer, but also in extraoral applications to replace scarred tissue in the urethra. A central issue in these applications is that, when applied clinically in the patient, tissue-engineered buccal mucosa grafts exhibit contraction that contracts further after implantation to the injury site which can lead to incorrect functionality of the tissue. Although extensive research has been dedicated to the study of contraction in oral mucosa grafts, there is an urgent need for a better understanding of the nature of contraction.¹²⁰¹¹⁹ Currently, there is no method available to accurately measure the crosslinking of collagen at the biochemical level, as conventional assays (Electrochemiluminescence ECLIA to indirectly measured collagen synthesis through the concentration of amino terminal propeptide of type I (P1NP), and Sircol soluble collagen assay) are tedious and not very reliable. Raman spectroscopy is capable of identifying biochemical changes occurring in collagen type I, III and IV. Therefore, this gives us the opportunity to analyse and characterise the progressive process and extent of physical contraction occurring in oral mucosa grafts using Raman spectroscopy technique. This chapter reports on the results obtained from characterising the progressive process of contraction with Raman spectroscopy, over a period of 14 days.

6.1 DIMENSIONAL ANALYSIS

The extent of contraction occurring in a TEBM model was analysed at different time points. Contraction at day 0, 3, 7, 14, 21 and 28 were the previously established time intervals. Following the same protocol of preparation, six TEBM models were produced, one for each time point. The degree of contraction progresses as a function of time. Whenever a time point was reached, all samples were photographed **Figure 18**. Subsequently, the sample assigned to that time interval was fixed in order to be analysed and characterised to record the extent of contraction achieved up until that time point.

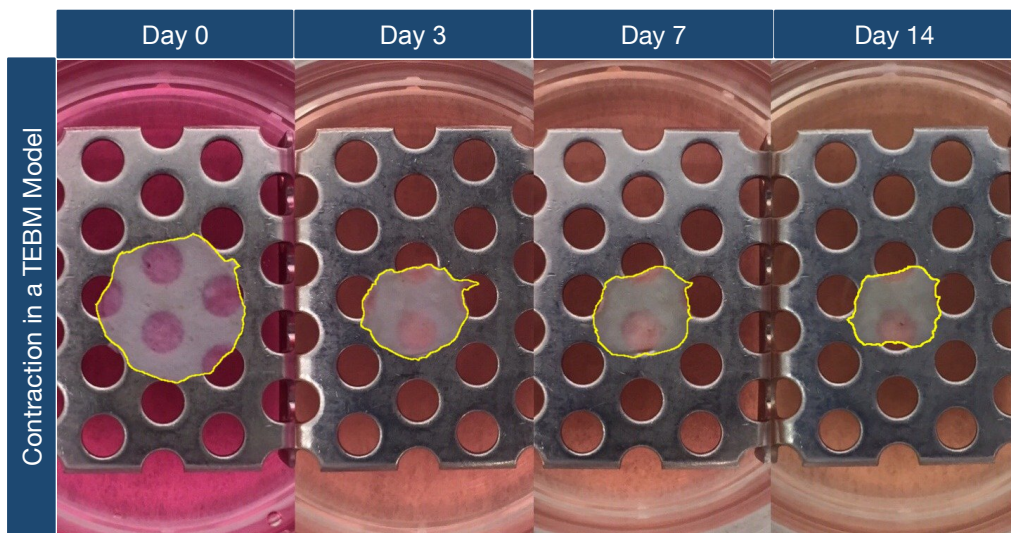


Figure 18. Digital image of sample #4 showing the extent of contraction from the starting point at day 0 up until day 14 of *in vitro* culture. This is a representation of sample 4 at different time points. Each image is showing



RESULTS & DISCUSSION.

Characterising Contraction in a TEBM Model with Raman Spectroscopy

contraction at a different day. Sample #4 was assigned as day 14, once it reached day 14, it was then fixed and processed for further analysis.

The graph in **Figure 19** represents the extent of contraction seen per time point. An average of the remaining surface area and their respective standard deviation values (SD) have been calculated and included in **Table 11**. All triplicates followed a similar tendency when contracting and according to the dimensional analysis, the highest activity of contraction occurred between day 0 and day 3. As it can be seen in **Table 11**, the remaining surface area at day 3 is around 52% in average. Then from Day 3 to Day 7 samples contracted slightly more, showing a remaining area of 37% in average. As time point increases, so does the extent of contraction and hence the remaining surface area is slightly reduced. From day 7 to day 14 the graph reaches a plateau indicating not much of a difference between the remaining area of day 7 and day 14.

Table 11. Percentage of contraction in a TEBM model (and its triplicates). The average remaining surface area was calculated by including all the available measurements per time point.

% of Remaining Surface Area in TEBM Models (triplicates)			
Time points (days)	Average (cm ²)	SD	%
0	0.813 (n=12)	0.10	100
3	0.423 (n=9)	0.05	52
7	0.300 (n=6)	0.06	37
14	0.286 (n=3)	0.03	35

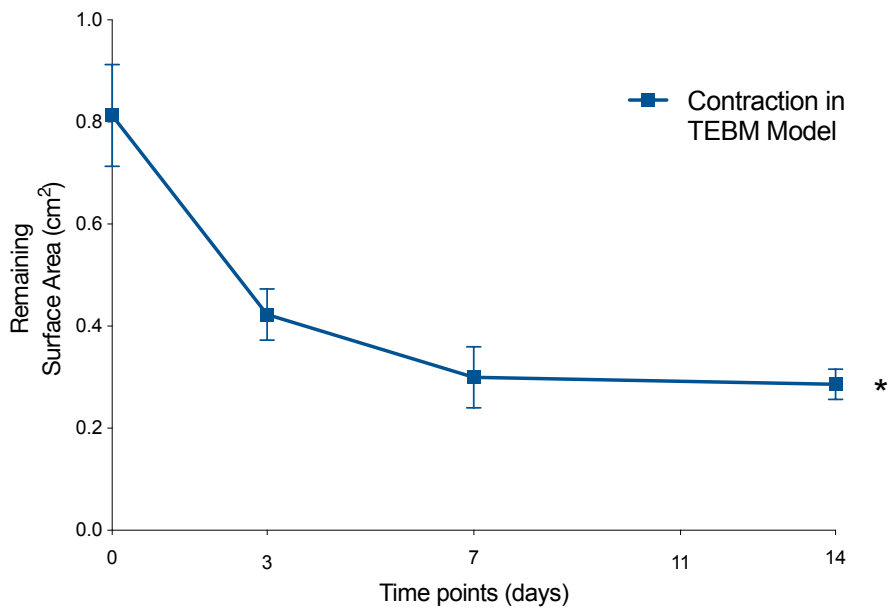


Figure 19. Percentage of remaining surface area as a function of time. the solid navy-blue line represents the average and SD calculated for each time point. (one-way t test was performed, $p < 0.0214$, *)

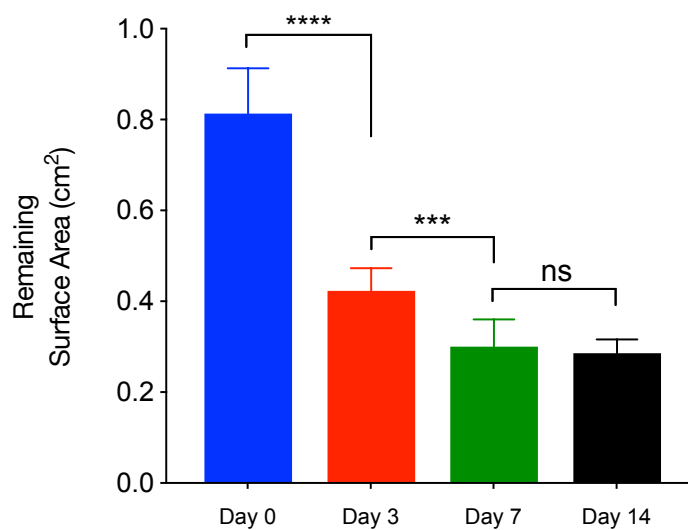


Figure 20. Unpaired t-test statistical analysis of surface area of control model as a function of time. day 0 vs day 3 ($p < 0.0001$, ****). Day 3 vs day 7 ($p < 0.0007$, ***). Day 7 vs day 14 ($p < 0.7106$, ns).



RESULTS & DISCUSSION.

Characterising Contraction in a TEBM Model with Raman Spectroscopy

6.2 HISTOLOGICAL ANALYSIS

When tissue sections are stained with H&E, the hemalum is chemically binded to the DNA within the nuclei, giving the appearance of blue dots when seen in the histological images. In this case, the blue dots on any of the images shown below, strongly suggests the presence of nucleus where the stain can bind to. As can be seen in **Figure 21** all TEBM samples exhibited the formation of a stratified epithelium characteristic of the oral mucosa. A progressive increment in the stratified layers of the epithelium can be appreciated as a function of time. Therefore, there is a notorious difference between day 0 and day 7, where the epithelium layer seemed to be thicker when compared to the starting point of contraction. Similar case with day 14. As time points get longer, the thickness of the epithelium increases. Images in this figure show the similarity between these engineered models and native oral mucosa structure.

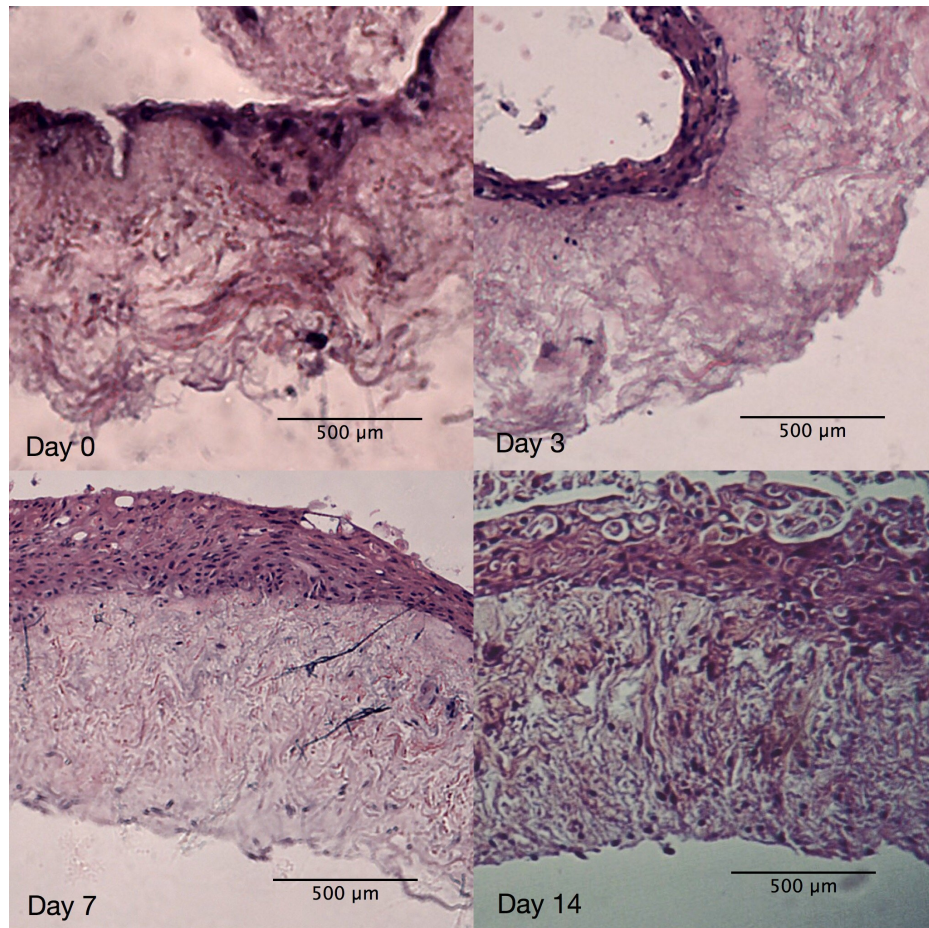


Figure 21. Histological images (taken with 20x objective) of all four TEBM models. In all four images it can be seen how the epithelium increases in thickness as a function of time.

6.3 RAMAN SPECTROSCOPY CHARACTERISATION

All four samples and their respective triplicates were analysed with Raman Spectroscopy. The epithelium, papillary and reticular layer were the three main layers from the TEBM models to be characterised. Twenty spectra per layer were collected. Considering that each sample was made in triplicates, there were 60 spectra per layer/time point. An average of those 60 spectra was calculated,



RESULTS & DISCUSSION.

Characterising Contraction in a TEBM Model with Raman Spectroscopy

making a spectral profile for each layer at each specific time point. The purpose of this was to establish and compare the spectral profiles and detecting the differences occurring between each day of contraction.

6.3.1 EPITHELIUM LAYER

Briefly, the oral epithelium is the outermost layer directly exposed to the oral environment and is mainly formed by squamous cells that are uniformly distributed along the basement membrane. As cells start differentiating into keratinocytes, they start migrating to the uppermost layers forming what is known as the stratified epithelium. In this study, contraction in the TEBM models was characterised and analysed. The epithelium of four different samples was analysed and their spectra were averaged to calculate a spectral signature. A spectral profile for each specific time point has been illustrated in **Figure 22**. The highest activity of contraction was seen between day 0 and day 3.

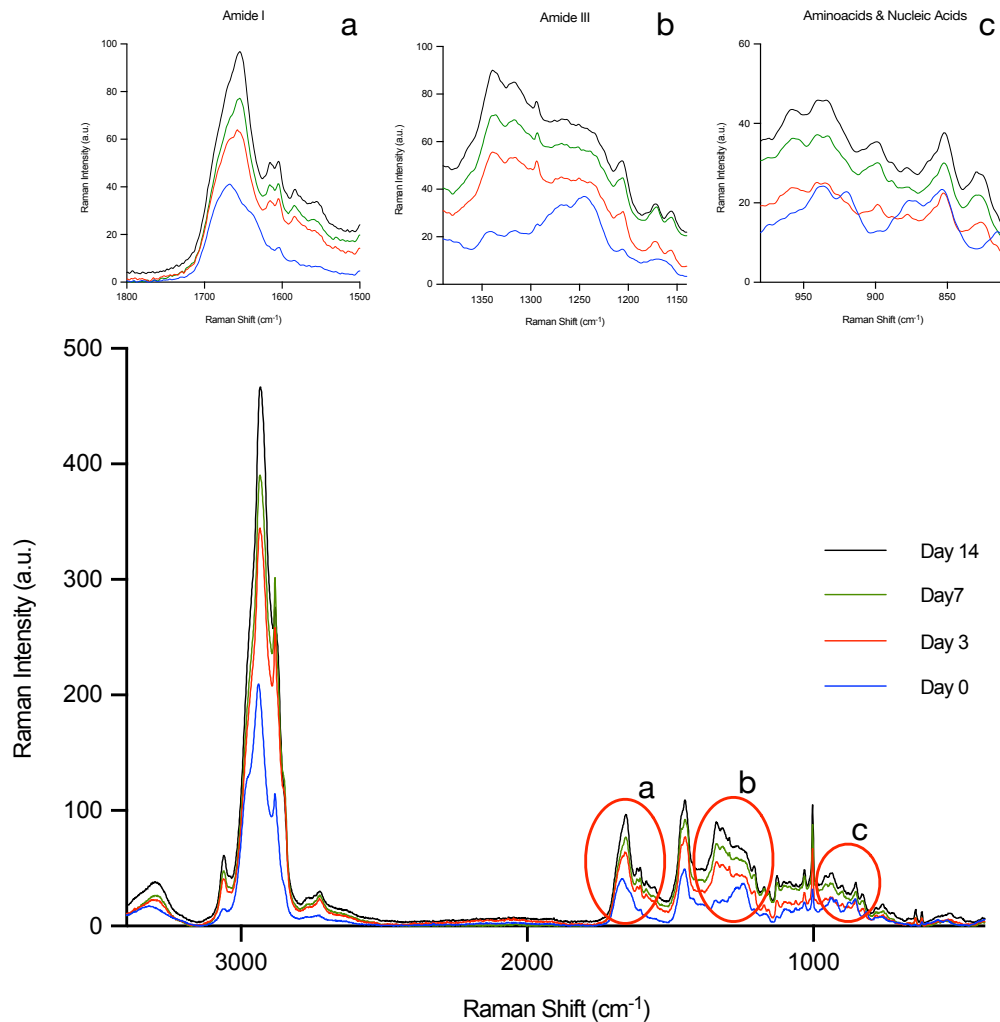
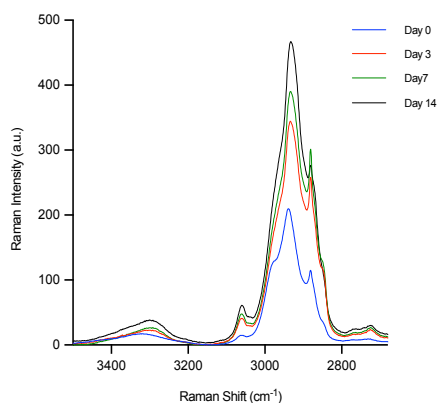


Figure 22. Raman characterisation of contraction in the epithelium layer at different time points. Each time point is represented by their spectral profile. Each profile is an average of 60 spectra. In this figure, the most notorious differences between time points have been highlighted and expanded. These regions have been labelled as followed, a) Amide I, b) Amide III, and c) Aminoacids & Nucleic Acids region.

Together with this, the qualitative Raman analysis of contraction at the epithelium level indicates that most notorious changes were reflected at day 3.

Figure 22 highlights spectral differences that are easy to identify by the naked eye, being Amide I, Amide III and Amino acids regions the most notorious. To validate these observations, Raman statistical analysis –via MVA techniques– was performed on all spectral data to spot the most relevant biomarkers in an accurate manner. The main spectral differences highlighted by the PCA method were Lipids, Amide I, Amide III and Amino acids region, which are described below.



Lipids. At the initial state of contraction, at day 0, there is a lower activity on the stretching vibration of the CH bond than in day 3. This stretching vibration is reflected at 2918 cm^{-1} , coming from the CH located mainly in lipids²⁷. According to the PCA of lipids region in **Figure 23**, by day 3 into contraction this activity has notoriously increased causing a separation between both time points. The stretching vibration of CH bond is now higher in day 3. It is also noted that there is a higher activity from the asymmetric stretching (v^{as}) vibration from both the CH_3 and CH_2 bonds, which is reflected at 2882 cm^{-1} . Since lipids are a main component of cell membranes, this increase in activity of all CH bonds could be justified as an increase in the rate of triglycerides (TG) content. According to Ponec et al., the rate of TG content is somehow related to the stage of differentiation of keratinocytes cells.¹⁵⁴ They have previously

reported that the TG content increases in air-exposed stratified keratinocyte cultures.¹⁵⁴ It could be possible that by day 3 there has been an increase in the number of keratinocytes, due to the proliferation and mainly differentiation of squamous cells during the re-epithelialisation process, resulting in the stratification of the epithelium layer.

At the final stage of contraction, from day 7 to day 14, notorious changes were detected. By day 7, the intensity of peaks at 2881 and 2846 cm^{-1} was higher than the average value. Which translates into a higher amount of activity from the $\nu^{\text{as}}(\text{CH}_3, \text{CH}_2)$ and the $\nu^{\text{s}}(\text{CH}_3)$, respectively.²⁷ However, according to the PCA in **Figure 24**, it seems that the intensity of these two bands significantly reduced by day 14. Since the re-epithelialization process is mostly done by day 14, differentiation and migration of keratinocytes is notoriously reduced. Hence, proliferation and adhesion between keratinocyte membranes is considerably lower than the activity presented at day 7.

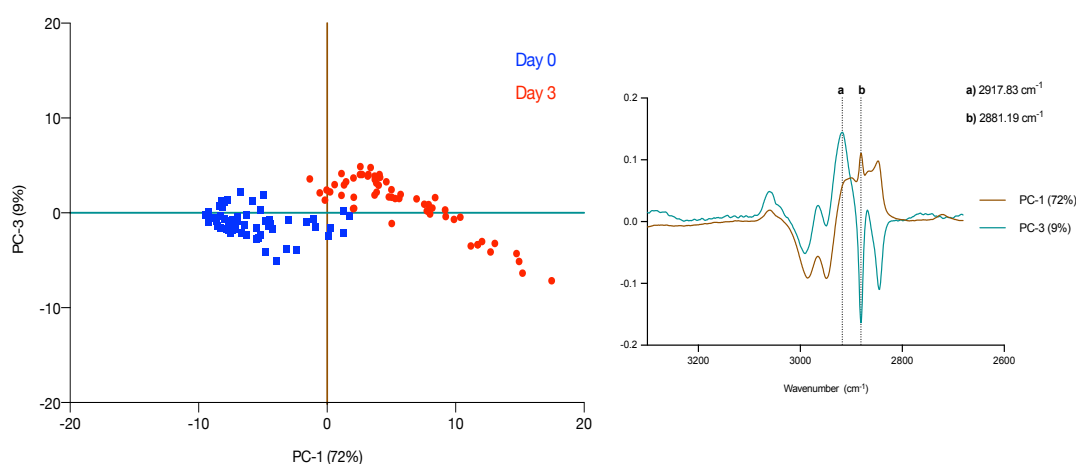


Figure 23. PCA of lipids region ($3100\text{-}2600\text{ cm}^{-1}$) at the initial stage of contraction. Spectral data from day 0 and day 3 are separated mostly by peaks at 2881 cm^{-1} (PC-1 in brown) and 2918 cm^{-1} (PC-2 in green). Band at 2881 cm^{-1} (PC-1) is responsible for 72% of the separation, while the 2918 cm^{-1} PC-2 accounts for 9%.

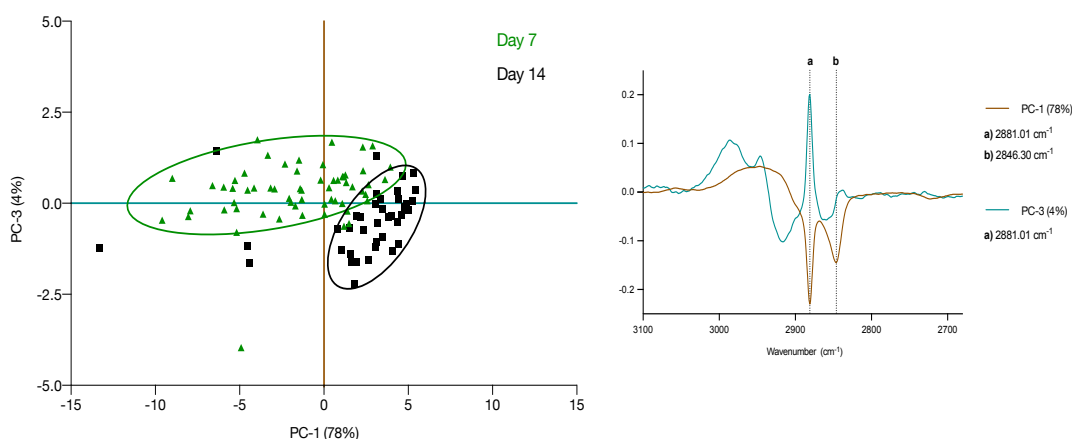
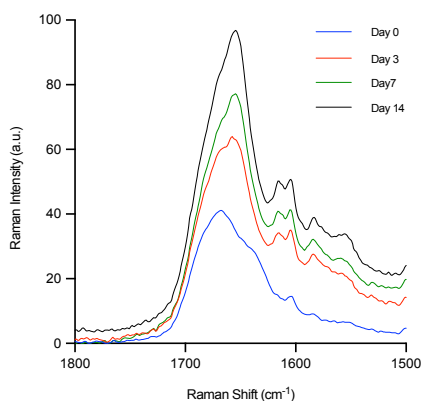


Figure 24. PCA of lipids region ($3100\text{-}2600\text{ cm}^{-1}$) at the final stage of contraction. Spectral data from day 7 and day 14 were compared and analysed. Bands at 2881 cm^{-1} and 2846 cm^{-1} account for 78% of the variation. Peak at 2881 cm^{-1} was considered and individual component responsible for 4% of the separation.



Amide I. As the starting point of contraction, the spectrum for day 0 reflected an amide I band at 1668 cm^{-1} and a peak at 1605 cm^{-1} . After three days into contraction, both peaks increased in intensity and a downshift from 1668 to

1658 cm^{-1} was noticed. This downshift in frequency reflects a change in the



RESULTS & DISCUSSION.

Characterising Contraction in a TEBM Model with Raman Spectroscopy

secondary structure of the protein, going from an unordered structure to an α -helix structure.^{27,70} In agreement with this, the PCA for Amide I region shows that most samples at day 0 have a stronger tendency towards an unordered structure, separating themselves from samples at day 3. Responsible for this separation is peak at 1676 cm^{-1} , characteristic to unorganised secondary structures,¹³¹ and represented by PC-2. Whereas at day 3, an average of all samples is reflecting Amide I bond at 1658 cm^{-1} . Accordingly, the score plot from **Figure 25A** is showing that most of the samples from day 3 have a lower activity than the average with respects to peak 1676 cm^{-1} . It might be indicating a change in the secondary structure of a protein into the formation of an α -helix structure. This observation did not correlate with Dehring et al.²⁵, who considered the aging process as a chemical factor that caused the crosslinking of collagen fibres resulting in an increase in a disordered secondary structure in the protein molecule. On the other hand, Guilbert et al. supported the statement that no conformational changes occurred in the triple-helical structure of collagen I during glycation process.¹⁵⁵

However, with the increase of crosslinking, it is reasonable to expect continuous formation of α -helix structure from the polypeptidic chains, increasing the rigidity of the oral mucosa graft. Together with this, two detectable peaks that were not present at day 0 emerged at 1616 and 1584 cm^{-1} at day 3 onwards into contraction. These peaks are representative of the stretching vibration of C-C from tyrosine and the bending mode of the C-C bond from phenylalanine,



RESULTS & DISCUSSION.

Characterising Contraction in a TEBM Model with Raman Spectroscopy

respectively.^{131,27} It is well-documented that excessive activity from LOX enzyme promotes the excessive crosslinking of collagen fibres.¹⁵⁶ However, LOX is incapable of inducing reactions without the presence of a cofactor known as lysyl-tyrosyl-quinone (LTQ), which derives from the di-oxo-phenylalanine (DOPA) complex.¹⁵⁷ This could be indicating that after the starting point of contraction, crosslinking of polypeptide chains resulted from the activation of LOX enzyme through cofactor LTQ, which oxidised the ϵ -amino group of lysine residues into highly reactive aldehydes. Justifying the presence of both tyrosine (1616 cm^{-1}) and phenylalanine (1584 cm^{-1}) at day 3 of contraction **Figure 25D**. Additionally, it would explain why most of the samples at day 3 have a higher activity of both peaks than samples at day 0.

Furthermore, by day 7 amide I band kept reflecting a downshift in frequency. It went from 1658 at day 3 to 1655 cm^{-1} . However, little to no difference was seen regarding the presence of both tyrosine and phenylalanine at this stage of contraction **Figure 26**. This correlates with the little difference in contraction seen between both time points.

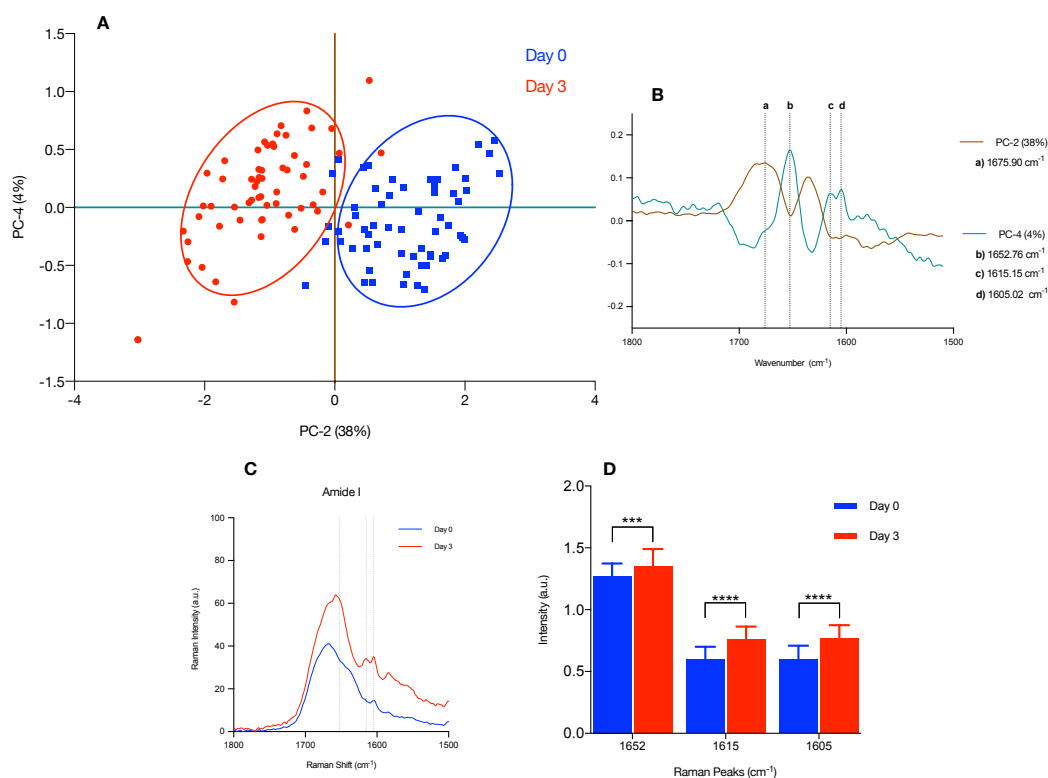


Figure 25. **A)** PCA score plot of the amide I region: According to the PCA analysis, spectral data from day 0 and day 3 are mostly separated by PC-2 and PC-4 loadings. **B)** PC-2 accounts for 38% of the variation, represented by a positive value of 1676 cm^{-1} band. Bands at 1658 , 1615 and 1605 cm^{-1} are considered the fourth component with a variation of 4%, showing a direct correlation between them. **C)** Spectral profile for day 0 in blue and day 3 in red, with all three peaks indicated by dotted line. **D)** T-test analysis of the direct correlation between 1652 , 1615 and 1605 cm^{-1} bands at day 0 and day 3. Mean and SD values were reported as [mean, SD]. For peak at 1652 , values were [1.2734, 0.0995] for day 0 and [1.3495, 0.1411] for day 3. For peak at 1615 , values were [0.5987, 0.1014] for day 0 and [0.7573, 0.1057] for day 3. For peak at 1605 , values were [0.5976, 0.1118] for day 0 and [0.7687, 0.1065] for day 3.

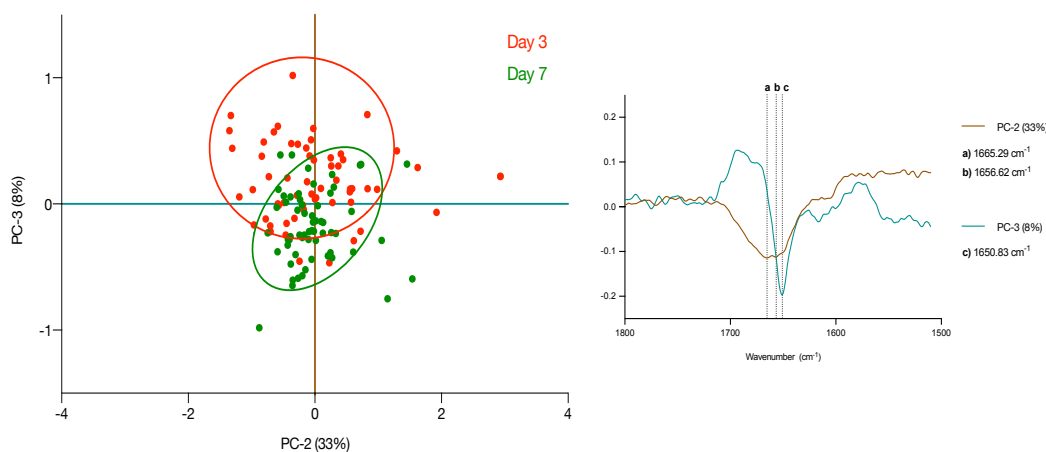
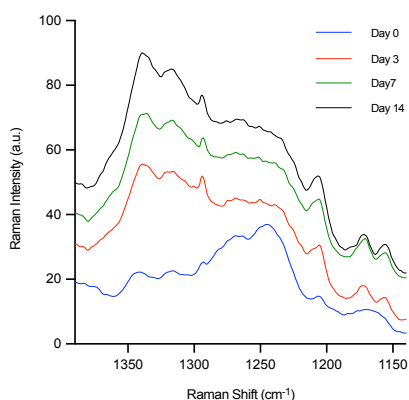


Figure 26. PCA score plot of the amide I region: According to the PCA analysis, spectral data from day 3 and day 7 are mostly separated by PC-2 and PC-3. PCA loadings of the amide I region: PC-2 accounting for 33% of the variation, represented by negative values of 1665 and 1657 cm^{-1} bands. PC-3, represented by a negative value of 1651 cm^{-1} and accounting for 8% of the variation.



Amide III. At day 0 of contraction, amide III bands were reflected at 1245 and 1268 cm^{-1} at much more higher intensities than peaks at 1316 and 1341 cm^{-1} . However, from day 3 onwards, sharp peaks at 1245 and 1268 cm^{-1} were hardly seen and deformed into blunt irregular bands.

Together with this, the peak at 1339 cm^{-1} had raise and reached a higher intensity when compared to the 1245 cm^{-1} band (**Figure 27C**). This goes in agreement with the PCA statistical analysis in **Figure 27A**, where similarities and differences within the Amide III region (1390-1140 cm^{-1}) are shown. According



RESULTS & DISCUSSION.

Characterising Contraction in a TEBM Model with Raman Spectroscopy

to the PCA, the peaks responsible for separation between day 0 and day 3 are 1336 and 1245 cm^{-1} , representing 35% of the variation (PC-2). Based on the corresponding loadings, these two bands are indirectly correlated, hence if one increases the other one decreases **Figure 27B** (see loading PC-2). This correlates with **Figure 27D**, where the intensity at day 0 is significantly higher for 1243 cm^{-1} band ($p < 0.0001$) and significantly lower for the 1335 cm^{-1} band ($p < 0.0001$), when compared to day 3. Therefore, as reported by the PCA statistical analysis, there is a higher activity of the stretching vibration of C-N from the amide bond, 1245 cm^{-1} , than in day 3. Interestingly, by day 3 this stretching vibration has reduced its activity and instead the twisting vibration of CH_3 and CH_2 has now increased, 1336 cm^{-1} . Previous literature has reported that LOX transforms lysine residues into aldehydes via oxidation of the ϵ -NH group.¹⁵⁸ It could be possible that at day 0 there was no notorious activity from the CH_3 and CH_2 twisting vibration since LOX was in the process of inducing the aldehyde formation. Once the transformation had occurred, reactive aldehydes formed at the end of the side chains can easily react with other reactive terminal groups. Hence explaining an increase of the twisting vibration of CH_3 and CH_2 (mostly located in the side chains) as a result of the re-accommodation of polypeptidic fibres. Intensity in all peaks mentioned above kept slightly increasing as a function of time.

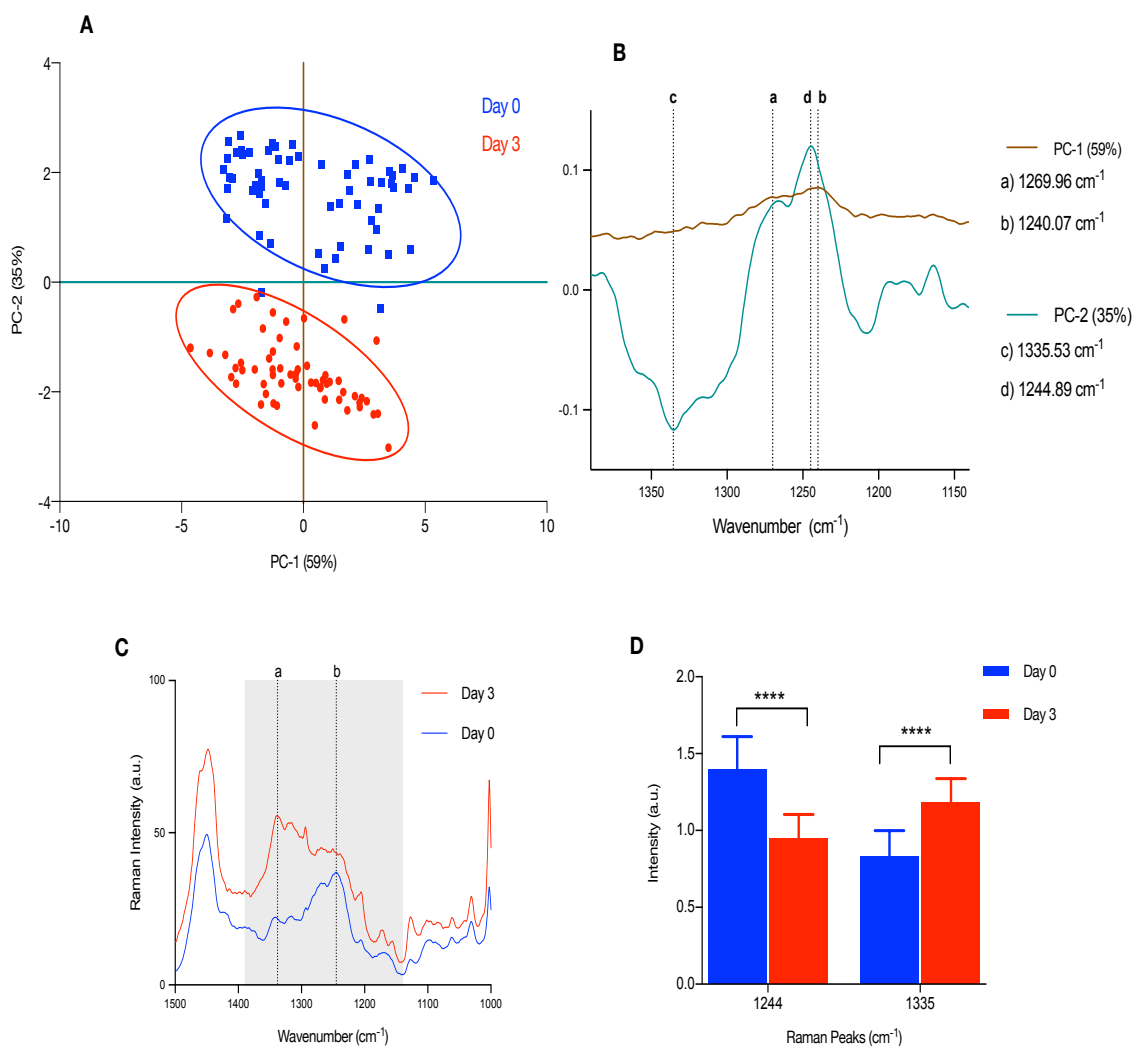


Figure 27. **A)** PCA score plot of the amide III region: According to the PCA analysis, spectral data from day 0 and day 3 are mostly separated by peaks at 1336 and 1245 cm^{-1} . **B)** PCA loadings of the amide III region: PC-1 accounting for 59% of the variation, represented by positive values of 1270 and 1240 cm^{-1} bands. PC-2, represented by a positive and negative value of 1244.89 and 1336 cm^{-1} , respectively. These two peaks are considered the second component with the next highest variation of 35%, showing an indirect correlation. **C)** The amide III region is highlighted in grey, spectral profile for day 0 in blue and day 3 in red, with both peaks indicated by dotted line, a)1336, b)1245. **D)** **T-test analysis** of the indirect correlation between 1245 and 1336 cm^{-1} bands at day 0 and day 3. Mean and SD values were reported as [mean, SD]. For peak at 1245, values were [1.3980, 0.2134] for day 0 and [.9483, 0.1563] for day 3 here. For peak at 1336, values were [0.8308, 0.1687] for day 0 and [1.1848, 0.1534] for day

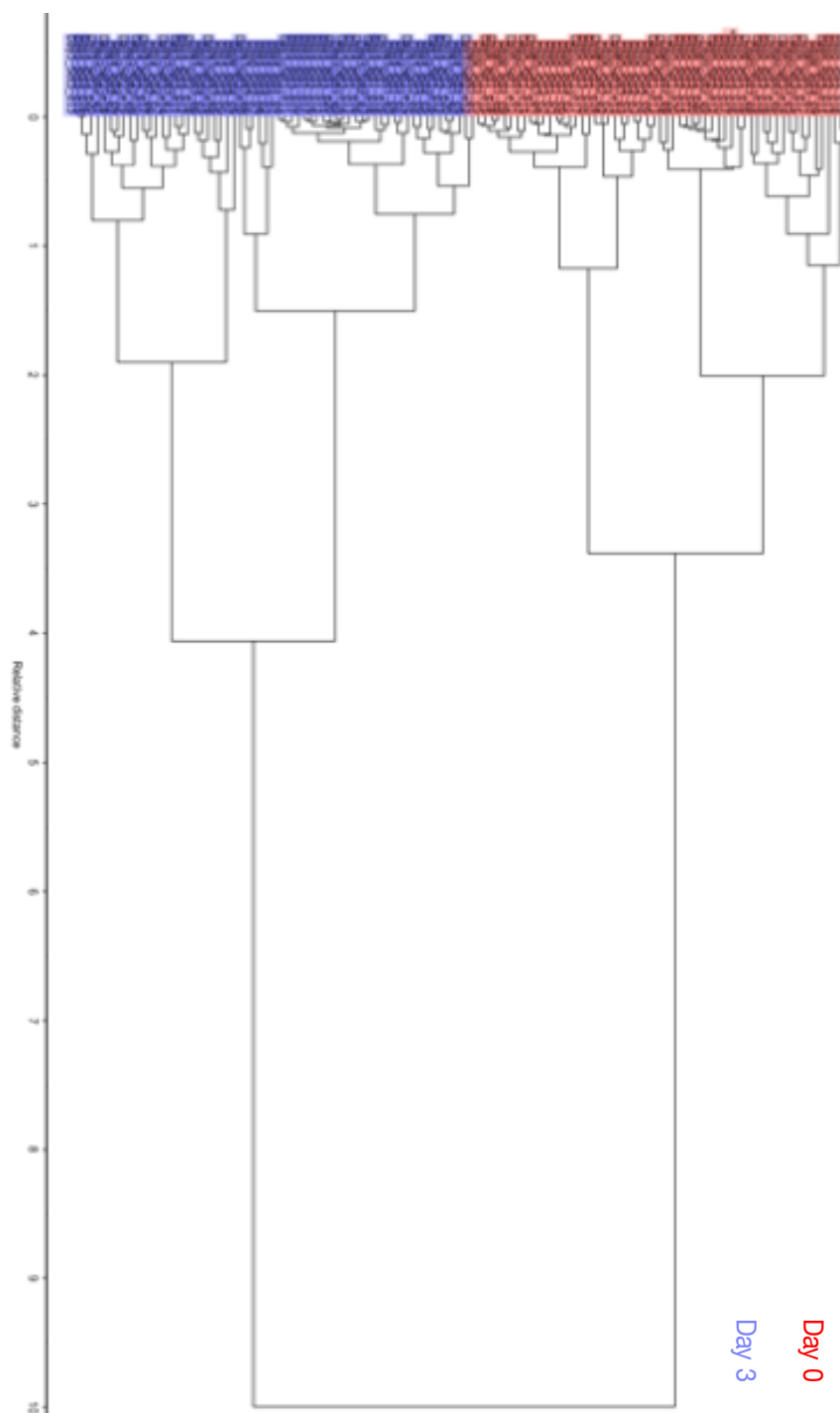
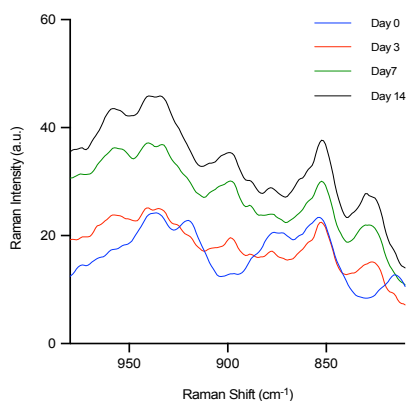


Figure 28. CA of Amide III region on Day 0 and Day 3 of contraction in a TEBM model. The unsupervised method clustered Day 0 and separate it from Day 3, complementing the results of the PCA.



Amino and Nucleic Acids. At day 0 on the initial state of contraction, well-defined peaks were reflected at 815, 854, 876, 898, 920 and 937 cm^{-1} . By day 3, biochemical changes due to contraction produced several spectral differences. Based on the statistical analysis, the PCA of amino acid and nucleic

acids region (spectral range 980-600 cm^{-1}) is shown in **Figure 29**. Similarities and differences between samples is shown based on the existing variation, representing 77% between both PC-1 and PC-3 accounting for 73% and 4%, respectively. A clear separation between time points can be seen when applying these two components. According to PC-1, Day 0 is characterised by a higher activity of stretching vibration of C-C from proline and lipids residues, 920 and 873 cm^{-1} , respectively²⁷. However, distinctly from day 0, these vibrations have reduced in activity by day 3 and instead an increase in activity of the out-of-plane breathing ring of tyrosine is detected, 828 cm^{-1} ²⁵²⁷. This characterisation goes in conjunction with a higher activity of stretching C-C bond from the skeleton of a polypeptide chain, reflected at 903 cm^{-1} . Since contraction has occurred by day 3, it is reasonable to assume that crosslinking has reflected into a higher number of C-C skeletal vibration modes during the formation of α -helix structures and rearrangement of collagen fibres. Moreover, the notorious increase of out-of-plane vibration from tyrosine ring at day 3 could be an indication of the presence of LTQ cofactor located in the catalytical site of LOX

enzyme. The C=O group from LTQ binds to the ϵ -NH from the lysine side chain, resulting in an aldehyde end product. Base on the MVA, the increase activity of tyrosine ring at day 3 of contraction could be indicative of higher activity from LTQ cofactor.

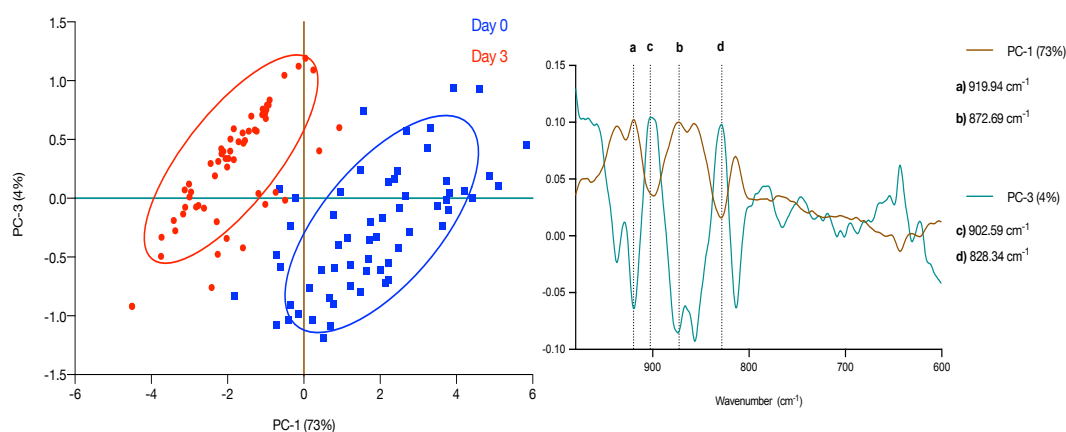


Figure 29. A) PCA score plot of the amino acids region: According to the PCA analysis, spectral data from day 0 and day 3 are mostly separated by peaks at 920 and 873 cm^{-1} . **B)** PCA loadings of the amino acids region: PC-1 accounting for 73% of the variation, represented by positive values of 920 and 873 cm^{-1} bands. PC-3, represented by positive values of 903 and 828 cm^{-1} . These two peaks are considered the third component accounting for a variation of 4%.

6.3.2 PAPILLARY LAYER

While it may be true that the highest activity of contraction was seen from day 0 to day 3, biochemical changes occurring over the course of three days did not manifested abruptly on day 3 for the papillary and reticular layers. Instead, qualitative Raman data showed that most biochemical changes occurring during

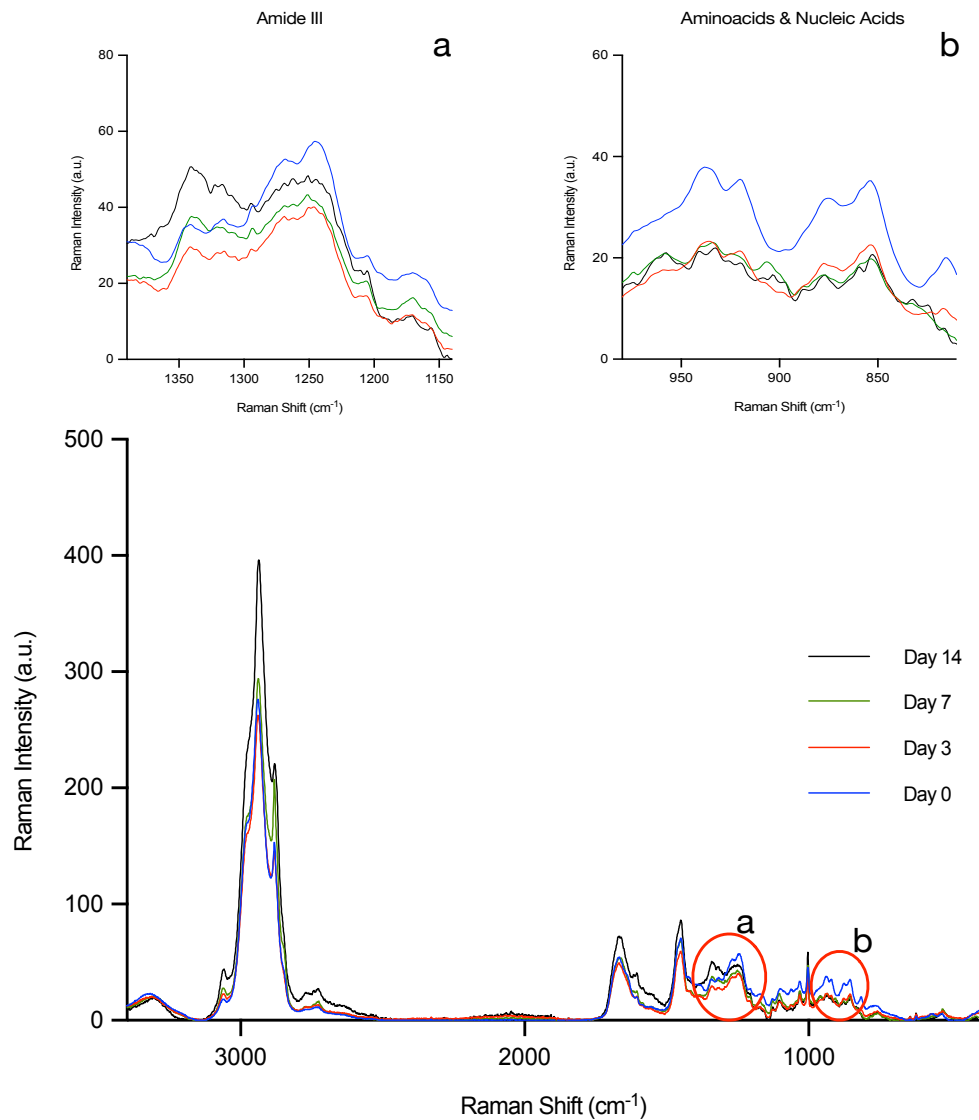
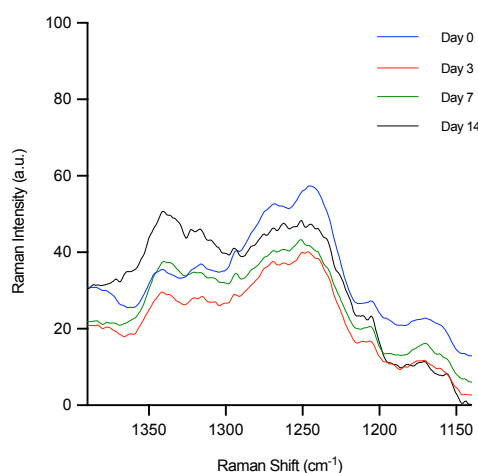


Figure 30. Raman characterisation of contraction in the papillary layer at different time points. Each time point is represented by their spectral profile. Each profile is an average of 60 spectra. In this figure, the most notorious differences between time points have been highlighted and expanded. These regions have been labelled as a) Amide III, and b) Amino acids & Nucleic Acids region.

contraction had expressed gradually throughout the four different time points. Most changes reported are reflected in terms of intensity. **Figure 30** highlights spectral differences that are easy to identify by the naked eye, being Amide III and Amino acids regions the most notorious.

To validate these observations, Raman statistical analysis –via MVA techniques– was performed on all spectral data to accurately spot the most relevant biomarkers. The main spectral differences highlighted by the PCA method were mostly consistent with the visual examination of the Raman qualitative data, which are described below.



Amide III. At day 0, the following peaks appeared within the amide III region: 1341, and 1316 showing a lower intensity than the 1268/1245 cm^{-1} doublet. Although the same peaks appeared after three days into contraction, they all reflected a

reduced intensity when compared to the peaks presented in day 0. Now, according to the statistical analysis of the Amide III region, the PCA showed that at Day 0 of contraction, there was a higher activity from the peptidic bond belonging to the stretching vibration of C-N, 1244 cm^{-1} , and bending vibration of the N-H, 1274 cm^{-1} . Interestingly, by day 3 into contraction samples were



RESULTS & DISCUSSION.

Characterising Contraction in a TEBM Model with Raman Spectroscopy

slightly scattered in the opposite quadrant as a result of a reduction in activity from the peptide bond, 1244 and 1274 cm^{-1} , and instead characterised by a higher activity of the twisting vibration of CH_3 and CH_2 of collagen protein, 1336 cm^{-1} **Figure 31A**. It is expected to assume that since composites had notoriously contracted by day 3, then collagen fibres have been crosslinking between one another. By then, LOX had already converted the ϵ -amine from lysine residues into a highly reactive aldehyde. This will promote the interlocking between polypeptide chains that will eventually surround the peptide bond hindering the vibration of stretching C-N and bending N-H at the collagen backbone.

Additionally to this, these lysine-derived aldehydes at the end of the side chains could be reacting with the N-H of the peptide bond from other polypeptide chains, resulting in the formation of a secondary amide bond. This reaction could also explain the reduction of the N-H bending vibration by day 3 into contraction. Furthermore, CH_3 and CH_2 are mostly located at the side chains of the collagen backbone. When crosslinking is occurring, it is due mostly to these side chains being linked to the side chains of other molecules. Crosslinking between lysine-derived aldehydes and remaining lysine residues will occur spontaneously as collagen fibres keep gliding over one another. This could be due to keratinocytes exerting contractile forces over the dermis during re-epithelialisation. The aforementioned observation has been notorious from day 0 to 3 **Figure 31** and slightly noticed from day 3 to 7 **Figure 32**.



RESULTS & DISCUSSION.

Characterising Contraction in a TEBM Model with Raman Spectroscopy

According to the PCA in **Figure 32B**, the separation between day 3 and day 7 is mostly caused by PC-2, represented by the indirect correlation between 1244 and 1336 cm^{-1} . Correspondingly, this can also be seen in **Figure 32C**, where there is a significant difference between both peaks at day 3 ($p < 0.0001$), whereas by day 7, peak 1336 almost reached intensity values for 1244 cm^{-1} , still remaining significantly different ($p < 0.0003$). At day 7 into contraction the stretching vibration of C-N from the peptide bond (1244 cm^{-1}) keeps reducing in intensity over the course of time, whereas the twisting vibration of the CH_2 and CH_3 bonds (1336 cm^{-1}) keeps increasing. This could indicate that these bonds will be actively vibrating after the transformation of lysine residues into highly reactive aldehydes. However, the activity of the N-H bending vibration from the peptide bond has reached a plateau from day 3 to day 7.

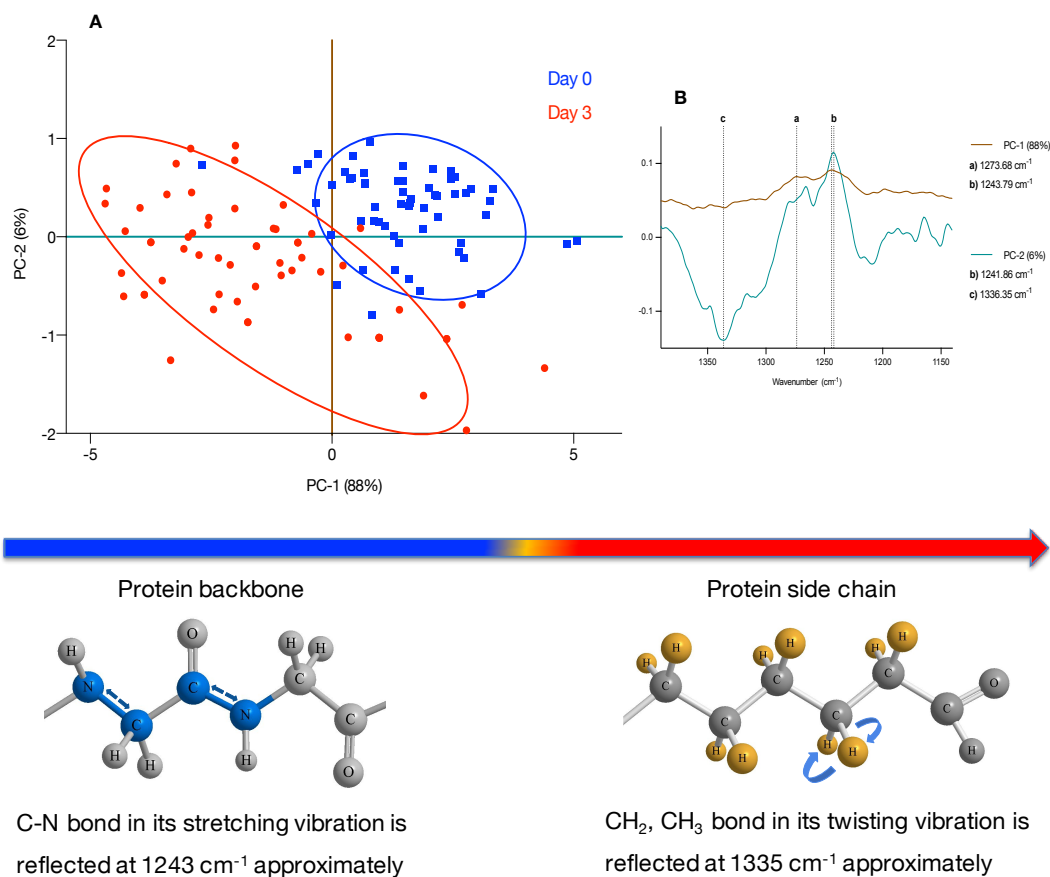


Figure 31. A) PCA score plot of the amide III region: According to the PCA analysis, spectral data from day 0 and day 3 are mostly separated by peaks at 1274 and 1244 cm⁻¹. B) PCA loadings of the amide III region: PC-1 accounting for 88% of the variation, represented by positive values of 1274 and 1244 cm⁻¹ bands. PC-2, represented by a positive and negative value of 1242 and 1336 cm⁻¹, respectively. These two peaks are considered the second component with the next highest variation of 6%, showing an indirect correlation between peaks. C) Illustrates the vibration of chemical bonds characteristic of each time point. At day 0, the stretching of C-N is predominant, whereas day 3 is characterised instead by the twisting of CH₂, CH₃ bonds.

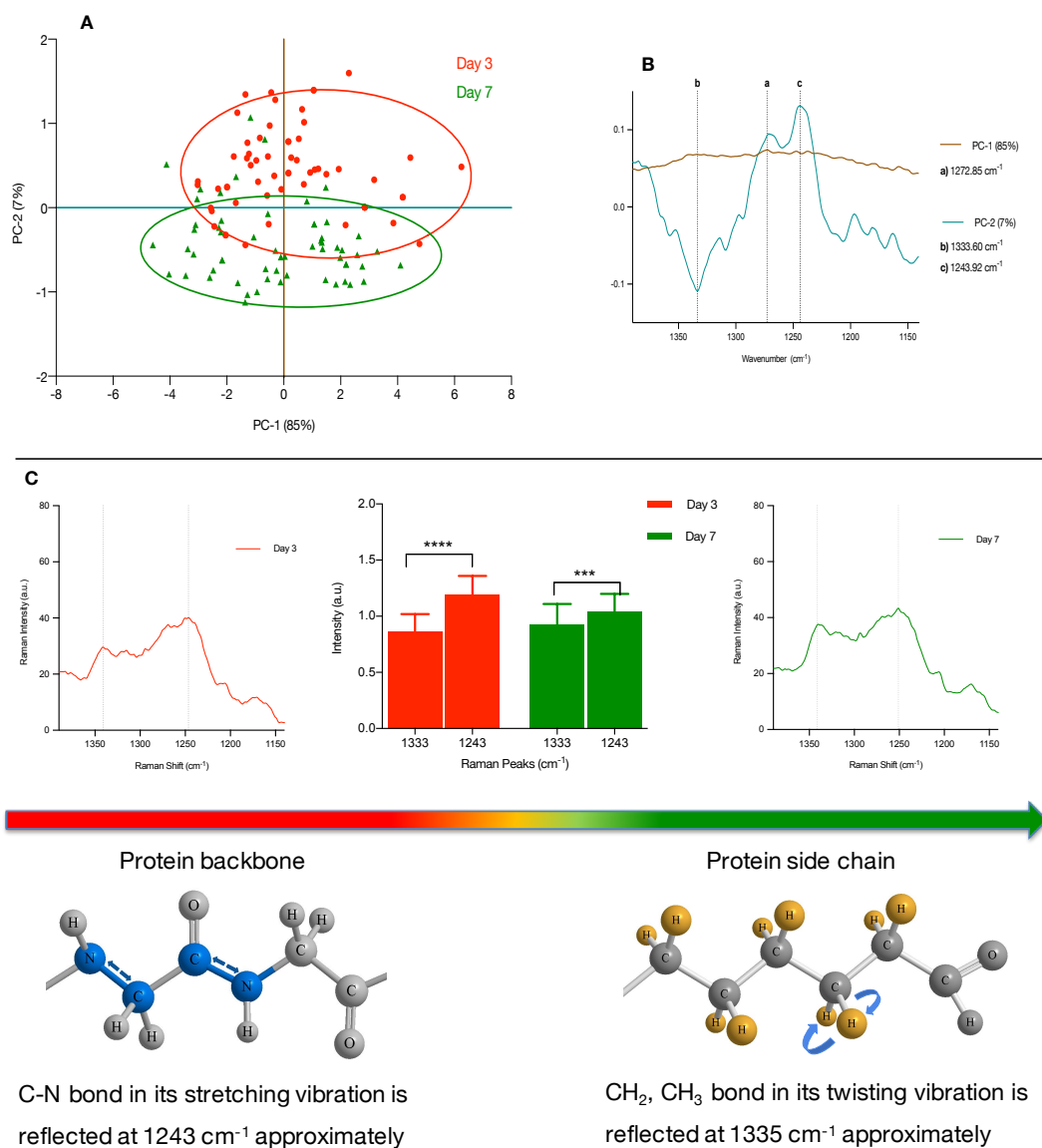
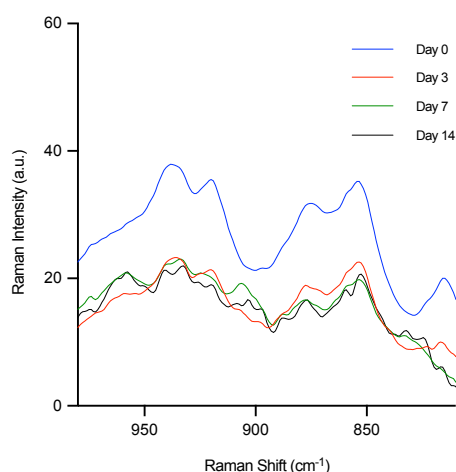


Figure 32. A) PCA score plot of the amide III region: According to the PCA analysis, spectral data from day 3 and day 7 are mostly separated by peaks at 1334 and 1244 cm^{-1} . B) PC-1 accounting for 85% of the variation, represented by positive value of 1273 cm^{-1} band. PC-2, represented by a negative and positive value of 1334 and 1244, respectively, with the next highest variation of 7%, showing an indirect correlation. C) T-test analysis of the indirect correlation between 1243 and 1333 cm^{-1} bands. Mean and SD values were reported as [mean, SD]. For peak at 1243, values were [1.1931, 0.1659] for day

3 and [1.0431, 0.1559] for day 7. For peak at 1335, values were [0.8631, 0.1558] for day 3 and [.9295, 0.1799] for day 7.



Amino and Nucleic Acids. In the amino acids region, the following peaks appeared during the starting point of contraction: 938, 920, 875, 854, and 815 cm^{-1} . By day 3, no significant shift in frequency was perceived, however, same peaks

continue to appear at a lower intensity than in day 0. From day 3 to day 7 into contraction, a few differences were noticed. According to the PCA in **Figure 33A**, at day 3 there is a higher activity of the stretching vibration of C-C bond from both, the hydroxyproline and proline ring, reflected at 854 cm^{-1} and 869 cm^{-1} band respectively. However, by day 7, the activity of these vibrations was no longer as high as in day 3. Instead, day 7 was characterised by a higher activity of the stretching vibration of the C-C from the skeletal backbone of the collagen protein, 905 cm^{-1} , and a significantly lower activity of both bands at 854 ($p < 0.0001$) and 869 cm^{-1} ($p < 0.0001$). These changes in activity may be suggesting that upon cross-linking, the side chains of collagen fibres may be rearranging or compressing as a result of continuous interlocking between polypeptide chains. This reflects in less exposed side chains and higher activity

needed from the collagen backbone. Explaining the decrease of proline and hydroxyproline activity and increase of C-C backbone vibrations by day 7.

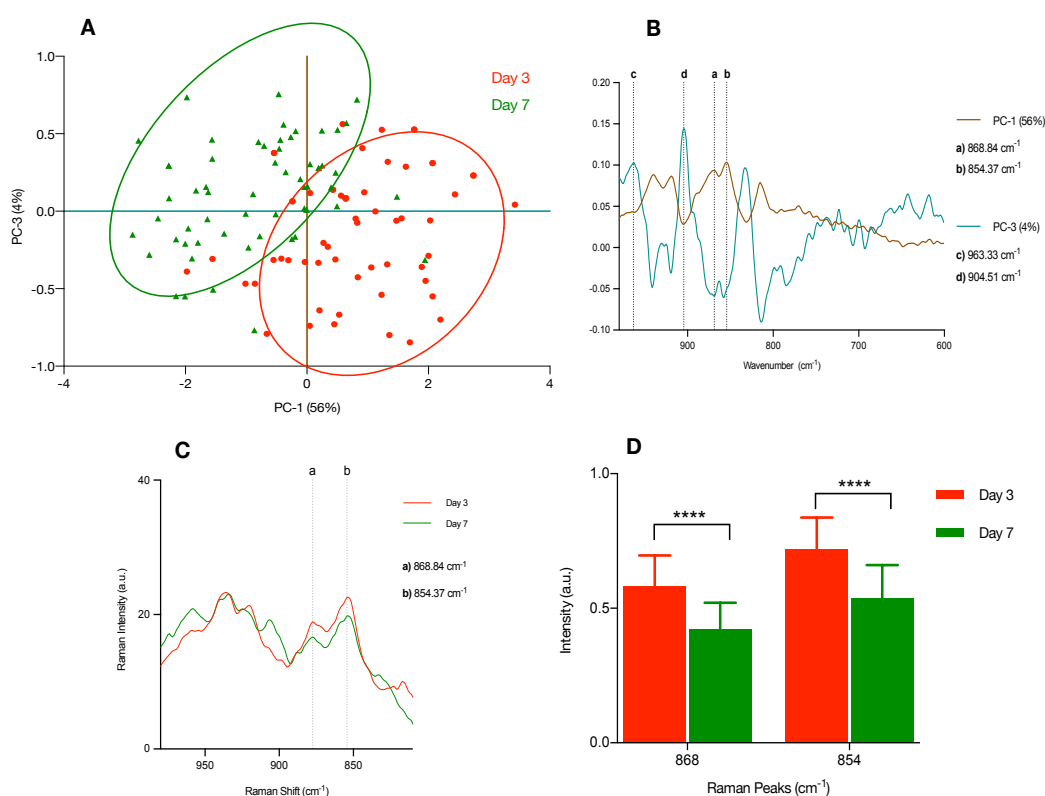


Figure 33. A) Amino acids Region: PCA analysis, spectral data from day 3 and day 7 are mostly separated by peaks at 869 and 854 cm^{-1} . B) PC-1 accounting for 56% of the variation, with positive values of 869 and 854 cm^{-1} bands showing a direct correlation. PC-2: positive values of 963 and 905 cm^{-1} , with a variation of 4%. C) Spectral profile for day 3 in red and day 7 in green. D) T-test analysis of the direct correlation between 869 and 854 cm^{-1} bands at day 3 and day 7. Mean and SD values were reported, for peak at 869, values were [0.5826, 0.1139] for day 3 and [0.4232, 0.0975] for day 7. For peak at 854, values were [0.7181, 0.1192] for day 3 and [0.5387, 0.1217] for day 7.

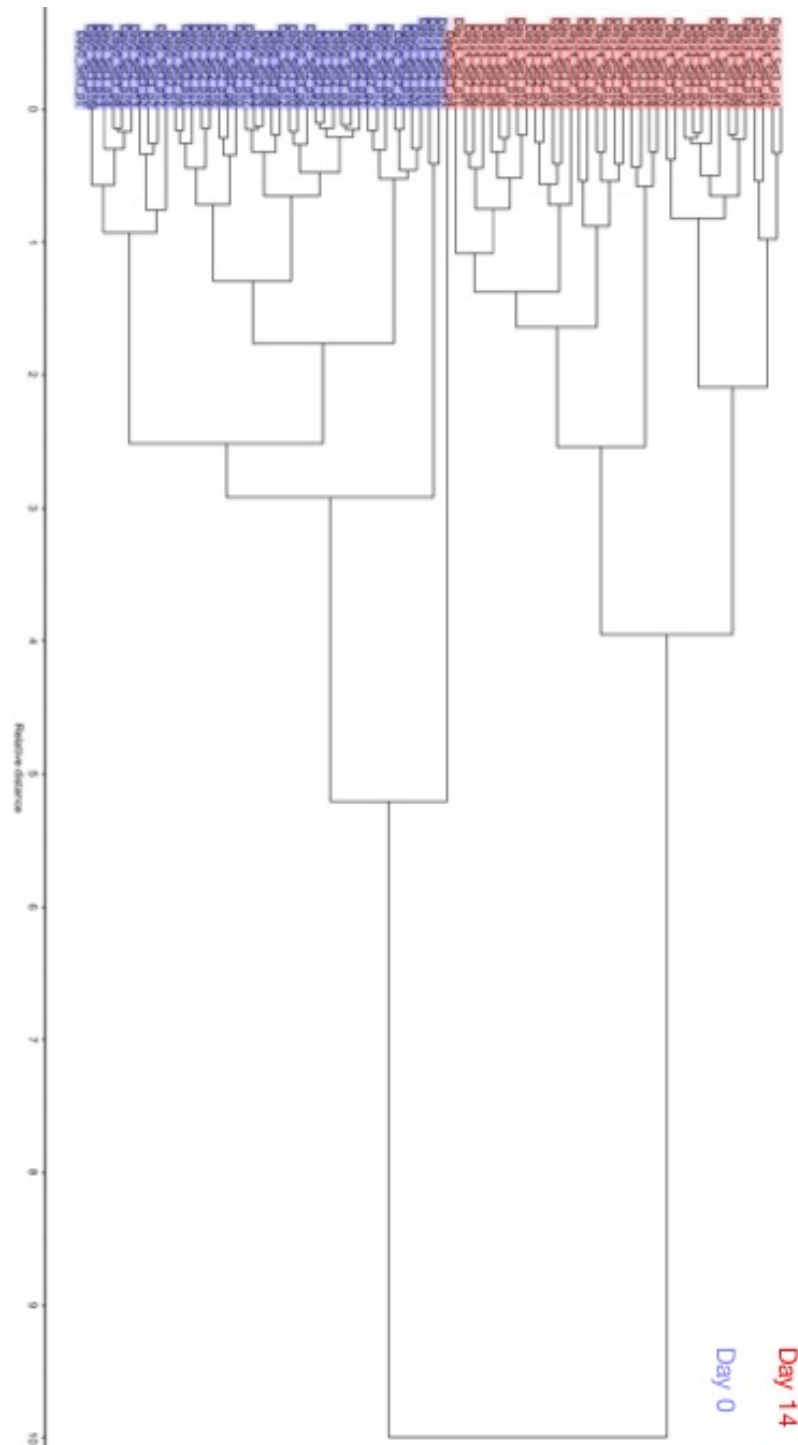


Figure 34. CA of Amide III region on Day 0 and Day 14 of contraction in a TEBM model. The unsupervised method clustered Day 0 and separate it from Day 14.



RESULTS & DISCUSSION.

Characterising Contraction in a TEBM Model with Raman Spectroscopy

6.3.3 RETICULAR LAYER

The analysis and interpretation of Raman data on the contraction occurring in the reticular layer of oral mucosa models are explained in this section. While it may be true that the highest activity of contraction was seen from day 0 to day 3, biochemical changes occurring over the course of three days did not manifest abruptly on the spectra of day 3 for the reticular layer. Instead, qualitative Raman data showed that most biochemical changes occurring during contraction had expressed notoriously mainly between day 3 and 7. Most changes reported are reflected in terms of intensity. **Figure 35** highlights spectral differences that are easy to identify, being Amide I, II and III the most notorious regions.

To validate these observations, Raman statistical analysis –via MVA techniques– was performed on all spectral data to accurately spot the most relevant biomarkers. The main spectral differences highlighted by the PCA method were mostly consistent with the visual examination of the Raman qualitative data, which are described below.

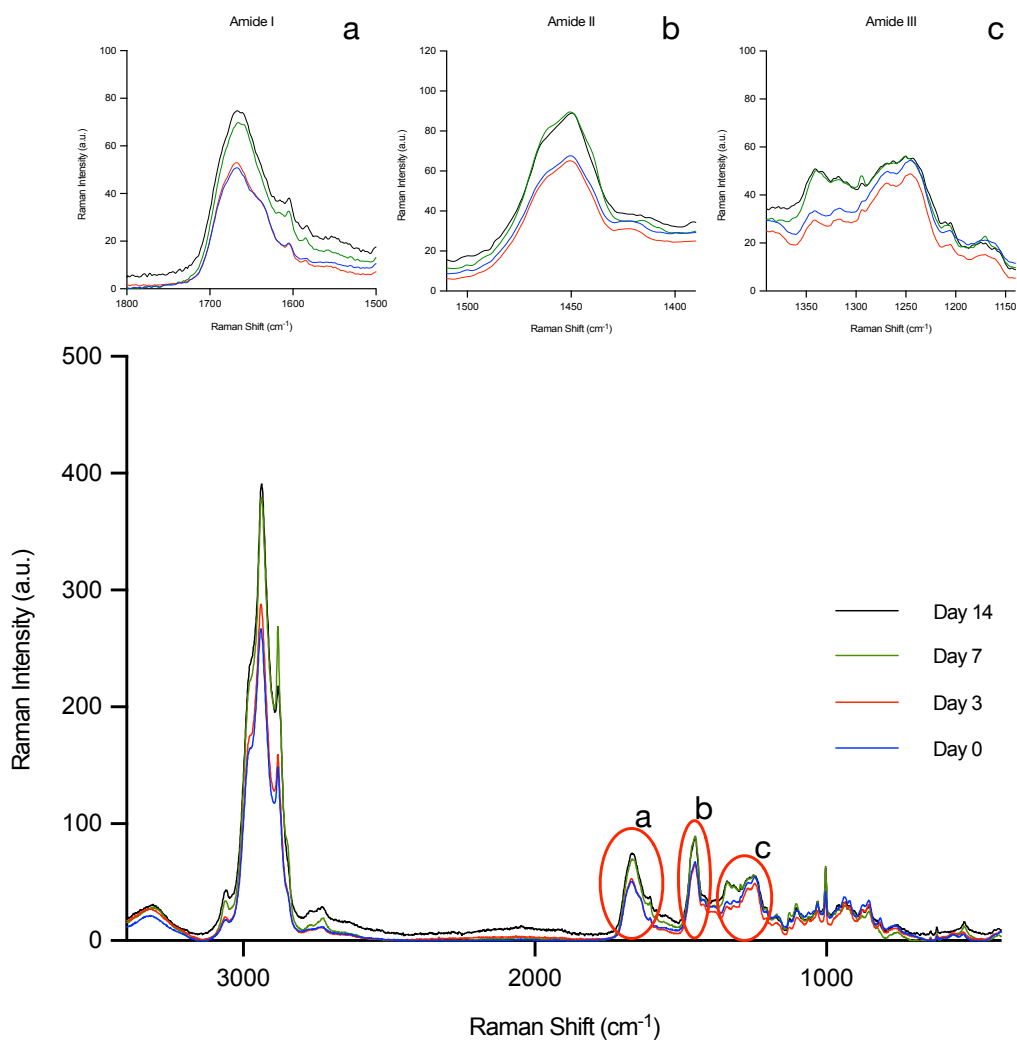
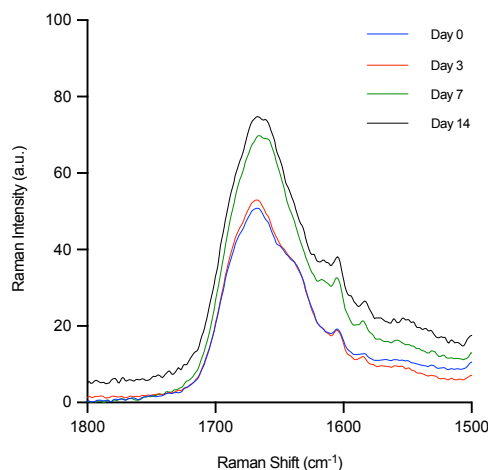


Figure 35. Raman characterisation of contraction in the reticular layer at different time points. Each time point is represented by their spectral profile. Each profile is an average of 60 spectra. In this figure, the most notorious differences between time points have been highlighted and expanded. These regions have been labelled as followed, a) Amide I, b) Amide II, and c) Amide III region.



Amide I. At the starting point of contraction, the reticular layer reflected an amide I band at 1667 together with a peak at 1605. By day 3 of contraction, there was a lower amount of activity from the stretching vibration of the C=O bond from the α -helix conformation of

collagen, 1657 cm^{-1} . Together with this there was also a low activity in the stretching vibration of the C-C bond from phenylalanine and tyrosine residues, 1606 and 1613 cm^{-1} respectively. By day 7 however, the activities of these bands increased considerably and were higher than at day 3. This translates in a higher intensity of bands at 1657 , 1613 and 1606 cm^{-1} . Tyrosine residue encompasses a variety of vibrational modes, which are reflected throughout the whole spectral range. For instance, the stretching mode of C-C from tyrosine reflects at 1613 cm^{-1} ,¹³¹ whereas the bending mode of C-C appears at 1606 cm^{-1} .^{23,70} As contraction increases, so does the activity of these bands reflecting a higher amount of tyrosine. Coupled with this, by day 7 most of the samples have shown a stronger tendency towards 1655 cm^{-1} indicative of C=O stretching vibration in an α -helix polypeptide chain. Based on the PCA analysis of Amide I region, the separation between both time points is mostly caused by the PC-4 loadings. As can be seen **Figure 36B** the PC-4 is accounting for 3% of the variation but it is significant enough to provoke a separation.

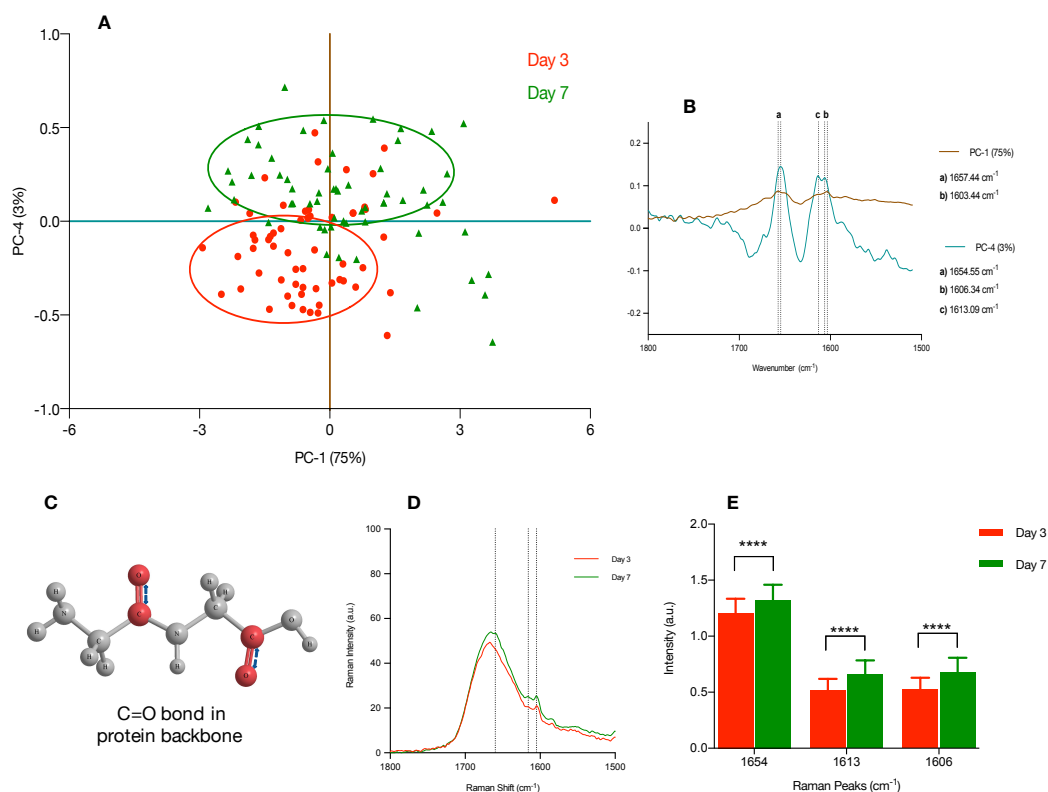
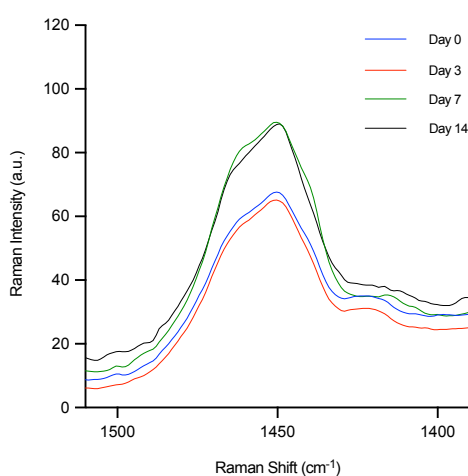


Figure 36. **A)** PCA score plot of the amide I region: According to the PCA analysis, spectral data from day 3 and day 7 are mainly separated by peaks at 1655, 1613, and 1606 cm^{-1} . **B)** PCA loadings of the amide I region: PC-1 accounting for 75% of the variation, represented by positive values of 1657 and 1603 cm^{-1} bands. PC-4, represented by positive values of 1655, 1613, and 1606 cm^{-1} . These three peaks are accounting for 3% of the variation showing a direct correlation. **C)** Schematic representation of the C=O group. **D)** The amide I region is expanded, spectral profile for day 3 in red and day 7 in green, with both peaks indicated by dotted line. **E)** T-test analysis of the direct correlation between all three bands from PC-4 at day 3 and day 7. Mean and SD values were reported as [mean, SD]. For peak at 1655, values were [1.2076, 0.1271] for day 3 and [1.3224, 0.1370] for day 7. For peak at 1613, values were [0.5153, 0.1030] for day 3 and [.6603, 0.1239] for day 7. For peak at 1606, values were [0.5226, 0.1065] for day 3 and [0.6780, 0.1300] for day 7.

All three peaks have positive values, and since they are all under the same loading a positive correlation between all them is established. Correspondingly, in **Figure 36E** a t-test analysis of the intensities of all peaks between time points is shown. It can be seen how the difference between time points in all three peaks is considered significant, 1654 ($p < 0.0001$), 1613 ($p < 0.0001$) and 1606 cm^{-1} ($p < 0.0001$), indicating that as contraction increases, so does the intensity values of tyrosine (1606.34, 1613.09 cm^{-1}) and the α -helix structure (1654.55 cm^{-1}).



Amide II. According to the PCA of the Amide II region, a clear separation between time points 3 and 7 was obtained mainly because of PC-2 and represented by band at 1422 cm^{-1} . Based on the loading shown in **Figure 37**, the 1446 cm^{-1}

band is responsible for PC-1. According to the PCA score plot, the bending mode of CH_2 from proteins is equally active at both time points. Even after conversion of lysine residues into aldehydes, sporadic crosslinking to other lysine or available aldehydes will keep occurring. As a result, the non-enzymatic spontaneous crosslinking between aldehydes of different side chains will require the bending of the CH_2 bonds. Reflecting similarly at both time points since contraction of the models keeps occurring. Additionally, at day 3 samples

reflected a higher activity of N-H in plane deformation than at day 7, which was manifested by a higher intensity of 1422 cm^{-1} band. However, since spontaneous crosslinking is still occurring by day 7, formation of secondary amides interrupts the vibration of this bond. This observation could be reflected as a reduction of the bending vibration of N-H from the peptide bond.

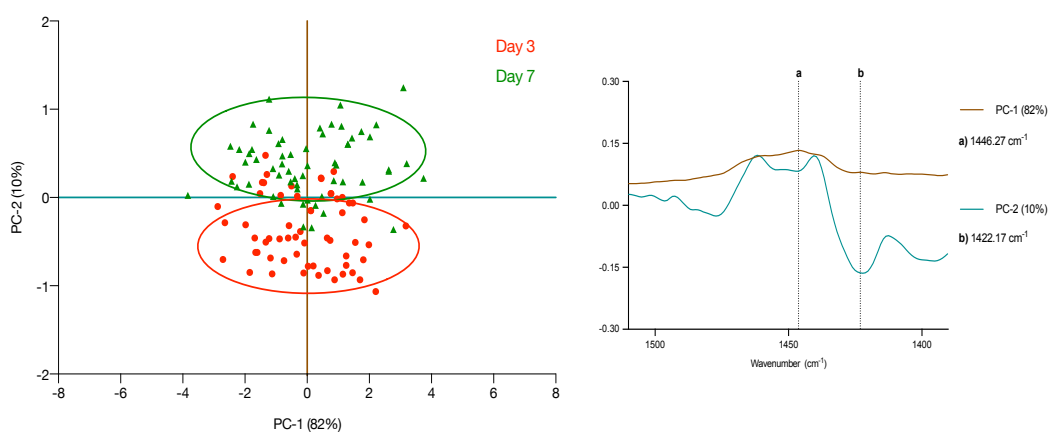
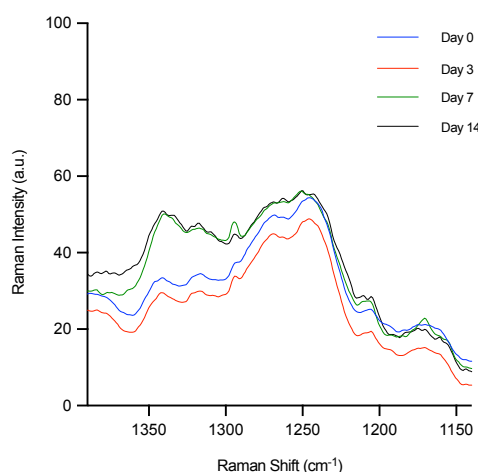


Figure 37. PCA score plot of the amide II region: According to the PCA analysis, spectral data from day 3 and day 7 are mostly separated by PC-1 and PC-2. PCA loadings of the amide II region: PC-1 accounting for 82% of the variation, represented by a positive value of 1446 cm^{-1} band. PC-2, represented by a negative value of 1422 cm^{-1} . This peak is considered the second component with 10% of the variation.



Amide III. At day 0, the following peaks were found in amide III region: 1341 and 1316 with a notoriously low intensity when compared to the 1268/1246 cm^{-1} doublet. After day 3 into contraction not much spectral change was

shown, only a slight decrease in intensity for all peaks previously mentioned. However, by day 7 both peaks at 1340 and 1317 considerably raise in intensity almost reaching the intensity values of the 1271/1251 doublet. According to the PCA done between day 3 and day 7, separation of both groups is caused mainly by PC-2, which according to the loadings it is represented by two peaks that are indirectly correlated, 1243 and 1335 cm^{-1} . At day 3 of contraction, a higher activity of the stretching vibration of the C-N from the peptide bond was exhibited, 1243 cm^{-1} . By day 7, this vibration slowed down in activity whereas the twisting vibration of CH_3 and CH_2 increased notoriously, 1335 cm^{-1} . This observation confirms what was noticed in the epithelium and papillary layer, where the stretching vibration of C-N reduces in activity as crosslinking increases. As previously mentioned, this could be due to the limited flexibility remained after formation of secondary amines through the N-H from the peptide bond. Also, since polypeptide chains keep crosslinking between one another, rearrangement of collagen fibres kept occurring. Hence, it may be possible that

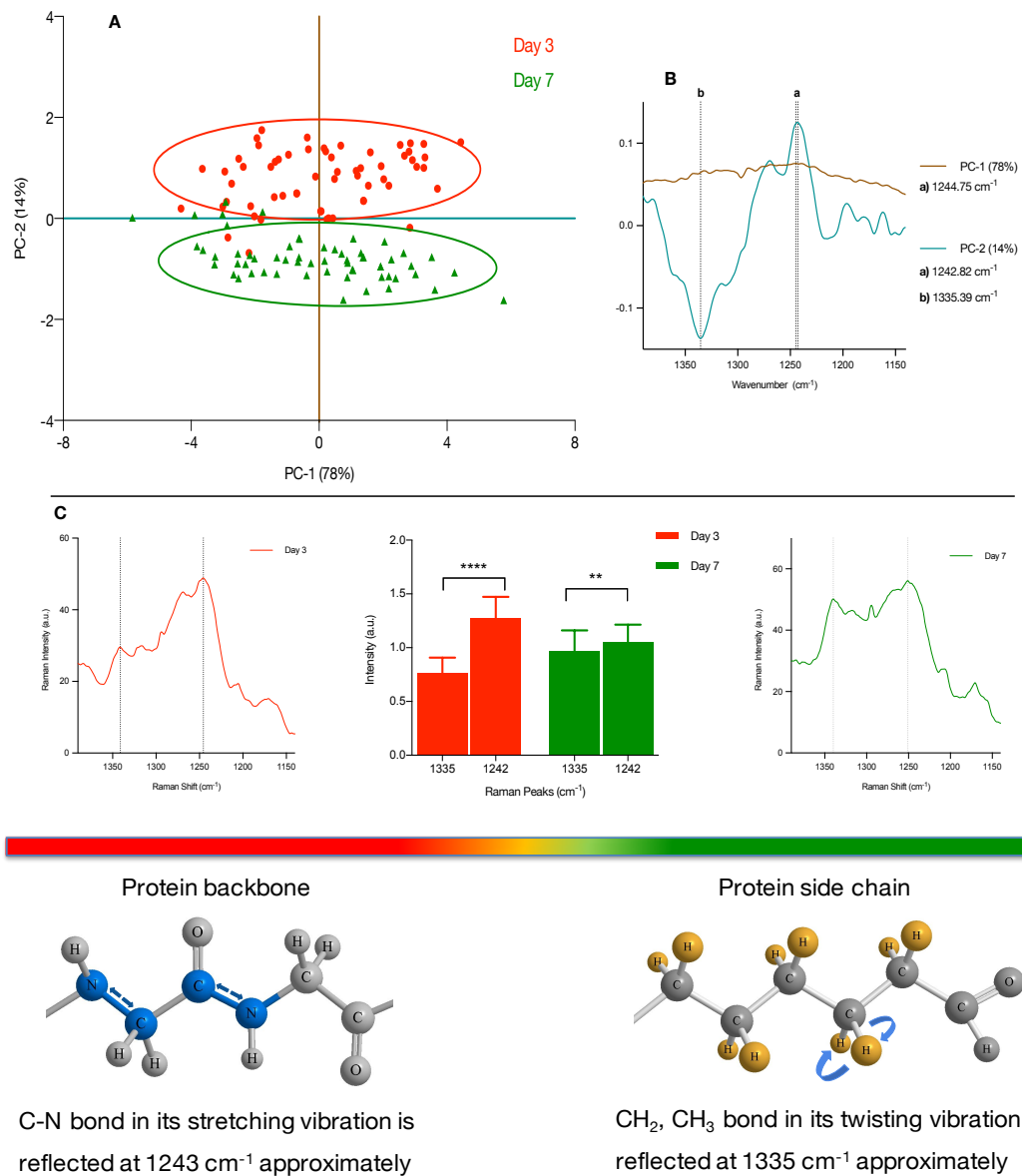


Figure 38. **A)** PCA score plot of the amide III region: According to the PCA analysis, spectral data from day 3 and day 7 are mostly separated by peaks at 1335 and 1243 cm^{-1} . **B)** PCA loadings of the amide III region: PC-1 accounting for 78% of the variation, represented by positive value of 1245 cm^{-1} band. PC-2, represented by a negative and positive value of 1335 and 1243 cm^{-1} , respectively. These two peaks are considered the second component with the next highest variation of 14%, showing an indirect correlation. **C)** T-test



RESULTS & DISCUSSION.

Characterising Contraction in a TEBM Model with Raman Spectroscopy

analysis of the indirect correlation between 1243 and 1335 cm^{-1} bands. At day 3 of contraction, intensity values are significantly different between the indirectly correlated bands ($p < 0.0001$). By day 7, still there is a significant difference ($p < 0.0072$), however the band at 1335 almost reached the 1243 cm^{-1} intensity values. Mean and SD values were reported as [mean, SD]. For peak at 1243, values were [1.2723, 0.1997] for day 3 and [1.0552, 0.1593] for day 7. For peak at 1335, values were [0.7640, 0.1431] for day 3 and [.9668, 0.1932] for day 7.

the increase in twisting vibration from the CH_3 and CH_2 could be a result of the existing side chains compressing by the accommodation of fibres. In addition to this, by day 7 onwards, an upshift in frequency was detected from 1246 at day 3 to 1251 cm^{-1} at day 7.

6.4 SUMMARY

Raman spectroscopy was successful in identifying the biochemical effects of contraction on TEBM models. The ability of this technique to monitor the process of contraction is proven by a number of biomarkers identified in this chapter. While it may be true that the role of LOX in contraction is well-explained in the literature, RS is providing information regarding the regional effects of contraction that contributes in understanding the focal points of progression.

1. For instance, it is described in this chapter the crucial role of the peptidic bond of collagen polypeptide chains (reflected in the Amide III region) as a biomarker



RESULTS & DISCUSSION.

Characterising Contraction in a TEBM Model with Raman Spectroscopy

of crosslinking of collagen. As contraction increases as a function of time, so does the intensity band at 1336 cm^{-1} , while the intensity of 1244 cm^{-1} decreases. This turnover of intensities became more drastically noticed during the highest activity of contraction.

2. Moreover, RS also confirmed that biochemical changes of contraction are first manifested by the epithelium layer and as time goes by then it significantly appears in the papillary and reticular layer. The notorious spectral changes that each layer displayed at subsequent time points is an indication that contraction is moving in what it would be called a cascade effect.



RESULTS & DISCUSSION.

Characterising Contraction in a TEBM/ β -APN Model With Raman Spectroscopy

7 CONTRACTION IN A TEBM MODEL WITH β -APN

A substantial amount of research has been carried out to study the mechanism of contraction in tissue-engineered skin^{113,159-160} and oral mucosa models.^{119,120} It has been well-established a direct correlation between an overexpression of lysyl oxidase (LOX) enzyme and the degree of contraction seen in these engineered models.^{161,162} Because of this, inhibition of LOX enzyme became the appropriate target in order to reduce the mechanism of contraction. Although studies then reported on a variety of pharmacologic approaches that prevented this phenomenon, most of them lead to unwanted secondary effects that render them counterproductive.¹¹³ The effect of β -APN on engineered models has been studied since and it has been well-documented that this drug is capable of preventing contraction to some extent by inhibiting the activity of LOX enzyme.^{113,162-163} Although considerable research has been committed to pharmacologic modulation of oral mucosa contraction, less attention has been paid to the need for a better understanding behind the mechanism of drug-3D composites' interaction. For that reason, this chapter reports on the results obtained from characterising the inhibition of contraction in β -APN-containing TEBM models, with Raman spectroscopy.

7.1 RESULTS & DISCUSSION



RESULTS & DISCUSSION.

Characterising Contraction in a TEBM/ β -APN Model With Raman Spectroscopy

7.1.1 DIMENSIONAL ANALYSIS

To quantify the degree of contraction occurring in β -APN-containing TEBM models, surface area of all samples was measured at different time points over a period of 14 days. Consistent with the previous experiment, the marking time points were day 0, 3, 7 and 14 at an ALI. All samples were photographed once a time point was reached and samples representing the time point in question were then removed from the six-well plate and fixed to be further processed and analysed. From the images obtained, the remaining surface area was then measured using Image JTM software, **Figure 39**.

The extent of contraction was calculated at each time point and in **Figure 40** a representation of the remaining surface area as a function of time can be seen. The average and SD values for each time point was calculated and listed below in **Table 12**. After three days at the ALI, the 3D composites only reduced to ~10% of their surface area. In this case, the highest activity of contraction appeared to be between day 3 and day 7, where a reduction of ~23% of the surface area can be observed while from day 7 to day 14 only ~10% was lost. According to the data, the introduction of β -APN in the TEBM models seem to be reducing the progression of contraction.

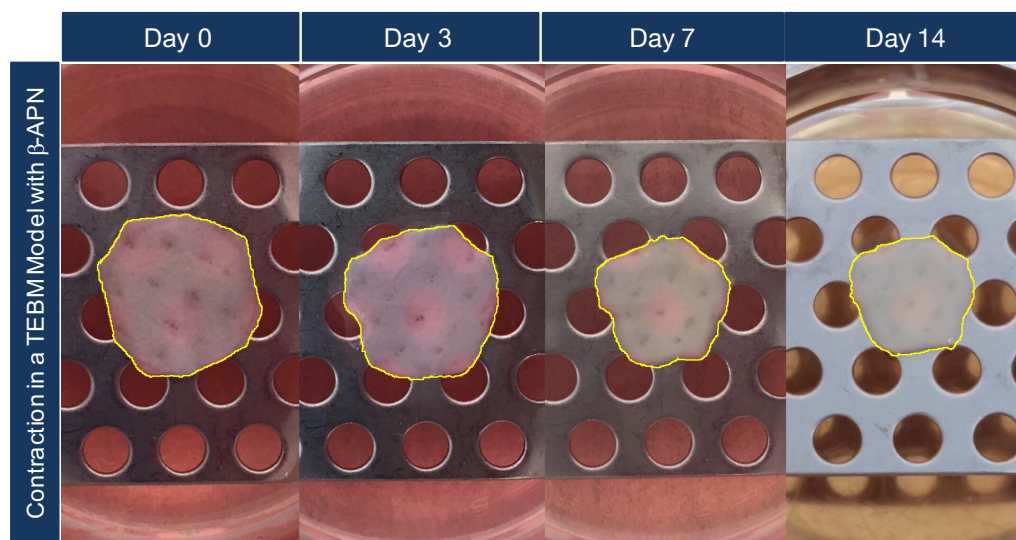


Figure 39: β -APN-containing TEBM model. Sample #4 showing the extent of contraction at day 0, 3, 7 and 14. This sample was assigned as day 14 and photographed at each time point. Once day 14 was reached, sample was removed from the 6-well plate and fixed to be further analysed.

Table 12. Average and SD values for the remaining surface area calculated at each time point in a β -APN-containing TEBM model.

% of Remaining Surface Area in TEBM Models (triplicates)			
Time points (days)	Average (cm ²)	SD	%
0	0.894 (n=12)	0.21	100
3	0.804 (n=9)	0.14	90
7	0.596 (n=6)	0.06	67
14	0.509 (n=3)	0.05	57

This can be related to Arnold et al. who reported that long-lasting effects of β -APN is due to administration of periodic doses.¹⁶⁴ Since in this experiment medium was replaced every 2-3 days with β -APN-containing medium (200 μ g/mL β -APN) contraction in TEBM models was periodically modulated

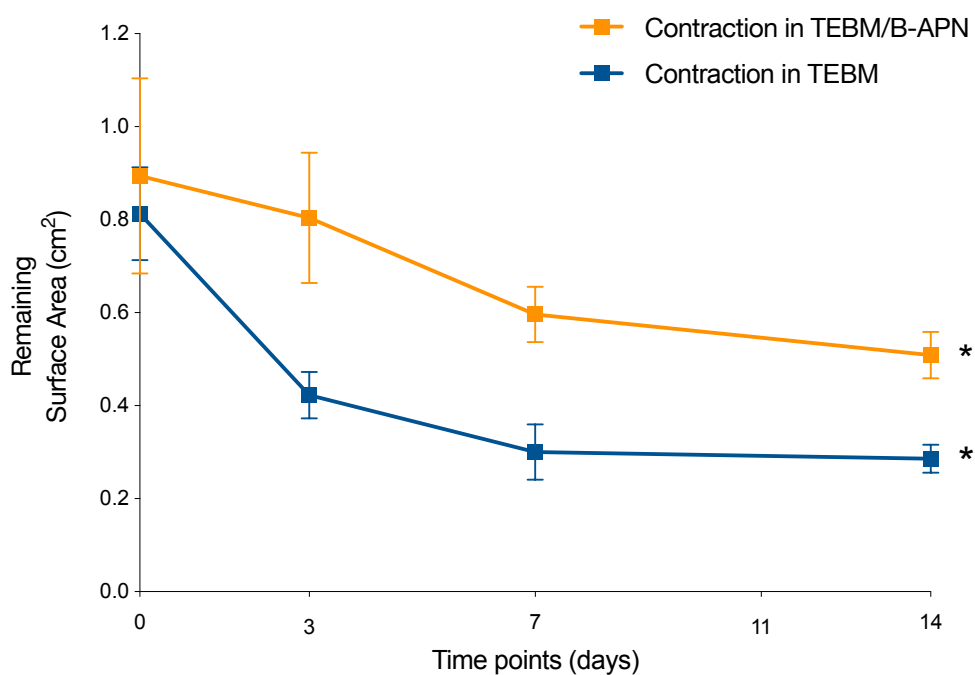


Figure 40. Remaining surface area as a function of time in β -APN-containing TEBM models. Solid orange line is representing the average calculated for each timepoint. Dashed orange lines are indicating SD values. (One-way t test was performed: $p < 0.0214$, *, for control model (blue). $P < 0.0441$, *, for drug model (orange))

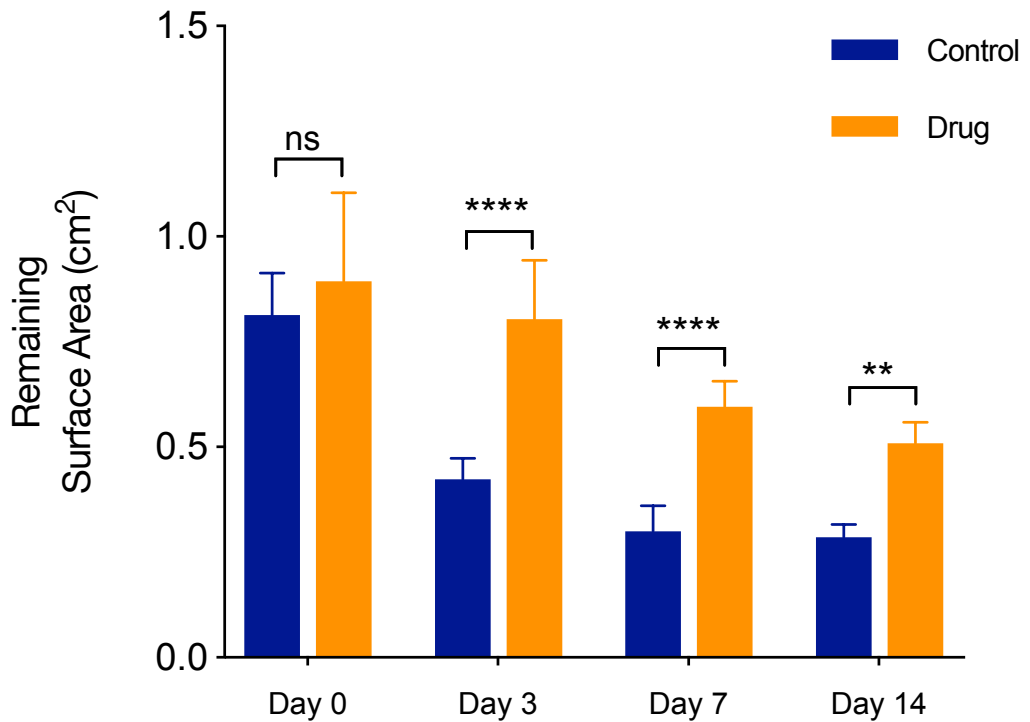


Figure 41. Unpaired t-test statistical analysis of surface area of control vs drug model as a function of time. Day 0 (p value .2385, ns). Day 3 (p<0.0001, ****). Day 7 (p<0.0001,****). Day 14 (p<0.0023, **).

7.1.2 HISTOLOGICAL ANALYSIS

In **Figure 42** it can be seen the histological representation of β -APN-containing TEBM models at different time points during contraction. While at day 0 and day 3 a decent stratification of the epithelium was appreciated, this was not the case for day 7 and day 14, where a lack of vertical migration from the keratinocytes resulted in a poorly stratified epithelium. According to the

literature, introduction of β -APN into 3D composites hinders the differentiation of keratinocytes and fibroblast resulting in a direct effect on the stratification of the epithelium.¹⁶⁵

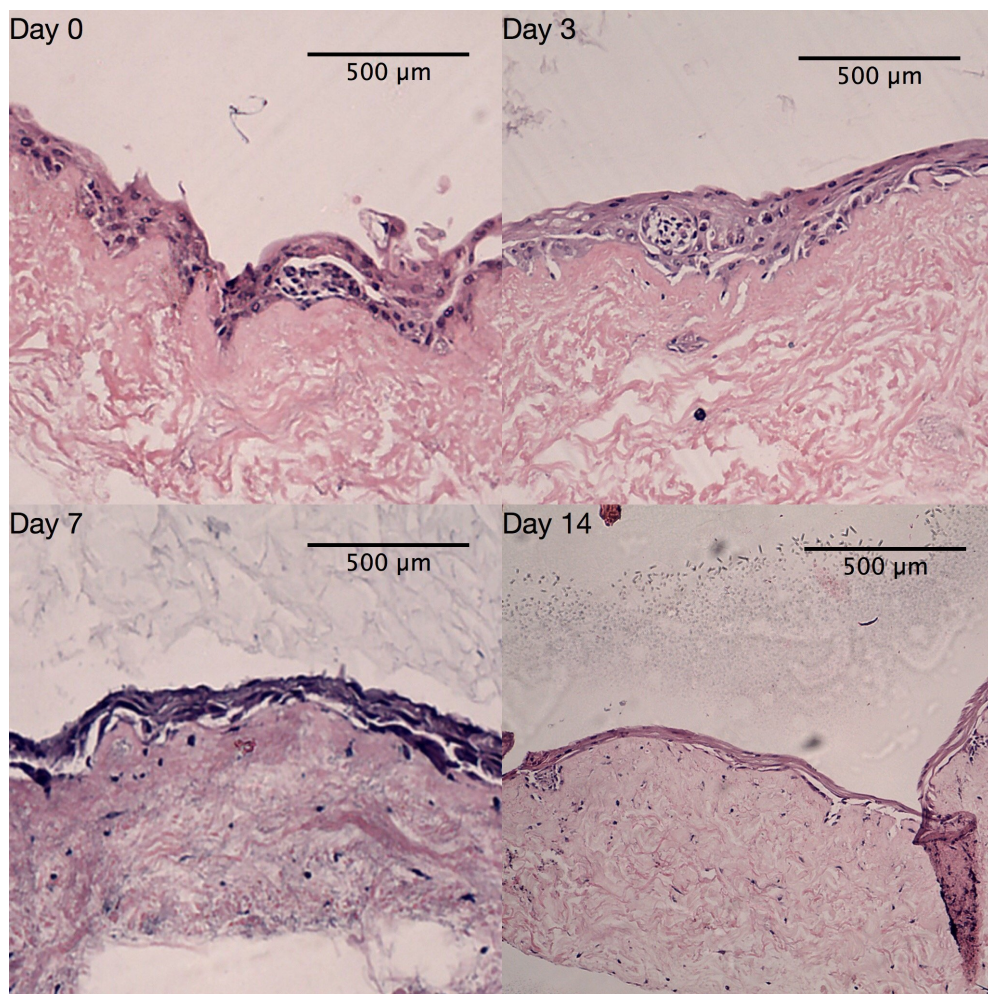


Figure 42. Histological images of β -APN-containing TEBM models at different time points.

7.1.3 RAMAN SPECTROSCOPY CHARACTERISATION



RESULTS & DISCUSSION.

Characterising Contraction in a TEBM/ β -APN Model With Raman Spectroscopy

To keep consistency between experiments, same procedure described in section 5.4 was followed when analysing TEBM/ β -APN with Raman Spectroscopy. Subsequently, data collected for both TEBM and TEBM/ β -APN was then compared in order to establish the main differences and effects caused after the incorporation of β -APN drug. The epithelium, papillary and reticular layer were the three main layers that were studied. The purpose of this was to establish and compare the spectral profiles and detecting the differences occurring between each day of contraction.

7.1.3.1 EPITHELIUM LAYER

After incorporation of β -APN drug into the TEBM models, significant differences were noted in a delayed manner, especially when compared to the control data. Illustrated In **Figure 43** the spectral profile of TEBM/ β -APN models at different time points of contraction. As can be seen, spectral differences are not as noticeable as in the control data. Some of the spectral differences are noticed until day 7, which as it has been previously mentioned, day 7 was the highest activity of contraction in this group. It has been highlighted and expanded the regions that are more relevant and had higher spectral differences between time points in this layer. In this case and after analysis with MVA techniques, it became apparent that lipids molecules had a bigger role in the epithelial layer of TEBM/ β -APN models.

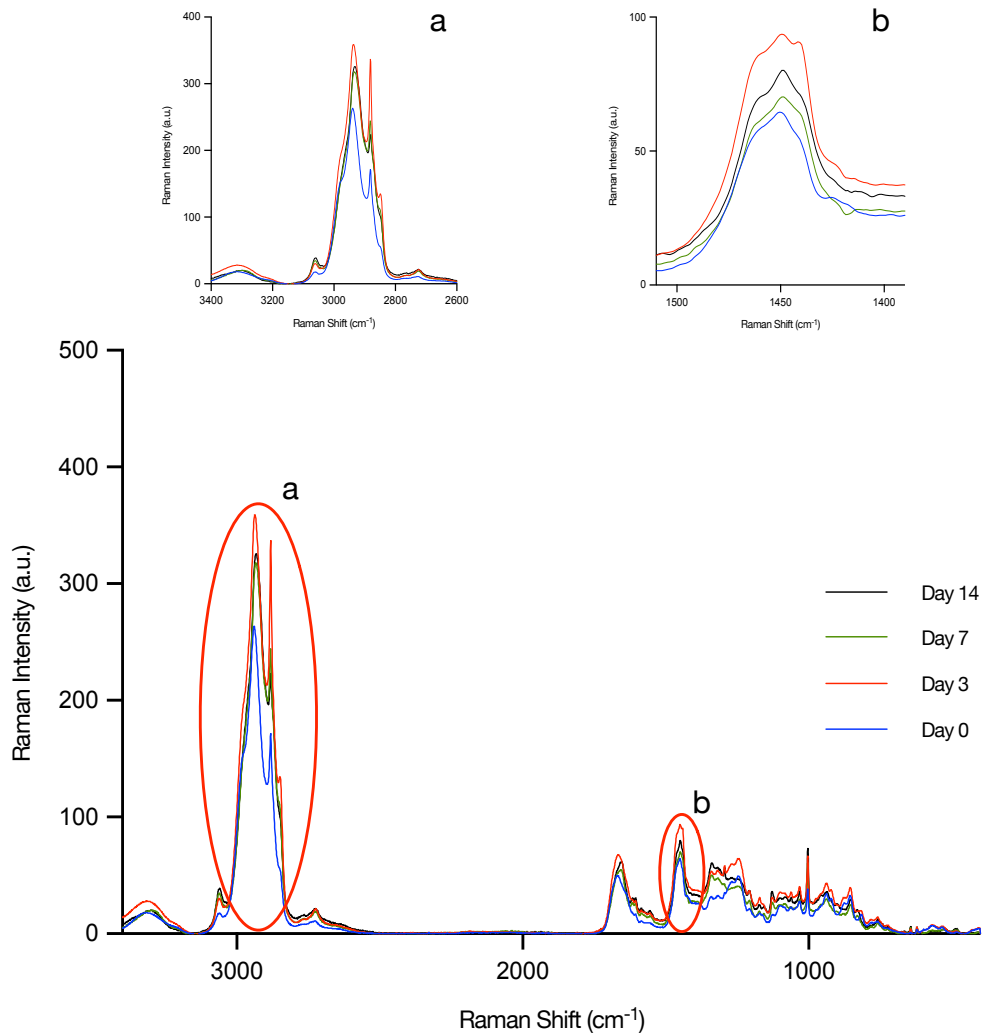


Figure 43. Raman characterisation of contraction in a TEBM/ β -APN models in the epithelium layer at different time points. Each time point is represented by their spectral profile. Each profile is an average of 60 spectra. In this figure, the most notorious differences between time points have been highlighted and expanded. These regions have been labelled as followed, a) Lipids and b) Amide II regions.

When analysing the epithelial layer, the main spectral differences identified when comparing both, the TEBM and TEBM/ β -APN groups, were reflected by



RESULTS & DISCUSSION.

Characterising Contraction in a TEBM/ β -APN Model With Raman Spectroscopy

lipids molecules. It has been previously reported that changes in cellular processes due to different types of diseases most often results in an alteration of lipids metabolism.¹⁶⁶ In this instance, we evaluated spectral differences that were reflected after the incorporation of β -APN drug into the TEBM models. Since these differences were coming from lipid molecules, the possibility of lipids metabolism being compromised was explained in this section. Either lipids are being used as structural components of biological membranes of keratinocytes' cells, or most likely, they are being used as the main source of energy storage to further be used for crosslinking of fibres. This theory was proposed since it has been reported that LOX enzyme has been directly correlated with increasing content of lipids in adipocyte tissue.^{167,168} Therefore, this section reports on the changes seen with regards to lipids molecules in the highest activities of contraction for both the TEBM and TEBM/ β -APN data.

The PC analysis performed on the Amide II region ($1510-1390\text{ cm}^{-1}$) highlighted spectral differences responsible for a moderate separation between TEBM and TEBM/ β -APN data. Accountable for this separation is the combination of PC-1 and PC-2 loadings. According to the score plot in **Figure 44A**, at day 3 of contraction, there is a lower content of CH_2 bending vibrations from fatty acids and lipids in the TEBM group that is being represented by the 1440 and 1452 cm^{-1} respectively.^{169,170} This is not the case for the TEBM/ β -APN group. After incorporation of β -APN into the TEBM constructs, it is noticeable that the content of lipids is considerably higher by an up regulation



RESULTS & DISCUSSION.

Characterising Contraction in a TEBM/ β -APN Model With Raman Spectroscopy

of the CH₂ bending vibrations from both fatty acids (1440 cm⁻¹) and lipids (1452 cm⁻¹). This observation is also seen when analysing the lipids region (3100-2680 cm⁻¹) in **Figure 44B**. Again, a higher content of lipids is found in the TEBM/ β -APN data than when compared to the control TEBM group. Overall, there is a higher asymmetric stretching vibration of CH₂ bonds coming from lipids and fatty acids reflected in this case at 2881 cm⁻¹. At day 7 however, this is no longer the case. When analysing the 1510-1390 cm⁻¹ spectral region, lipids content appeared lower in the TEBM/ β -APN group than when compared to the control data. Separation of both groups in **Figure 45** is mainly caused by a decreased in the CH vibrations of lipids reflected at 1449 and 1465 cm⁻¹.

It has been reported that LOX enzyme has found to be directly correlated to the accumulation of lipids content in the adipose tissue during the pathological processes of obesity and cancer progression and metastasis.^{171,172} According to Huang et al., the enzyme plays a role in promoting the commitment of stem cells towards adipocyte lineage.¹⁶⁷ It has also been documented that during the carcinogenesis process, LOX enzyme activity increases and so does disturbances in some aspects of lipid metabolism. This might be suggesting that overexpression of LOX enzyme may result in accumulation of lipid content during the initial stage of contraction. However, not all lipid storage seen in Raman is reflecting the anatomical components of biological membranes. The results highlighted above when comparing TEBM with TEBM/ β -APN data, might be indicating increase of lipid's uptake as the main source of energy



RESULTS & DISCUSSION.

Characterising Contraction in a TEBM/ β -APN Model With Raman Spectroscopy

during the contraction process. While it may be true that different type of tumours have shown glucose intake to be their main source of energy,¹⁷³ others like prostate cancer have proven low intake of glucose and instead high dependence on lipid oxidation for energy purposes.¹⁷² In this case, lower content of lipids seen at day 3 in the TEBM group when compared to the TEBM/ β -APN data could be indicating higher rate of lipid utilization during the highest activity of contraction. According to **Figure 44C**, surface area of TEBM models contracted ~48% in average, whereas in the TEBM/ β -APN models only a reduction of ~10% was seen at day 3. This could be suggesting that content of lipids is first being accumulated during early stages of LOX activity, and then it is reduced during highest activity of contraction as it is being used as the main source of energy. Interestingly, at day 7 of contraction, the lowest content of lipids is now seen in the β -APN model. The highest activity of contraction after incorporation of β -APN drug was seen at day 7 with a reduction of ~23% in surface area. In comparison, the control models only reduced ~15% of surface area from day 3 to 7. This goes in agreement with the theory proposed above where higher activity of contraction translates into higher uptake of lipids utilisation as energy source resulting into lower content of lipids in the Raman data.

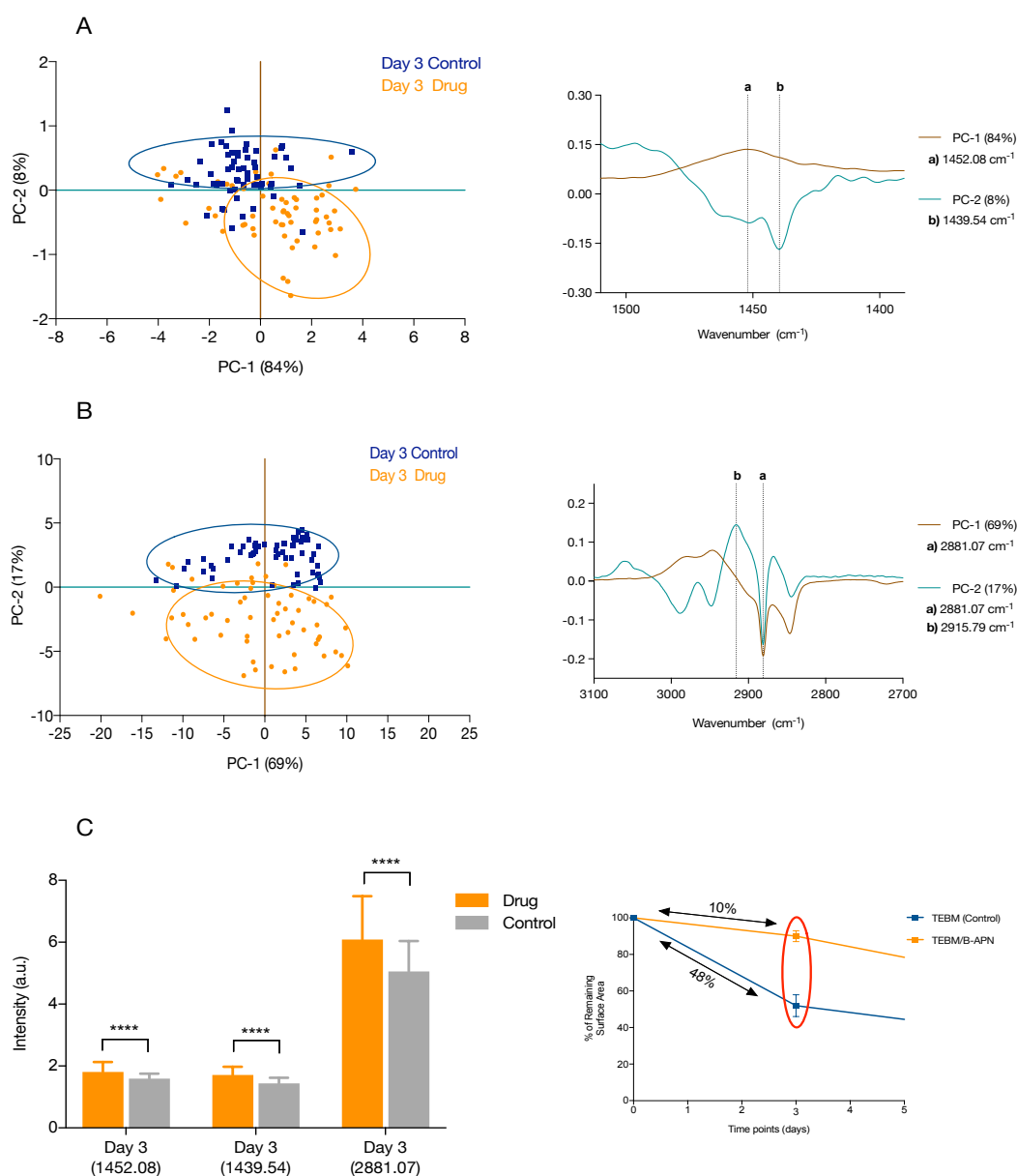


Figure 44: A) PCA score plot (left) and loadings (right) of the 1510-1390 spectral region. According to the PCA analysis of day 3, spectral data from TEBM models is mostly separated from TEBM/ β -APN group by PC-1 and PC-2 loadings. Accounting for 84% of variation in the 1452 cm^{-1} band and 8% in the 1440 cm^{-1} band. B) PCA score plot (left) and loadings (right) of the 3100-2700 spectral region. Responsible for the separation between groups, 69% of the variation was found in the 2881 cm^{-1} band for PC-1, whereas 17% was

shared between 2881 and 2916 cm^{-1} bands for PC-2. C) Unpaired t-test analysis of 1452, 1440, and 2881 cm^{-1} intensity bands for control and drug group (left) and an approximation of the amount of contraction from day 0 to day 3 seen in both groups. These analyses showed that the content of lipids reflected on those three bands is significantly higher ($p < 0.0001$) for the TEBM/ β -APN data, with $\sim 10\%$ reduction in surface area, when compared to the control group, with $\sim 48\%$ reduction of surface area.

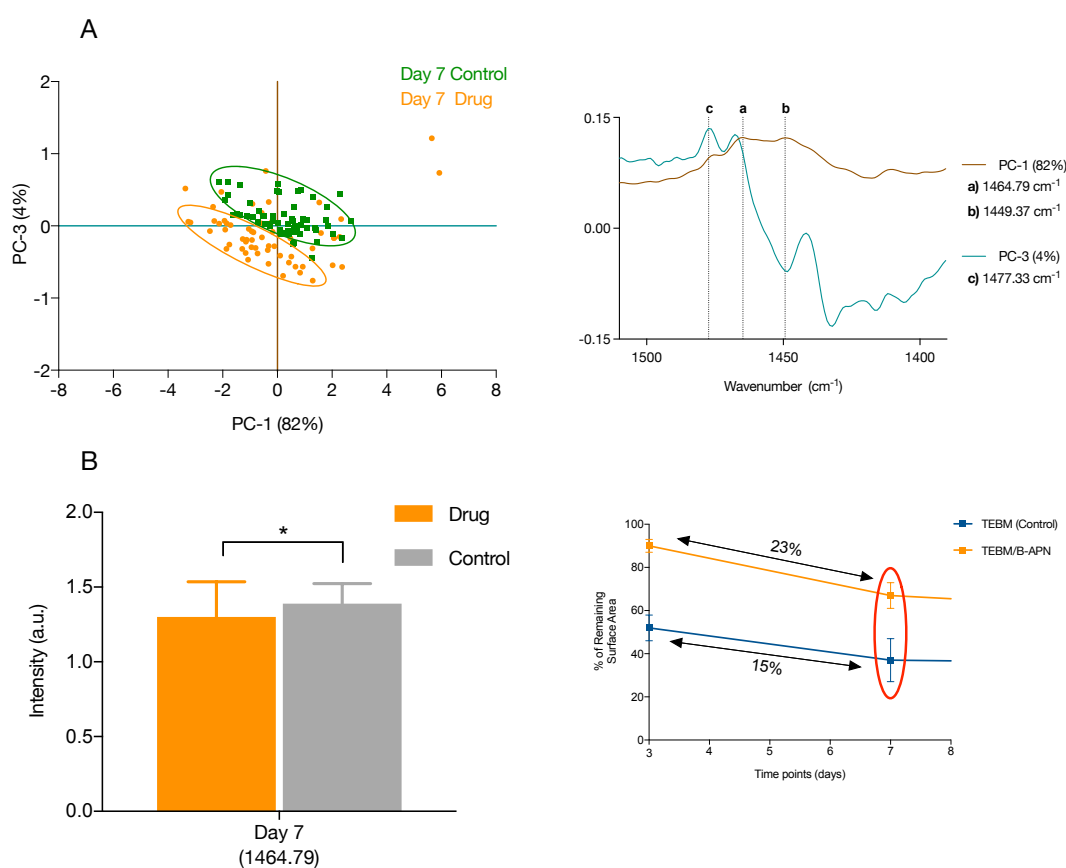


Figure 45. A) PCA score plot (left) and loadings (right) of the 1510-1390 spectral region. According to the PCA analysis of day 7, spectral data from TEBM models is mostly separated from TEBM/ β -APN group by PC-1 and PC-3 loadings. Accounting for 82% of variation in the 1465 and 1449 cm^{-1} bands, and 4% in the 1477 cm^{-1} band. B) Unpaired t-test analysis of 1465 cm^{-1} intensity band for control and drug group (left) and an approximation of the amount of contraction from day 0 to day 3 seen in both groups. These analyses showed that the content of lipids reflected on those three bands is significantly higher ($p < 0.0001$) for the TEBM/ β -APN data, with $\sim 10\%$ reduction in surface area, when compared to the control group, with $\sim 48\%$ reduction of surface area.



RESULTS & DISCUSSION.

Characterising Contraction in a TEBM/ β -APN Model With Raman Spectroscopy

contraction from day 3 to day 7 in both groups. These analyses showed that the content of lipids reflected on day 7 is lower in the TEBM/ β -APN model, with ~23% reduction in surface area, when compared to the control group, with only ~15% reduction of surface area ($p < 0.0118$).

7.1.3.2 PAPILLARY AND RETICULAR LAYER

Since 80% of the dermis is mainly composed by collagen type I, it is expected to see highly similar results in both the papillary and reticular layer. Nevertheless, both layers were analysed separately and only after comparing results it was noticeable that the effects shown in both layers were highly similar with, in some cases, only a delayed effect in timepoints. This resulted in the cascade effect and therefore it was decided to report together the conformational changes seen in collagen molecule after the incorporation of β -APN drug. This section reports on the conformational changes detected mainly in the secondary structure of proteins, together with the reaction of pivotal amino acids considered as biomarkers for the presence of collagen molecule. In the previous chapter it was reported how contraction in a TEBM model produced biochemical changes that can be easily identified by day 3 with Raman Spectroscopy. However, after the incorporation of β -APN, changes in collagen molecule became less noticeable and therefore, more difficult to identify. The MVA technique was capable of identifying subtler differences in Amide I, Amide III and Amino acid spectral regions.

Biochemical changes reflected in secondary structure of collagen.



RESULTS & DISCUSSION.

Characterising Contraction in a TEBM/ β -APN Model With Raman Spectroscopy

When analysing the effect of β -APN in a TEBM graft, differences in the secondary structure of collagen molecule were noted when compared to our control model. For instance, the PCA performed in the Amide I region (1800 - 1510 cm^{-1}) highlighted the spectral differences responsible for a separation between the TEBM and the TEBM/ β -APN data.

Accountable for this separation is the combination of PC-1 and PC-2 loadings. According to the score plot in **Figure 46A**, TEBM models after 3 days of contraction showed a higher content of α -helix secondary structure, together with phenylalanine and tyrosine residues. This observation was also noticed when comparing TEBM with TEBM/ β -APN at day 7 **Figure 46B** and at day 14 **Figure 46C**. The previous data goes in agreement with the data from **Figure 36**, which shows that the content of α -helix and tyrosine residues increases as a function of time during contraction.

However, the incorporation of β -APN to inhibit contraction in the TEBM grafts lead to different changes after 3 days of contraction. In contrast, TEBM/ β -APN showed a higher content of C=O stretching vibrations from β -sheet and disordered structures, reflected at 1677 and 1664 cm^{-1} respectively. This goes in agreement with Robertson et al., who stated that collagen under the effect of

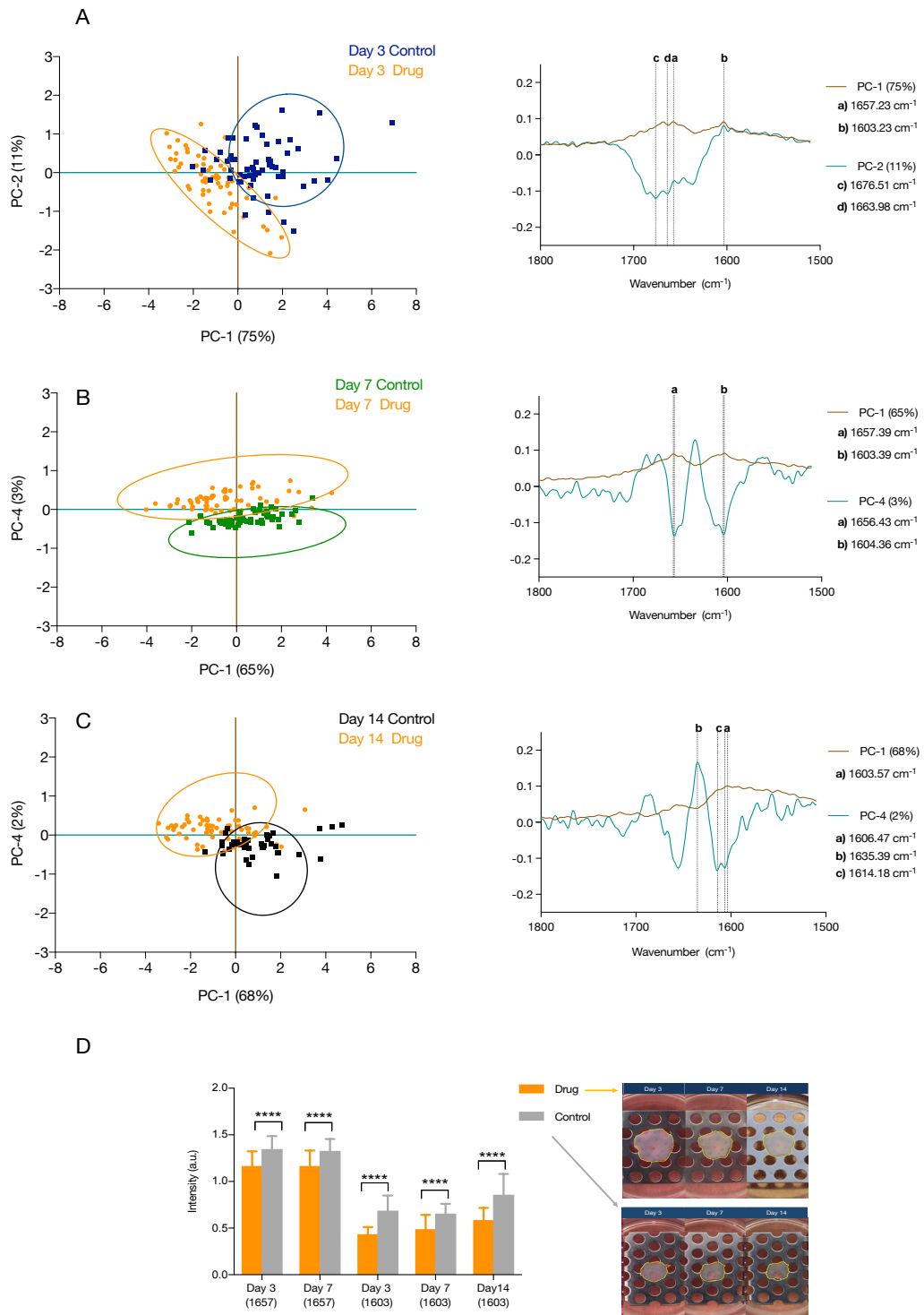


Figure 46. PCA score plot (left) and loadings (right) of the 1800-1510 cm^{-1} spectral region in the papillary layer. A) PCA for day 3. B) PCA for day 7. C)



RESULTS & DISCUSSION.

Characterising Contraction in a TEBM/ β -APN Model With Raman Spectroscopy

PCA for day 14. D) Unpaired t-test analysis of bands at 1657 and 1603 cm^{-1} , since those were the main peak intensities responsible for a separation between groups. Differences in peak intensities between control and drug models are considered highly significant ($p < 0.0001$).

β -APN agent results in the distortion of α -helix chains rendering them unable to crosslink properly to other collagen fibres.¹⁷⁴ These changes are also seen in the reticular layer of TEBM/ β -APN models. Whereas according to **Figure 46**, the incorporation of β -APN has shown a reduction in the content of triple helical structure as well. Not only this, but the presence of disordered structures, 1672 cm^{-1} , only appears until day 14, whereas in the papillary layer this effect appeared since day 3. Since 80% of the dermis is composed by collagen type I fibres it is reasonable to assume that the effects that β -APN has on dermis will be seen in both papillary and reticular layer. Same biochemical changes seem to appear at different timepoints between layers, giving the appearance of the cascade effect where the effect is first seen in the papillary and then extended to the reticular layer. Additionally to this, a significantly lower content of tyrosine residue were detected in the TEBM/ β -APN data when compared to the control group **Figure 46** and **Figure 47**. Two possible theories can explain these results: (i) binding of β -APN drug to the active site of LOX enzyme, which contains tyrosine as part of the catalytic active site, could be inhibiting the vibration of this residue or (ii) the higher content of β -sheet structure keeps the amino acid side chains clustered and less exposed to vibration when samples are being analysed. It is well documented that residues such as tyrosine, phenylalanine



RESULTS & DISCUSSION.

Characterising Contraction in a TEBM/ β -APN Model With Raman Spectroscopy

and tryptophan tend to form β -sheet secondary structures due to their bulky side chains.¹⁷⁵ Compared to this, in the TEBM graft, the presence of in-plane bending vibration of tyrosine and phenylalanine reflected at 1603 might be an indication of the presence of LOX enzyme or rearrangement of the collagen fibres. As stated on the previous data, as contraction increases so does the content of α -helix secondary structure. In agreement with Floramonte et al.,¹⁷⁵ the biochemical structure of both alpha and beta secondary structures dictate the precise orientation of the amino acid side chains. Thus, in the case of α -helix structure, side chains are naturally exposed towards the outside of the central axis and hence more susceptible to vibrate than when compared to the β -secondary structure in the drug model.

Furthermore, apart from showing lower than the average amount of tyrosine residues, according to Dukor et al.,¹⁷⁶ the higher content of 1635 cm^{-1} band seen in the PCA for TEBM/ β -APN at day 14, is representative of differences in collagen content **Figure 46C**. This goes in agreement with Chakrabarty et al. work,⁴⁰ where it was reported that no degradation or synthesis of collagen fibrils was detected during contraction of soft-tissue grafts, but instead an increase in dermal mass measurement was noticeable with increasing contraction.⁴⁰ It would be reasonable to suggest that the inhibition of LOX

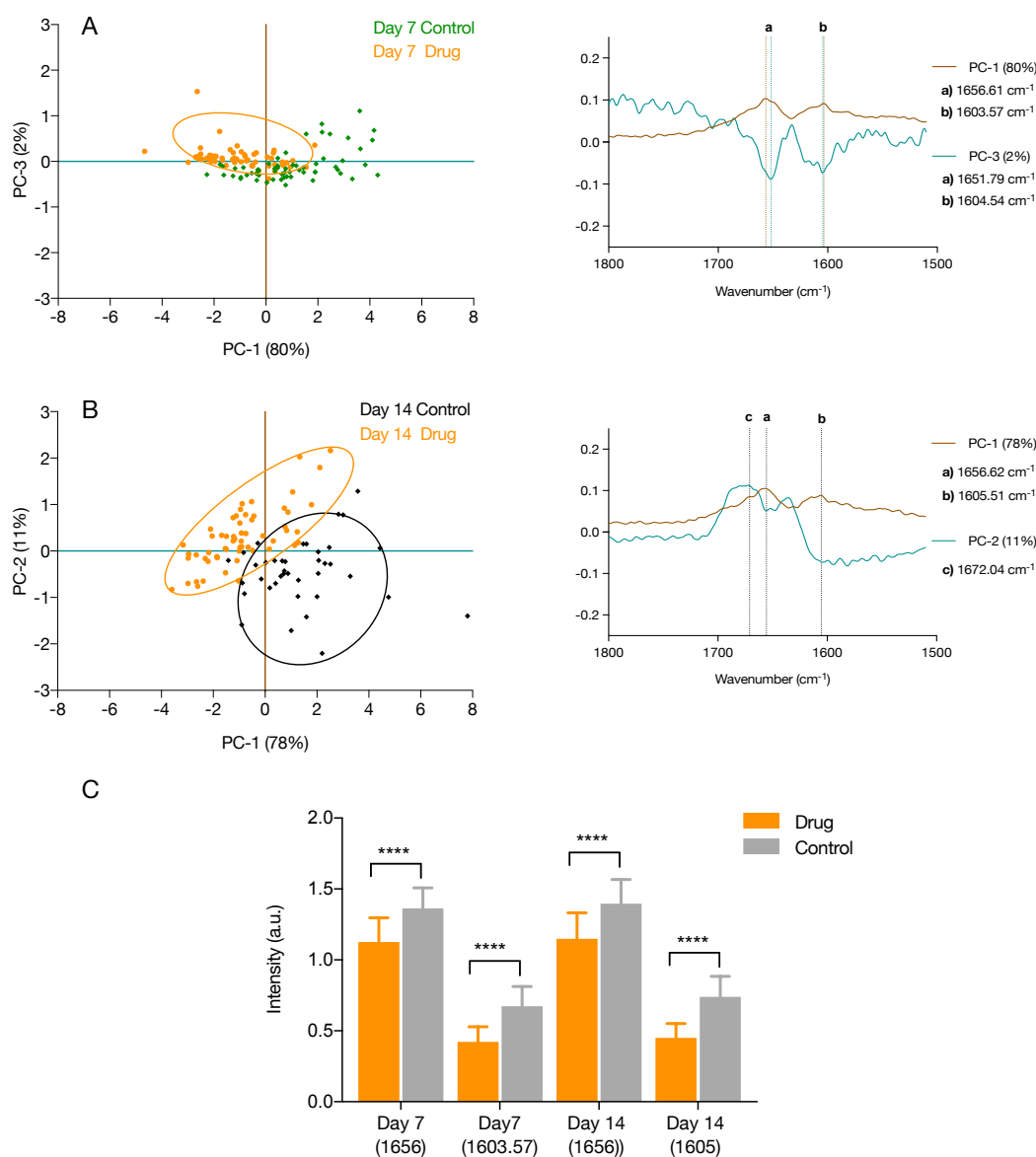


Figure 47. PCA score plot (left) and loadings (right) of the 1800-1510 cm^{-1} spectral region in the reticular layer. A) PCA for day 7. B) PCA for day 14. C) Unpaired t-test analysis of bands 1656 and $\sim 1603 \text{ cm}^{-1}$, since those were the main peak intensities responsible for a separation between groups. Differences in peak intensities between control and drug models are considered highly significant ($p < 0.0001$).



RESULTS & DISCUSSION.

Characterising Contraction in a TEBM/ β -APN Model With Raman Spectroscopy

activity by β -APN lead to the reduction of collagen crosslinking, hence resulting in a less compacted and fibrotic ECM and translating into less content of collagen fibres within the focal point of analysis.

Amide III as a biomarker of collagen cross linking.

As seen in the previous chapter, amide III reflected interesting information in the contraction of TEBM graft. It was established that the stretching vibration of C-N decreases (1245 cm^{-1}) whereas the twisting vibration of CH_3 increases (1335 cm^{-1}) as a function of time during contraction. After introduction of β -APN into the TEBM models, this biomarker was no longer noticeable. Instead it can be seen in **Figure 48** the separation between control and drug data, where TEBM/ β -APN at day 3 shows a higher content of 1244 cm^{-1} , which according to Lakshimi et al., corresponds to the C-N stretching vibration from β -sheet and random coils structures.¹⁶⁹ This goes in agreement with the higher content of β -sheet and unordered structures (1677 cm^{-1} and 1664 cm^{-1}) seen in **Figure 47A** when analysing the Amide I region. Together with this, TEBM/ β -APN also showed a lower content than the average with respects to the twisting vibrations of CH_3 and CH_2 bands. This observation is also present at day 7 and day 14, where according to PC-2 loadings, TEBM/ β -APN still shows a higher amount of C-N stretching together with a lower amount of twisting vibration from CH_3 and CH_2 **Figure 48B,C**. As explained before, since β -APN is responsible for the inhibition of LOX activity, partial inhibition of collagen crosslinking has been achieved. This translates into less twisting and wagging vibration from the CH_3



RESULTS & DISCUSSION.

Characterising Contraction in a TEBM/ β -APN Model With Raman Spectroscopy

and CH₂ groups located at the side chains of helical residues such as glycine and proline. If β -sheet has been the structure prevailing in the TEBM/ β -APN data, it is reasonable to assume that due to the biochemical structure of this secondary structure, orientation side chains from Gly and Pro residues might be less exposed. This observation is also highlighted in the reticular layer when analysing the amide III region. A lower amount of CH₂ and CH₃ wagging vibrations from glycine and proline residues is seen in TEBM/ β -APN group when compared to the control data. Together with this, a higher amount of C-N and N-H stretching vibrations from β -sheets and disordered structure is highly significant ($p < 0.0001$) when compared to control data. Since the triple motif of Gly-Pro-Hypro is characteristic of the α -helical structure of collagen, it is reasonable to assume that treatment with β -APN resulted in the distortion and interruption of the triple helix structure and thus disruption of the Gly-Pro-Hypro order. This resulted in a significant reduction of CH₂ and CH₃ vibration from side chains of these residues that is indirectly correlated to the increase in β -sheet structure.

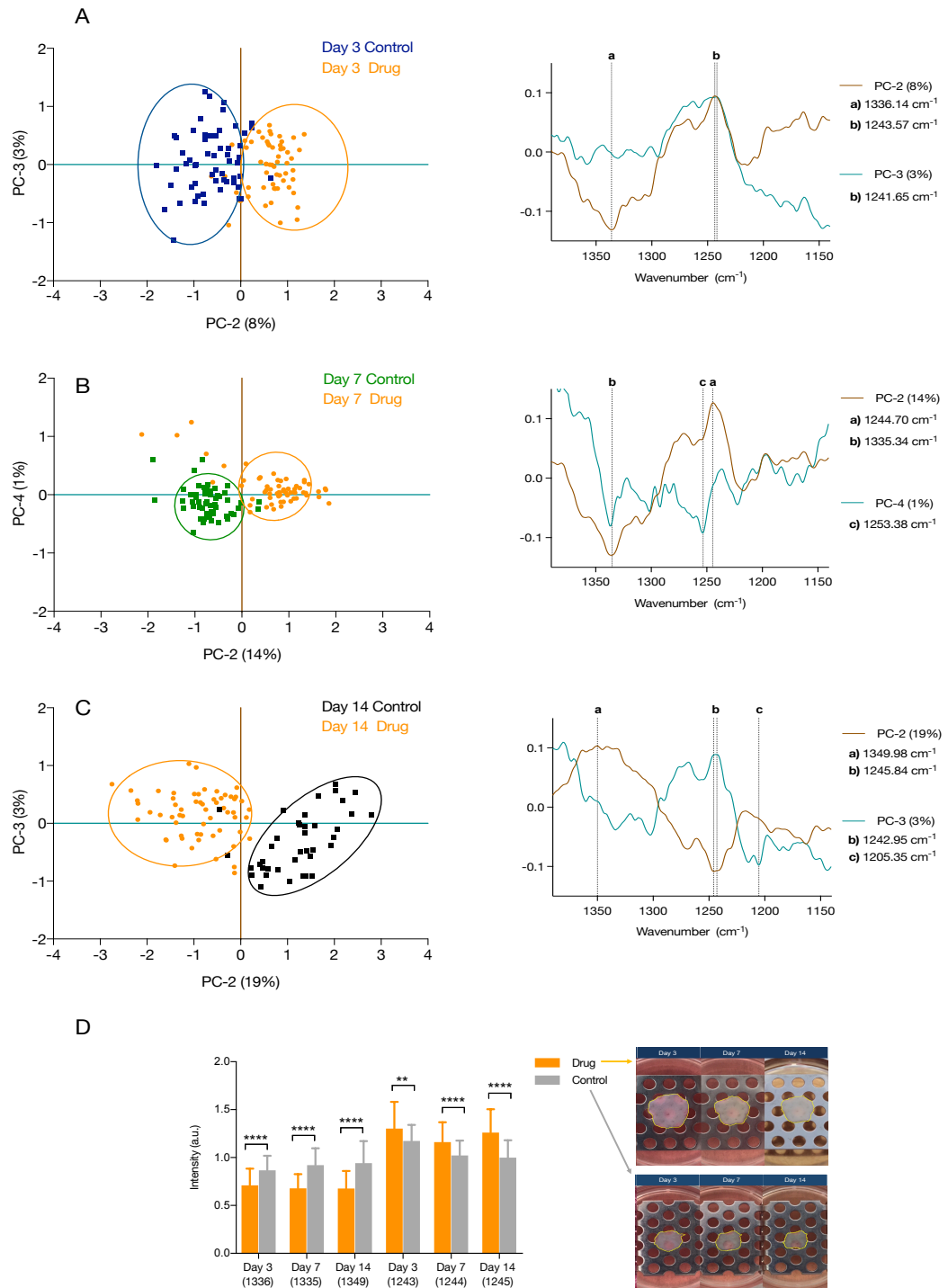


Figure 48. PCA score plot (left) and loadings (right) of the 1390-1140 cm^{-1} spectral region in the papillary layer. A) PCA for day 3. B) PCA for day 7. C) PCA for day 14. D) Unpaired t-test analysis of intensity bands ~ 1335 and ~ 1244

cm^{-1} , since those were the main peak intensities responsible for a separation between groups. Differences in peak intensities between control and drug models are considered highly significant ($p < 0.0001$) for all analyses, except for the 1243 cm^{-1} band at day 3 that showed a $p < 0.0024$.

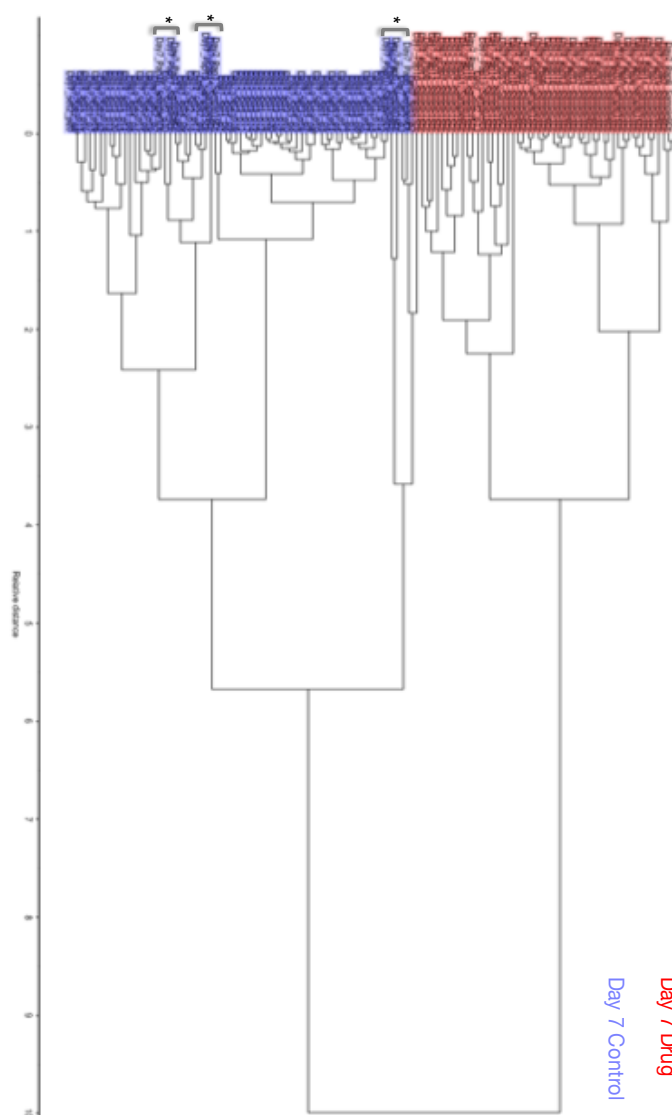


Figure 49. CA of Amide III region on Day 7 of contraction on both, TEBM & TEBM/ β -APN model. When analysing the amide III region, the unsupervised method clustered the control data and separate it from the drug data,

complementing the results of the PCA. Only few spectral points from the drug data clustered into the control group (*).

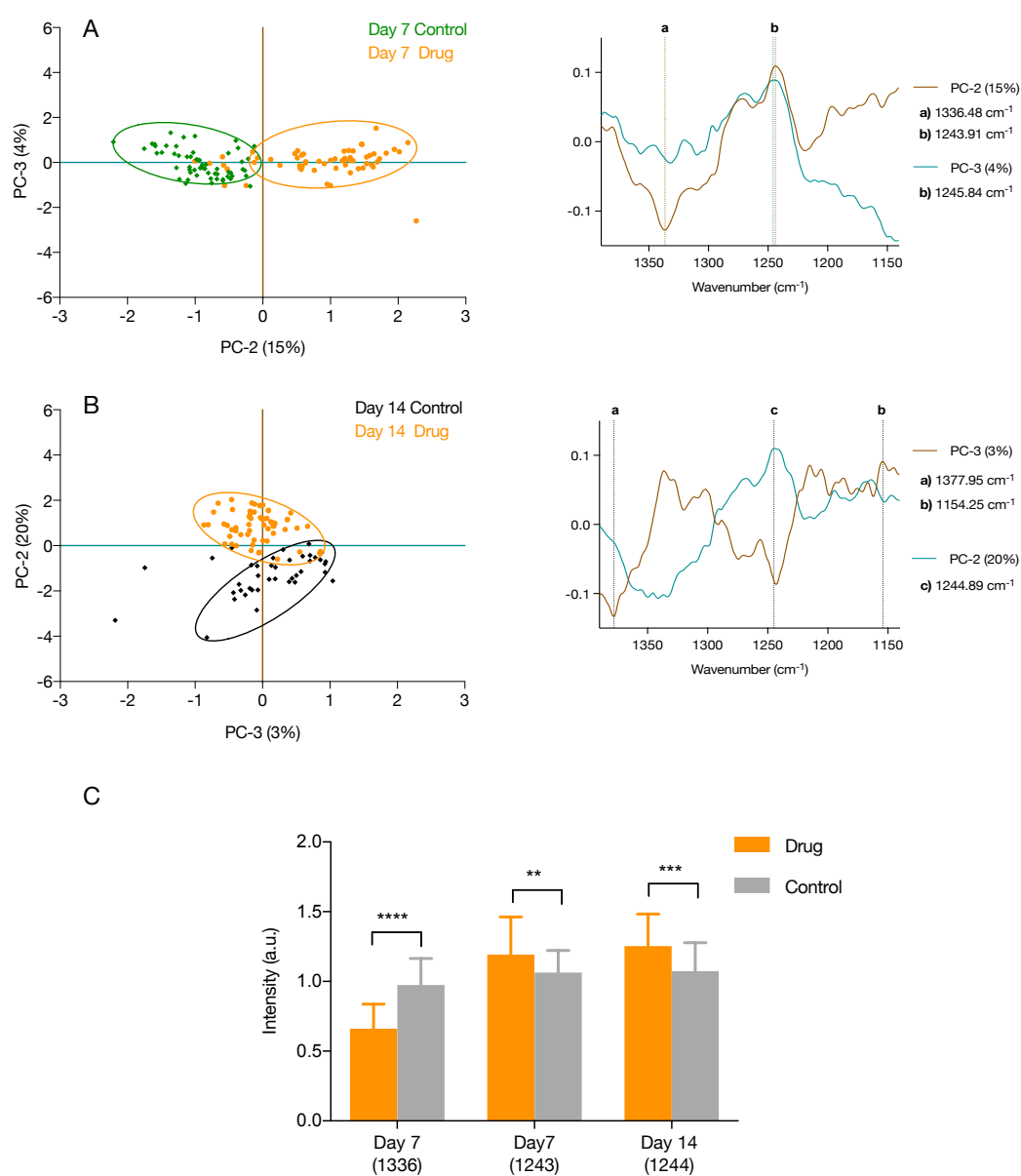


Figure 50. PCA score plot (left) and loadings (right) of the 1390-1140 cm^{-1} spectral region in the reticular layer. A) PCA for day 7. B) PCA for day 14. C) Unpaired t-test analysis of intensity bands at ~ 1336 and ~ 1244 cm^{-1} , since those



RESULTS & DISCUSSION.

Characterising Contraction in a TEBM/ β -APN Model With Raman Spectroscopy

were the main peak intensities responsible for a separation between groups. Differences in peak intensities between control and drug models are considered highly significant ($p < 0.0001$) for all analyses, except for the 1243 cm^{-1} band at day 7 and day 14, which showed a p.value of 0.0017 and .0001 respectively.

Relation between hydroxyproline residues and TEBM/ β -APN Model

When analysing the amino acids region ($980 - 600 \text{ cm}^{-1}$) with PCA, a separation between TEBM and TEBM/ β -APN data becomes clear at day 3, 7 and 14. Coincidentally, responsible for this separation in all time points is PC-1 and PC-3 loadings. According to the score plot and loadings in **Figure 51**, there is a higher content, in the TEBM/ β -APN group, of C-C stretching vibration of proline ring and breathing ring of hydroxyproline residue, reflected at 855 cm^{-1} [23,24]. Additionally to this, amino acid side chains from proline and hydroxyproline together with C-C stretching vibration of collagen backbone are reflected in higher content at 937 cm^{-1} band. According to Gullekson et al., the unique aromatic structure of proline's side chain gives the amino acid a high conformational rigidity, directly affecting the bond formation with other amino acids and hence the nearest secondary structure to this residue.⁷³ Thus, it is considered that the presence of proline residue usually results in the interruption of the nearest secondary structure from continuing with its usual orientation. Moreover, according to Qiu et al., variations in the content of hydroxyproline residue has been continuously used as an indicator of diseases caused by abnormalities in collagen metabolism.¹⁷⁷ Treatment with β -APN agents inhibit crosslinking within and/or with other collagen fibres. This interruption often



RESULTS & DISCUSSION.

Characterising Contraction in a TEBM/ β -APN Model With Raman Spectroscopy

leads to increasing content of what is known as soluble collagen. As stated by Robertson et al., excess of free hydroxyproline residues in the connective tissue might result in urinary disposal of the amino acid.^{174,178} In this case and in agreement with the previous statement, the higher amount of hydroxyproline residue found in both the papillary and reticular layer could be free hydroxyproline peptides ready to be disposed as a by-product of the disruption of α -helical structures. It has been well documented that treatment with β -APN goes together with increase content of urine hydroxyproline.^{179,180} This correlates with Keiser et al. findings, which state that higher amounts of soluble collagen after treatment with β -APN is accompanied by increased content of hydroxyproline in urine.¹⁸¹ The higher content of hydroxyproline ring vibration might be indicating that due to a lack of spontaneous crosslinking, collagen fibres might be having more flexibility to vibrate higher than when compared to the control data. β -APN is inhibiting the enzymatic conversion of telopeptide lysines and excessive crosslinking of telopeptide allysines to the α -helix structure, resulting in higher amount of soluble collagen and less fibrotic connective tissue.

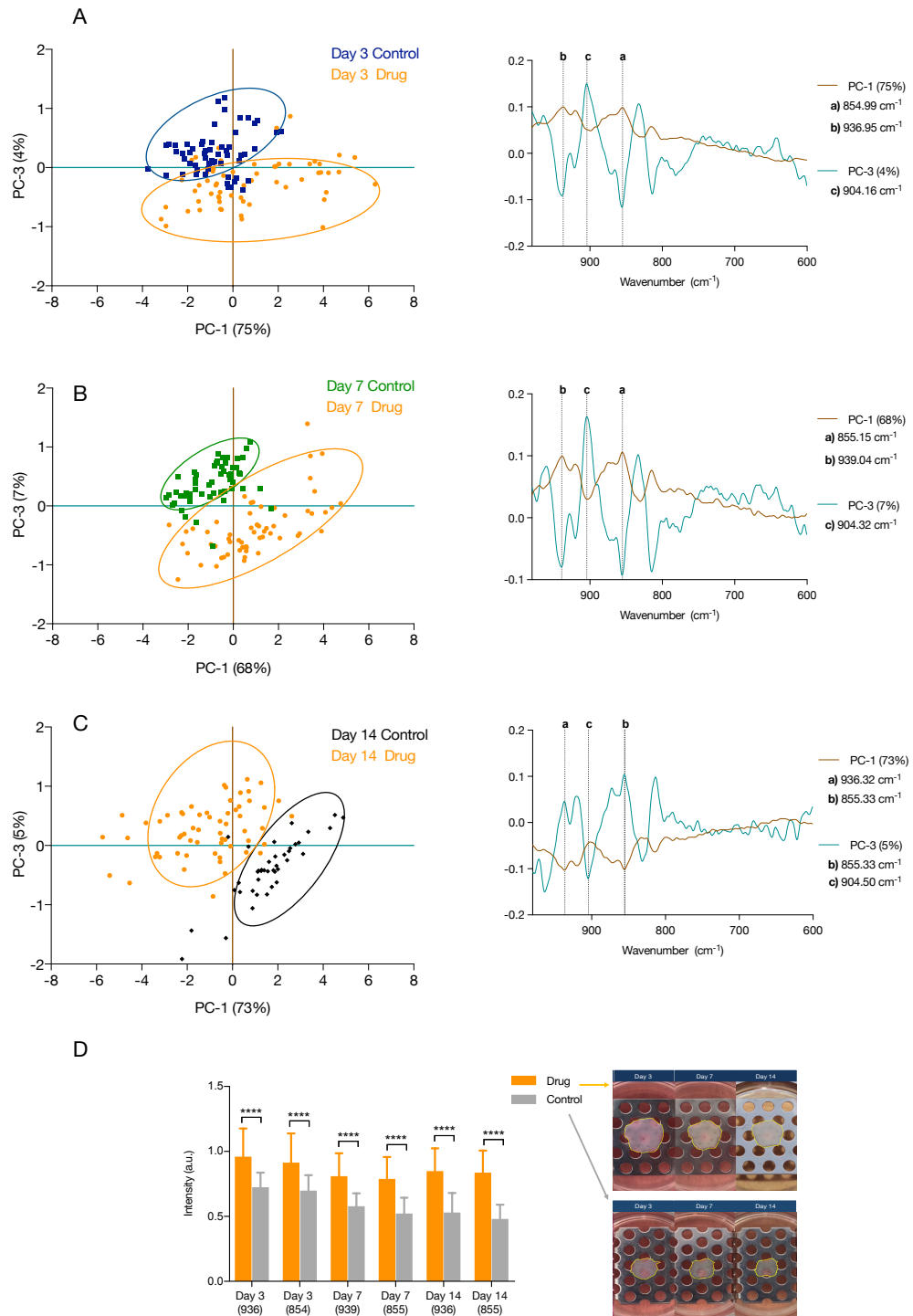


Figure 51. PCA score plot (left) and loadings (right) of the 980-600 cm^{-1} spectral region in the papillary layer. A) PCA for day 3. B) PCA for day 7. C) PCA for day 14. D) Unpaired t-test analysis of intensity bands at ~ 936 and ~ 855

cm^{-1} , since those were the main peak intensities responsible for a separation between groups. Differences in peak intensities between control and drug models are considered highly significant ($p < 0.0001$) for all time points.

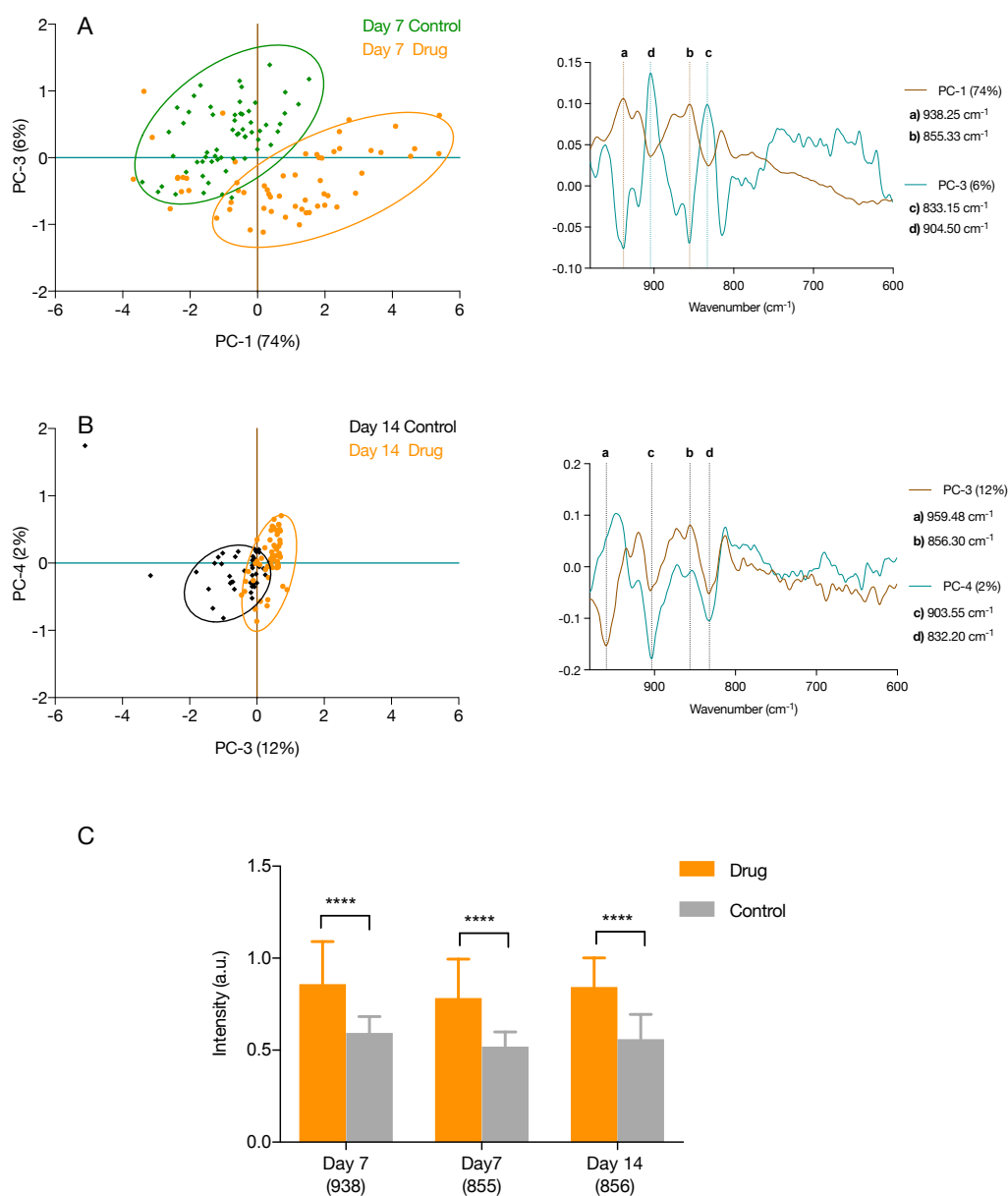


Figure 52. PCA score plot (left) and loadings (right) of the 980-600 cm^{-1} spectral region in the reticular layer. A) PCA for day 7. B) PCA for day 14. C) Unpaired t-test analysis of ~ 936 and $\sim 855 \text{cm}^{-1}$ intensity bands, since those were



RESULTS & DISCUSSION.

Characterising Contraction in a TEBM/ β -APN Model With Raman Spectroscopy

the main peak intensities responsible for a separation between groups. Differences in peak intensities between control and drug models are considered highly significant ($p < 0.0001$) for all time points.

7.2 SUMMARY

Biochemical changes were successfully detected by Raman spectroscopic analysis despite the partial inhibition of contraction in TEBM models with β -APN. RS and the use of MVA techniques identified main biomarkers involved in the inhibition of contraction due to the incorporation of β -APN. The characteristic rigidity of an overexpression of collagen crosslinking was disturbed with the incorporation of this drug, which lead to a higher occurrence of disordered β -sheet collagen fibres instead. Utilising lipids as the main source of energy, it can be concluded that with the incorporation of β -APN, the peptide bond (Amide III region) no longer contributed to the formation of triple helix structure, but instead lead to an unorganised rearrangement of collagen fibres. RS also highlighted the concentration of free hydroxyproline residues as a by-product of the rearrangement of this secondary structure. This conclusion leads to the possibility of considering the peptidic bond (Amide III region) as a focal point for the progression of contraction, which independently upon the addition of β -APN, plays an active part in the formation of non-enzymatic crosslinks.

8 CONCLUSION AND FUTURE WORK

Graft contraction continues to be a poorly understood clinical problem and a better insight into the underlying biochemical mechanism behind contraction is still very much needed. The use of Raman spectroscopy highlighted trends and biomarkers that can be considered as target points to tackle the routes of progression of graft contracture.

This research established the peptidic bond (Amide III region) as a biomarker for monitoring the extent of contraction. Where overexpression of crosslinking occurred, so did the formation of α -helix conformation of keratin and collagen proteins. Where crosslinking was prevented through inhibition of LOX activity, the triple helix conformation of both proteins was disrupted and instead rearranged into unorganised and β -sheet conformation. This observation was first manifested in the peptidic bond of keratin polypeptide chains from the epithelium layer, and four days after in the peptidic bond of the collagen fibres from the papillary and reticular layer. Supporting the theory that contraction of oral mucosa and skin grafts is due to contractile forces of keratinocytes and expanding later on towards the rearrangement of collagen fibres. The above findings are of clinical relevance because it opens up the possibility of considering targeting the peptidic bond of both proteins (keratin and collagen), as the starting point, to prevent the cascade effect of the natural progression of contraction.

It would be interesting to carry these findings further and focus some research on:

- Investigating this particular bond, and its potential to prevent the contractile forces of keratinocytes and the cascade effect of contraction, as a complementary measure to the inhibition of LOX activity by β -APN.
- The production of tissue-engineered normal skin models (TENS), which mimic as much as possible the *in vivo* human skin, before and after incorporation of β -APN drug. Utilizing different doses to analyse to what extent contraction can be inhibited. Raman analysis of contraction in these models at different time points and therefore interpretation of result.
- Comparison of TEBM with TENS results would be a good study to corroborate even more the biomarkers and processes described in this thesis as part of contraction. Although both soft tissues are highly similar, it has been reported that TEBM models tend to contract slightly more than TENS models.
- If available, apply the same experimental procedure with a different pharmacological agent for contraction modulation. For example, the use of D-Penicillamine would be an appropriate candidate to investigate. D-Penicillamine is known to be an inhibitor of collagen cross-linking by

blocking lysyl-derived aldehydes through the formation of thiazolidine rings. Thereby, in theory, lysyl-derived aldehydes would no longer be able to easily cross-link with the amide group towards formation of a secondary amide. It would also inhibit the cross-linking between reactive derived-aldehydes. It would be interesting to see the effects exhibited in the model after incorporation of D-Penicillamine, and to analyse the extent of contraction and inhibition of the crosslinking of the fibres.

- These findings have highlighted another potential route for collagen cross-linking. From a broader perspective, it would be of value to test both theories of contraction (inhibition of lysyl oxidase, and inhibition of aldol condensation reactions) with the same experimental design, both in skin and oral mucosa models. Taking into consideration that each route is targeted through different pharmacological agents, it would be interesting to see if both drugs can be used together, in moderation, to test the effect they have on contraction.

Finally, it has been concluded that Raman spectroscopy together with MVA techniques are highly capable of identifying differences and biomarkers without previous knowledge of the theory behind a physiological process. In this case, the results obtained from these studies corroborated and contributed to the literature available to date in terms of collagen crosslinking and the effect of the β -APN drug. It is interesting how Raman analysis of the data can highlight biomarkers that might be reflecting changes in the metabolism of specific



CONCLUSION & FUTURE WORK

molecules. This technique shed light to metabolism of lipids and hydroxyproline that might be taking place as part of the contraction process of soft tissue engineered models.

9 APPENDIX

9.1 GREENS MEDIUM COMPOSITION:

- Dulbecco's Modified Eagle's Medium (DMEM) + Ham's F-12 Medium
- In a 3:1 ratio respectively

Supplemented with:	
FCS 10%	50 ml
Adenine	2 ml
Glutamine	5 ml
Fungizone	1.25 ml
Penicillin + Streptomycin	5 ml
Insulin	2.5 ml
Hydrocortisone	80 μ l
EGF	2.5 ml
Triiodothyramine (T/T)	500 μ l
Cholera Toxin	500 μ l

9.2 FIBROBLAST'S MEDIUM COMPOSITION:

Dulbecco's Modified Eagle's Medium (DMEM)

Supplemented with:	
FCS 10%	50 ml
Glutamine	5 ml
Fungizone	1.25 ml
Penicillin + Streptomycin	5 ml

9.3 PREPARATION OF DED

Before starting the procedure, make sure to arrange the following materials inside the LAF:

1. Three universal tubes
2. Universal rack
3. IMS inside one of the universal tubes
4. Two forceps
5. One Scalpel with blade
6. Waste container
7. Petri dish with a bit of Green's medium

8. Small ruler
9. Marker container
10. Allograft
11. PBS
12. 1 mol of NaCl

When preparing allograft that has been stored in glycerol, the following instructions must be followed,

1. Transfer allograft from glycerol into container “1” full of PBS.
2. Keep allograft in incubator at 37 C for 24 hours.

After 24 hours...

3. Transfer allograft from PBS to a new container full of PBS.
4. Repeat step 2.

After 24 hours...

5. Transfer allograft from PBS to a new container full of PBS.
6. Repeat step 2

After 24 hours...

7. Transfer allograft from PBS to a new container with 1mol NaCl
8. Repeat step 2

After 24 hours...

9. With the ruler and a marker, trace a 2 cm² square under the petri dish surface
10. Place allograft insides the LAF and transfer it from the container into the petri dish.
11. With the forceps, gently expand the whole allograft, making sure epidermis is facing upwards.
12. Try to gently remove the epithelium from the dermis and place it aside were it would not be disturbed.
13. If the epidermis comes out easily, proceed by cutting the dermis in 2 cm² by following the trace that has been previously drawn under the petri dish surface.
14. Place each dermis sample in each six well plate, using a total of 3 six-well plates.

9.4 PASSAGING OF CELLS

1. Remove the entire medium from the flask with a 15 mL pipette and discard it in a bleach beaker.

2. Wash the cells with 10 mL of PBS.
3. Remove all the PBS from the flask with a 15 mL pipette and discard it in the bleacher beaker.
4. Add 5mL of Trypsin.
5. Put the cells in a CO₂ incubator for 5 minutes to make sure most of the cells have detached.
6. After 5 minutes, remove the cells from the incubator and add 5 mL of medium (equal volume as with trypsin).
7. With a 15 mL pipette, remove all the content from the flask and transfer it to a universal tube.
8. Centrifuge at 1000 rpm/5 minutes with a bench top centrifuge.
9. Carefully discard the supernatant in a bleacher beaker.
10. Place the cell-pellet in a new flask with 10 mL of culture medium.
11. Incubate the flask for 2 or 3 days in the CO₂ incubator
12. After 2 or 3 days, look at the cells under a microscope and determine whether or not they have reached 80% confluence, and if they have, repeat the process from 1 to 12.
13. If they have reach 80% confluence, proceed to do cell counting with trypan blue and then seed on DED

9.5 FREEZING CELLS

Before starting the procedure, make sure to arrange the following materials inside the LAF:

1. Fibroblast Medium
2. Pipette boy
3. 10 mL pipettes
4. Waste container
5. Universal tubes
6. Universal rack
7. DMSO
8. Cryovials
9. Cryovials rack
10. New T75 flask
11. Fibroblast flask

To froze cells, follow the protocol below:

1. With the 10 mL pipette, transfer Fibroblast Medium from the T75 flask to the waste container (avoid touching the T75 surface where cells are attached).
2. With a new 10 mL pipette, transfer 6 mL of PBS from the PBS container to the T75 flask. Rinse the surface of the flask for 10 seconds and proceed by discarding the PBS into the waste container (always using a new 10 mL pipette).
3. Transfer 5 mL of trypsin aliquot into the T75 flask and incubate it at 37 C for 5 minutes.

After 5 minutes...

4. Place the T75 flask inside the LAF and with a 10 mL pipette transfer the trypsin solution to a universal tube. To neutralise trypsin activity, add 10 mL of Fibroblast Medium into the universal tube and resuspend four times.
5. Centrifuge the universal tube at 1000 rpm/5 min.

After 5 minutes...

6. Place the universal tube inside the LAF and carefully discard the supernatant into the waste container without disturbing the cell pellet.
7. Close the universal tube and tap it against the LAF to resuspend the break down the cell pellet.
8. Add 4 mL of Fibroblast medium into the universal tube and resuspend to create a homogenous cell suspension.
9. From the universal tube, transfer 1 mL of cell suspension into a new T75 flask and label it accordingly.
10. Add 11 mL of Fibroblast medium into the new T75 flask to complete the 12 mL cell suspension.
11. Store the new T75 flask in the incubator at 37 °C.
12. Centrifuge again the remaining 3 mL of cell suspension at 1000 rpm/5 min.
13. Repeat step 6
14. Repeat step 7
15. Add 3 mL of FCS into the universal tube and resuspend to create a homogenous cell suspension.

Before freezing your cells, it is important to do cell counting and find out how dense your cell suspension will be. To achieve this, follow the procedure below:

16. With a micropipette, transfer both, 10 ul of cell suspension and 10 ul of trypan blue into a cryovial. Resuspend it and place 10 ul into the haemocytometer.
17. Proceed with cell counting

After cell counting...

18. With a micropipette, transfer 900 ul of cell suspensions from the universal tube into each cryovial.
19. With a new micropipette, transfer 100 ul of DMSO from the DMSO container into each of the previous cryovials.
20. Close cryovials and quickly placed them inside the -80 C freezer.

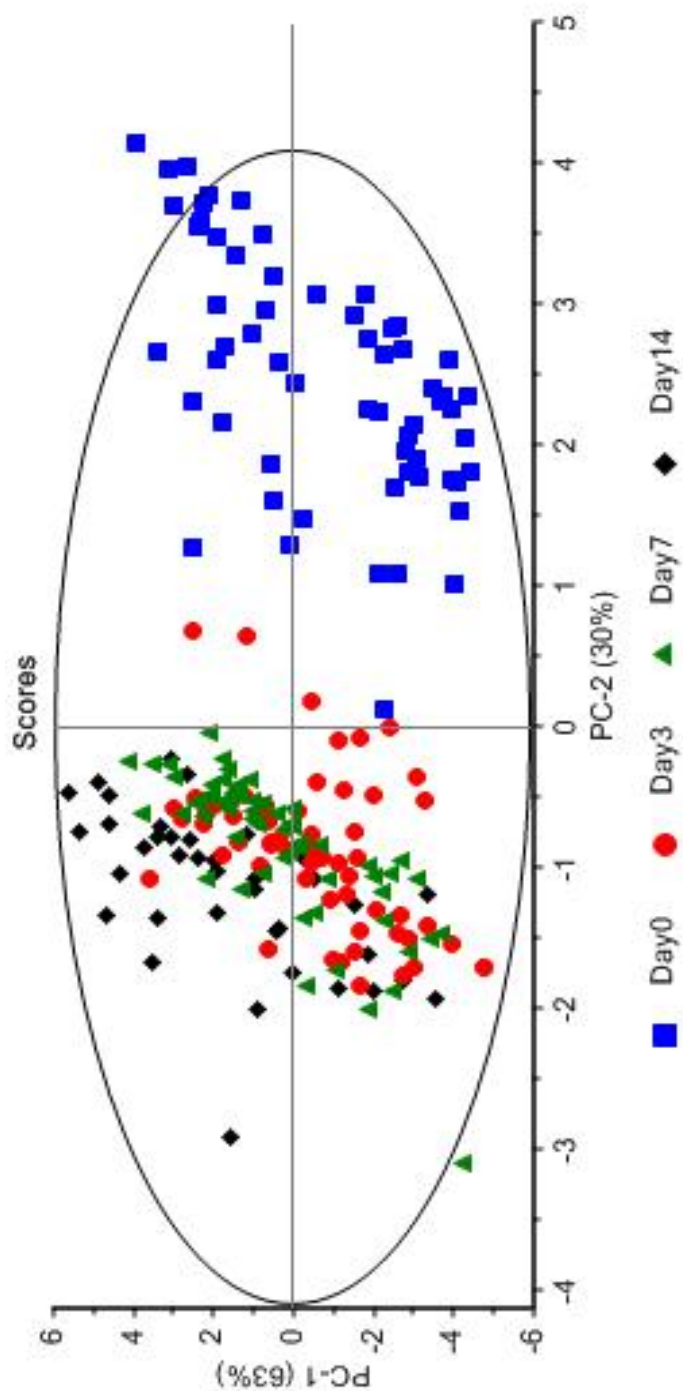


Figure 53. PCA of Amide III region in the epithelium layer. All four time points were analysed in the same matrix resulting in the isolation of day 0 from day 3 and from the rest of the groups. Responsible for this separation are peaks at 1245 and 1339 cm⁻¹.

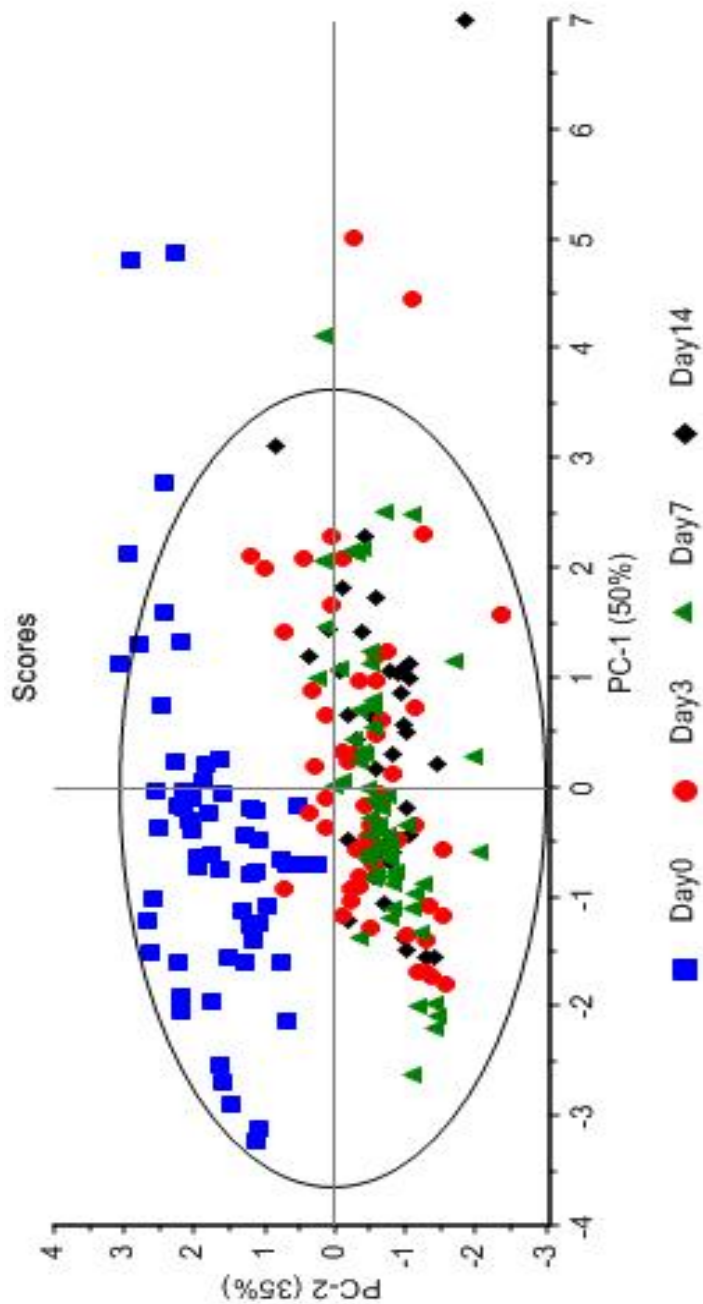


Figure 54. PCA of Amide I region in the epithelium layer. All four time points were analysed in the same matrix resulting in the separation of day 0 from day 3 and the rest of the groups. Responsible for this separation are peaks at 1605 and 1613 cm^{-1} .

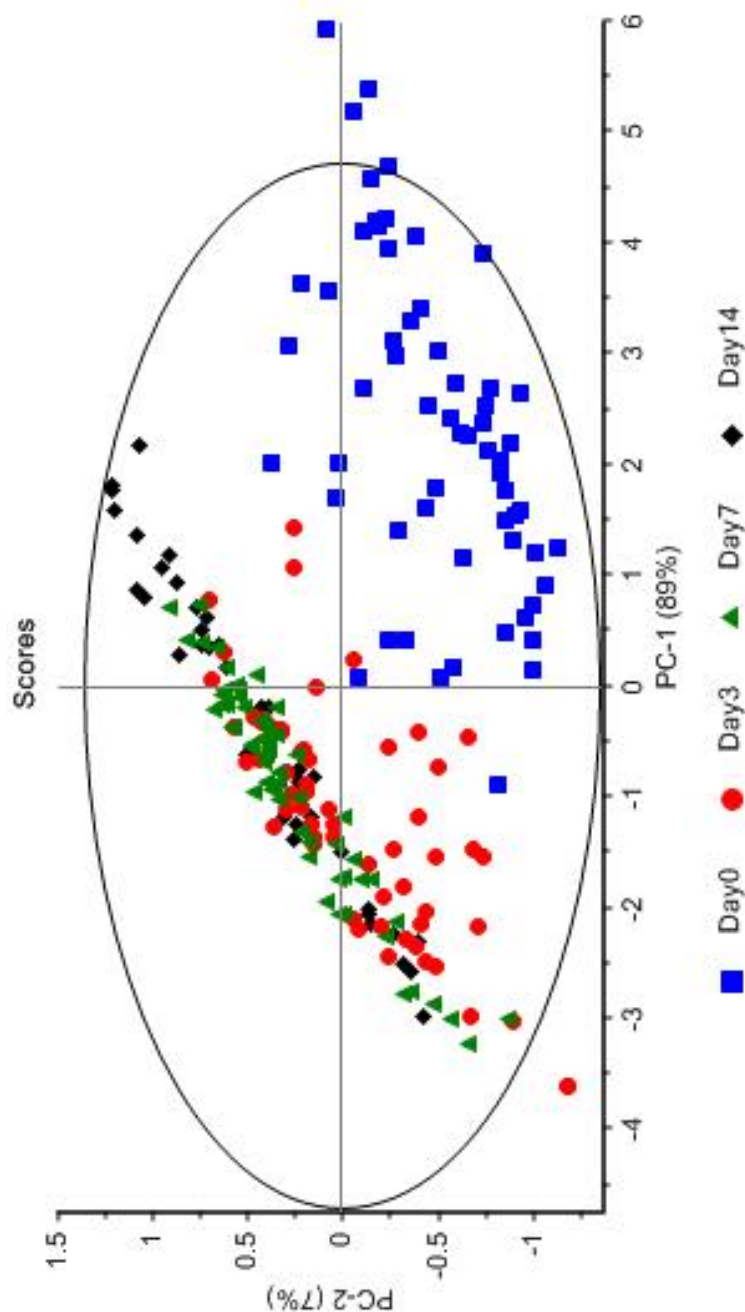


Figure 55. PCA of Amino acids region in the epithelium layer. All four time points were analysed in the same matrix resulting in the separation of day 0 from day 3 and the rest of the groups. Responsible for this separation are peaks at 872 and 920 cm^{-1} .

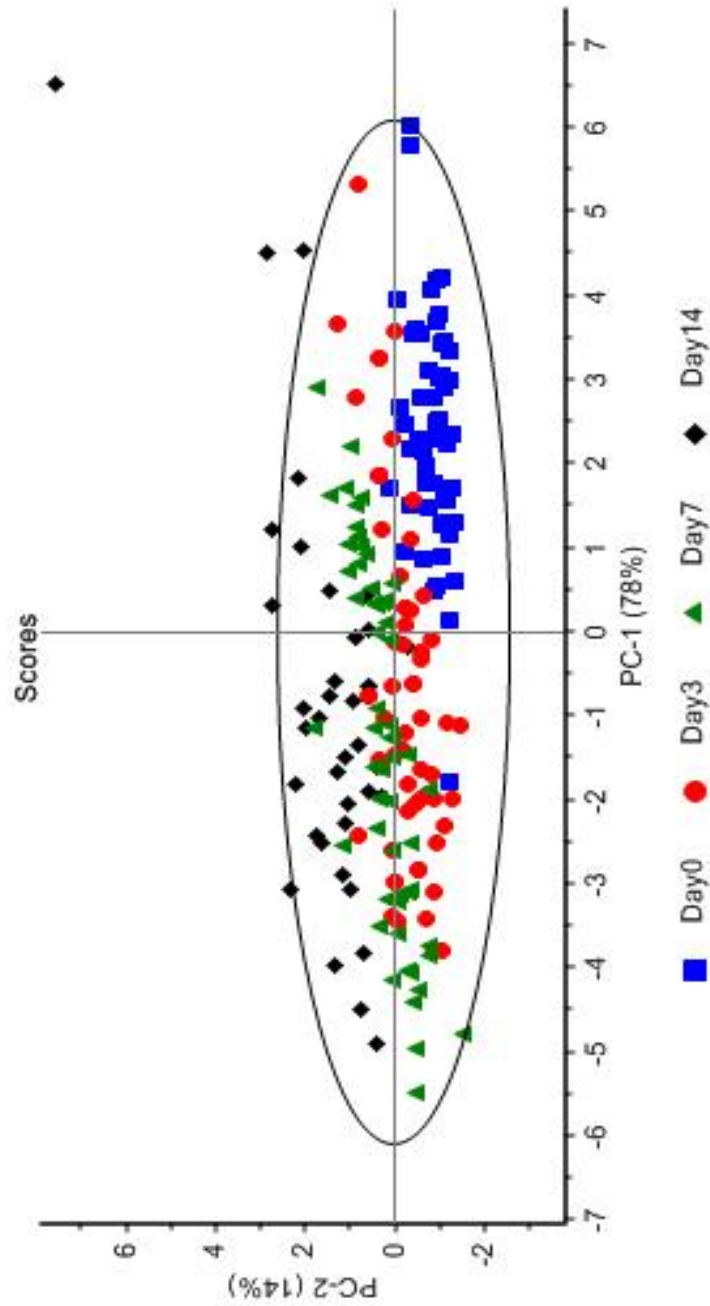


Figure 56. PCA of Amide III region in the papillary layer. All four time points were analysed in the same matrix. In this layer, groups are slightly separated from each other, starting with day 0 in the bottom right quadrant and ending with day 14 in the opposite quadrant.

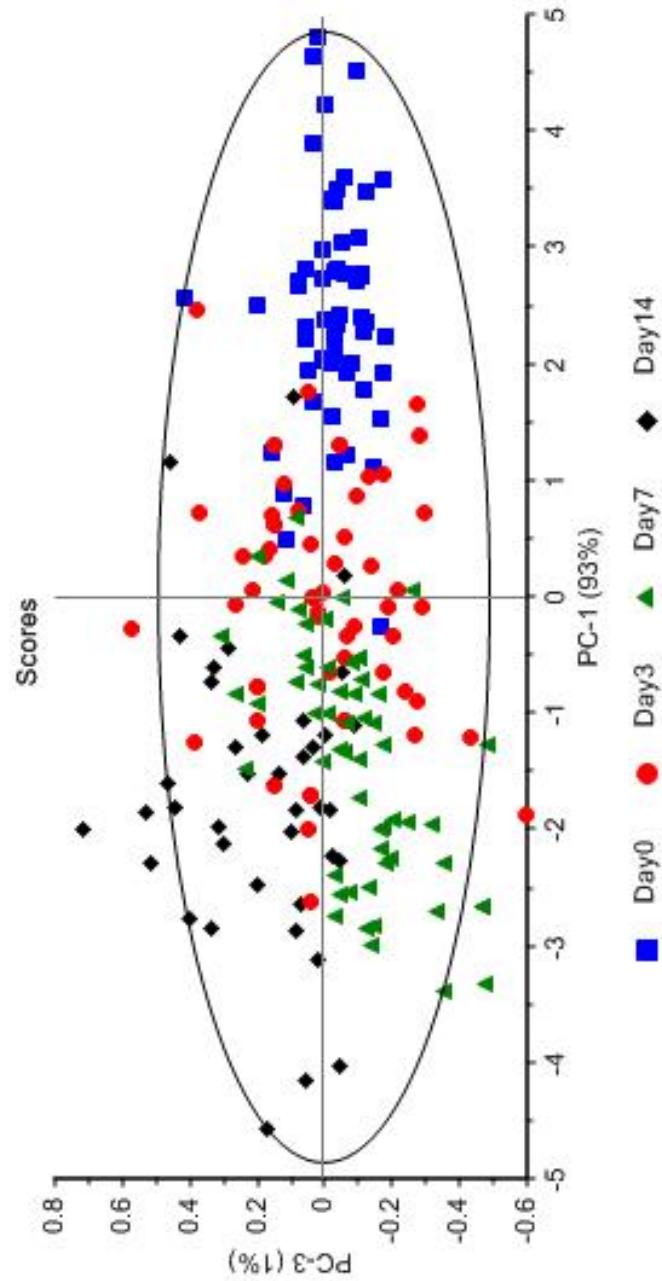


Figure 57. PCA of Amino acids region in the papillary layer. All four time points were analysed in the same matrix resulting in the separation of day 0 from day 3 and the rest of the groups.

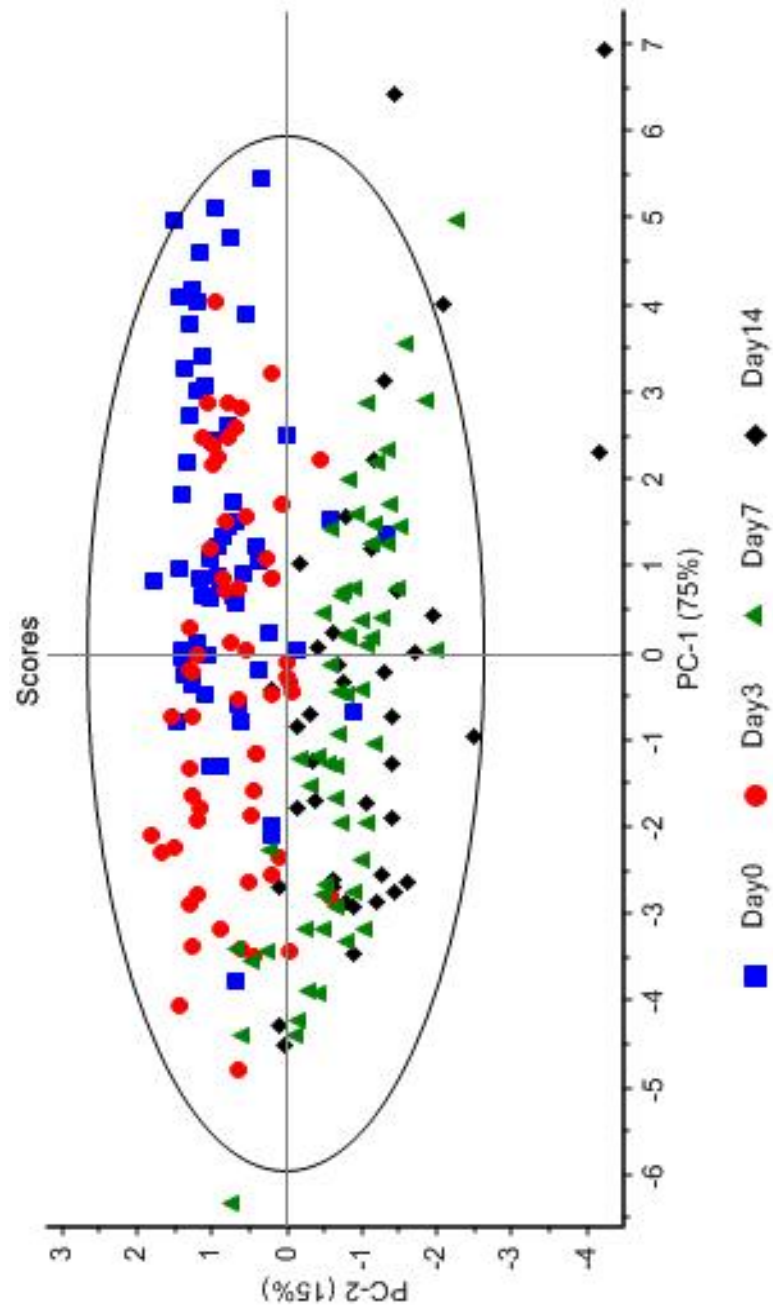


Figure 58. PCA of Amide III region in the reticular layer. All four time points were analysed in the same matrix resulting in the separation of day 0 and day 3 from day 7 and day 14 groups. In this layer, a more distinctive separation can be seen between day 3 and day 7.

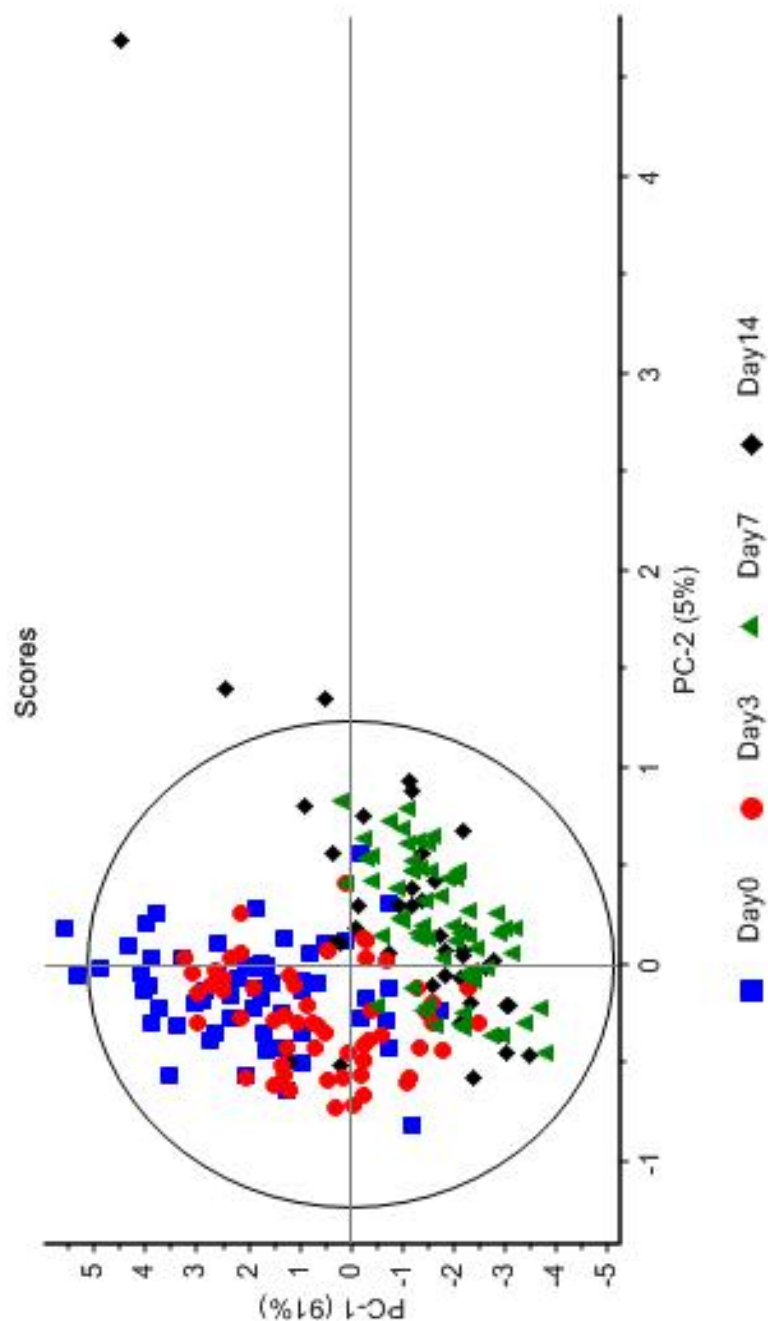


Figure 59. PCA of Amino acids region in the reticular layer. All four time points were analysed in the same matrix resulting in the separation of day 0 from day 3 and the rest of the groups. Responsible for this separation are peaks at 855 and 939 cm^{-1} .

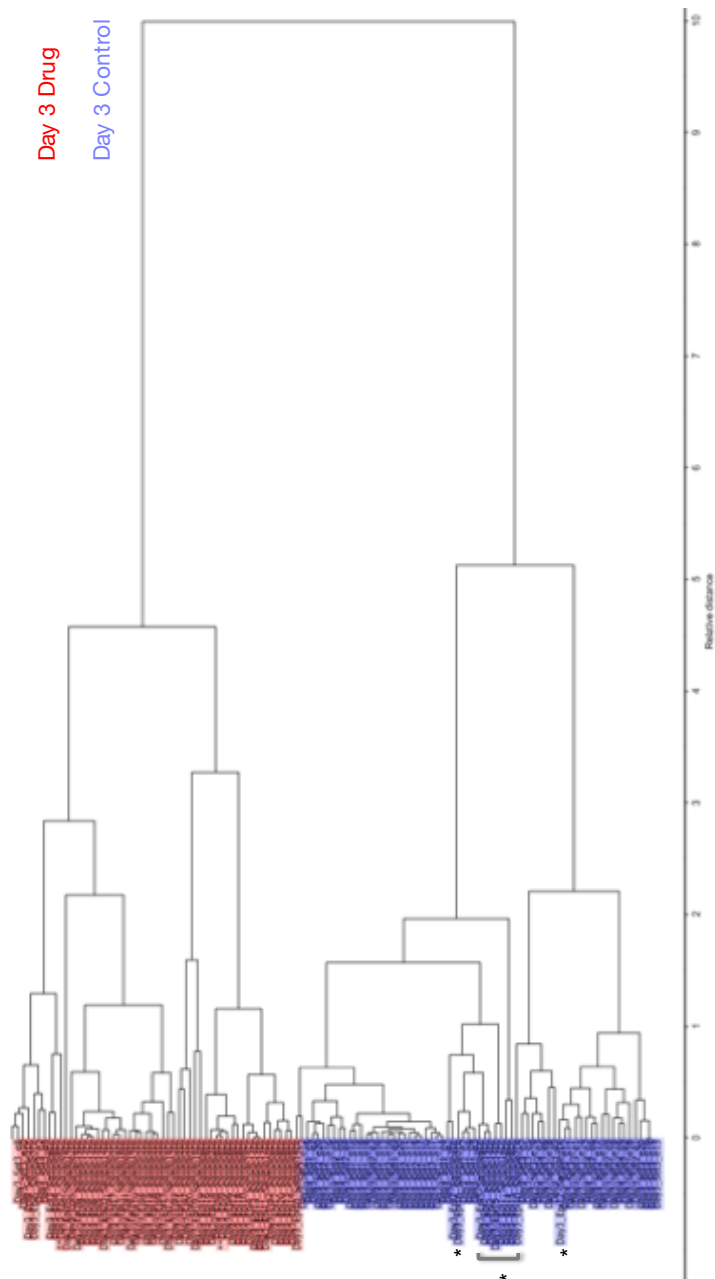


Figure 60. CA of Amide III region on Day 3 of contraction in both TEBM & TEBM/ β -APN groups. When analysing the amide III region, the unsupervised method clustered control data and separate it from drug group, complementing the results of the PCA.

10 REFERENCES

1. Squier, Christopher A. and Brogden, K. A. *Human oral mucosa; development, structure, and function*. **26**, (Ringgold Inc, 2011).
2. Moharamzadeh, K., Brook, I., Van Noort, R., Scutt, A. & Thornhill, M. Tissue-engineered Oral Mucosa: a Review of the Scientific Literature. doi:10.1177/154405910708600203
3. Bruch, J. M. & Treister, N. *Clinical Oral Medicine and Pathology*. (Springer International Publishing, 2017). doi:10.1007/978-3-319-29767-5
4. Yadev, N. P., Murdoch, C., Saville, S. P. & Thornhill, M. H. *Evaluation of tissue engineered models of the oral mucosa to investigate oral candidiasis*.
5. Chiego, D. J. *Essentials of oral histology and embryology: a clinical approach*.
6. Hand, A. R. & Frank, M. E. (Marion E. *Fundamentals of oral histology and physiology*.
7. Textbook of Oral Medicine - Google Books. Available at: <https://books.google.nl/books?hl=en&lr=&id=vxVPBQAAQBAJ&oi=fnd&pg=PP1&dq=Textbook+of+oral+medicine.+JP+Medical+Ltd.&ots=ZcZ0haKWx6&sig=JwTKQIMbZy8os6rO1vEbqH4cFiM#v=onepage&q=Textbook+of+oral+medicine.+JP+Medical+Ltd.&f=false>. (Accessed: 17th October 2018)
8. Carranza, F. A., Newman, M. G., Takei, H. H. & Klokkevold, P. R. *Carranza's clinical periodontology*. (Saunders Elsevier, 2006).
9. Gelse, K., Pöschl, E. & Aigner, T. Collagens - Structure, function, and biosynthesis. *Advanced Drug Delivery Reviews* **55**, 1531–1546 (2003).
10. Dee, K. C., Puleo, D. A. & Bizios, R. Protein-Surface Interactions. *An Introd. To Tissue-Biomaterial Interact.* 37–52 (2003). doi:10.1002/0471270598.ch3
11. Rashid, M. A., Khatib, F. & Sattar, A. Protein preliminaries and structure prediction fundamentals for computer scientists. (2015).
12. Shoulders, M. D. & Raines, R. T. Collagen Structure and Stability. *Annu. Rev. Biochem.* **78**, 929–958 (2010).
13. Ricard-Blum, S. & Ruggiero, F. The collagen superfamily: from the extracellular matrix to the cell membrane La superfamille des collagènes: de la matrice extracellulaire à la membrane cellulaire. *Pathol. Biol.* **53**, 430–442 (2005).
14. Glanvillc. *Structure and function of Collagen types*. (Academic Press, 2012).
15. Hay, E. D. & Hay, E. D. *Cell Biology of Extracellular Matrix*. (1991).
16. Ramachandran, G. N. *Biochemistry of Collagen*. (Plenum Press, 1976). doi:10.1007/978-1-4757-4602-0
17. Orgel, J. P. R. O., Irving, T. C., Miller, A. & Wess, T. J. Microfibrillar structure of type I collagen in situ. *Proc. Natl. Acad. Sci.* **103**, 9001–9005

- (2006).
18. R O Orgel, J. P., San Antonio, J. D. & Antipova, O. Molecular and structural mapping of collagen fibril interactions Molecular and structural mapping of collagen. *Connect. Tissue Res.* **52**, 2–17 (2011).
 19. Kalluri, R. Angiogenesis: Basement membranes: structure, assembly and role in tumour angiogenesis. *Nat. Rev. Cancer* **3**, 422–433 (2003).
 20. Caneló N, S. P. & Wallace, J. M. β -Aminopropionitrile-Induced Reduction in Enzymatic Crosslinking Causes In Vitro Changes in Collagen Morphology and Molecular Composition. (2016). doi:10.1371/journal
 21. Khmaladze, A. *et al.* Tissue-Engineered Constructs of Human Oral Mucosa Examined by Raman Spectroscopy. *Tissue Eng. Part C Methods* **19**, 299–306 (2013).
 22. Edwards, H. G. M. Modern Raman Spectroscopy—A Practical Approach. in *Journal of Raman Spectroscopy* **36**, 835–835 (2005).
 23. Nguyen, T. T. *et al.* Characterization of type I and IV collagens by Raman microspectroscopy: Identification of spectral markers of the dermo-epidermal junction. *Adv. Biomed. Spectrosc.* **7**, 105–110 (2013).
 24. Lo, W. L. *et al.* Raman spectroscopy monitoring of the cellular activities of a tissue-engineered ex vivo produced oral mucosal equivalent. *J. Raman Spectrosc.* **42**, 174–178 (2011).
 25. Dehring, K. A., Smukler, A. R., Roessler, B. J. & Morris, M. D. Correlating changes in collagen secondary structure with aging and defective type II collagen by Raman spectroscopy. *Appl. Spectrosc.* **60**, 366–372 (2006).
 26. Haka, A. S. *et al.* Diagnosing breast cancer by using Raman spectroscopy. *Proc. Natl. Acad. Sci. U. S. A.* **102**, 12371–6 (2005).
 27. Talari, A. C. S., Movasaghi, Z., Rehman, S. & Rehman, I. U. Raman spectroscopy of biological tissues. *Appl. Spectrosc. Rev.* **50**, 46–111 (2015).
 28. Huang, Z. *et al.* Near-infrared Raman spectroscopy for optical diagnosis of lung cancer. *Int. J. Cancer* **107**, 1047–1052 (2003).
 29. Nijssen, A. *et al.* Discriminating basal cell carcinoma from perilesional skin using high wave-number Raman spectroscopy. *J. Biomed. Opt.* **12**, 034004 (2007).
 30. Stone, N., Kendall, C., Smith, J., Crow, P. & Barr, H. Raman spectroscopy for identification of epithelial cancers. *Faraday Discuss.* **126**, 141–157 (2004).
 31. Pastar, I. *et al.* Epithelialization in Wound Healing: A Comprehensive Review. *Adv. Wound Care* **3**, 445–464 (2014).
 32. Martin, P. Wound Healing—Aiming for Perfect Skin Regeneration. *Science (80-.)*. **276**, 75–81 (1997).
 33. Broughton, G. I., Jeffrey Janis, U. E. & Attinger, C. E. The Basic Science of Wound Healing. doi:10.1097/01.prs.0000225430.42531.c2
 34. Werner, S. & Grose, R. Regulation of Wound Healing by Growth Factors and Cytokines. (2003). doi:10.1152/physrev.00031.2002
 35. Diegelmann, R. F. & Evans, M. C. *WOUND HEALING: AN OVERVIEW OF ACUTE, FIBROTIC AND DELAYED HEALING.* *Frontiers in Bioscience* **9**, (2004).



36. Larjava, H. *Oral wound healing : cell biology and clinical management*. (John Wiley & Sons, 2012).
37. Dam, A., Inger, J. S. & Lark, A. F. C. Cutaneous Wound Healing. *N. Engl. J. Med.* **341**, 738–746 (1999).
38. Lawrence Brown, B. F. *et al.* Expression of Vascular Permeability Factor (Vascular Endothelial Growth Factor) by Epidermal Keratinocytes during Wound Healing. doi:10.1084/jem.176.5.1375
39. Gabbiani, G. The myofibroblast in wound healing and fibrocontractive diseases. *J. Pathol.* **200**, 500–503 (2003).
40. Chakrabarty, K. H. *et al.* Keratinocyte-driven contraction of reconstructed human skin. *Wound Repair Regen.* **9**, 95–106 (2001).
41. Arwert, E. N., Hoste, E. & Watt, F. M. Epithelial stem cells, wound healing and cancer. *Nat. Rev. Cancer* **12**, 170–180 (2012).
42. Cristina, A. & Gonzalez, D. O. Wound Healing review. 614–620
43. Colthup, N. B., Daly, L. H. & Wiberley, S. E. *Introduction to infrared and Raman spectroscopy*. (Academic Press, 1975).
44. Rehman, I., Movasaghi, Z., Rehman, S., Movasaghi, Z. & Rehman, S. *Vibrational Spectroscopy for Tissue Analysis*. (CRC Press, 2012). doi:10.1201/b12949
45. Siesler, H. W. & Wiley InterScience (Online service). *Near-infrared spectroscopy: principles, instruments, applications*. (Wiley-VCH, 2002).
46. John R. Ferraro, Kazuo Nakamoto, C. W. B. *Introductory Raman Spectroscopy*. Elsevier, California **36**, (2003).
47. Coates, J. Vibrational Spectroscopy: Instrumentation for Infrared and Raman Spectroscopy*. *Appl. Spectrosc. Rev.* **33**, 267–425 (1998).
48. Baker, M. J. *et al.* Analyst CRITICAL REVIEW Clinical applications of infrared and Raman spectroscopy: state of play and future challenges. *Analyst* **143**, 1735 (2018).
49. Jermyn, M. *et al.* A review of Raman spectroscopy advances with an emphasis on clinical translation challenges in oncology. *Phys. Med. Biol.* **61**, R370–R400 (2016).
50. Wei, D. ; *et al.* Title Review of fluorescence suppression techniques in raman spectroscopy Review of Fluorescence Suppression Techniques in Raman Spectroscopy. (2015). doi:10.1080/05704928.2014.999936
51. Bonnier, F. *et al.* Analysis of human skin tissue by Raman microspectroscopy: Dealing with the background. *Vib. Spectrosc.* **61**, 124–132 (2012).
52. Wang, W., McGregor, H., Short, M. & Zeng, H. Clinical utility of Raman spectroscopy: current applications and ongoing developments. *Adv. Heal. Care Technol.* **13** (2016). doi:10.2147/ahct.s96486
53. Tampieri, A. *et al.* Biologically inspired synthesis of bone-like composite: Self-assembled collagen fibers/hydroxyapatite nanocrystals. *J. Biomed. Mater. Res.* **67A**, 618–625 (2003).
54. Ferrando, J. M. *et al.* Early imaging of integration response to polypropylene mesh in abdominal wall by environmental scanning electron microscopy: comparison of two placement techniques and correlation with tensiometric studies. *World J. Surg.* **25**, 840–7 (2001).
55. Detamore, M. S. *et al.* Quantitative analysis and comparative regional



- investigation of the extracellular matrix of the porcine temporomandibular joint disc. *Matrix Biol.* **24**, 45–57 (2005).
56. Baguneid, M. *et al.* Shear-stress preconditioning and tissue-engineering-based paradigms for generating arterial substitutes. *Biotechnol. Appl. Biochem.* **39**, 151 (2004).
 57. Cheng, Z. & Teoh, S.-H. Surface modification of ultra thin poly (epsilon-caprolactone) films using acrylic acid and collagen. *Biomaterials* **25**, 1991–2001 (2004).
 58. Habelitz, S., Balooch, M., Marshall, S. J., Balooch, G. & Marshall, G. W. In situ atomic force microscopy of partially demineralized human dentin collagen fibrils. *J. Struct. Biol.* **138**, 227–36 (2002).
 59. Xu, Y., Keene, D. R., Bujnicki, J. M., Höök, M. & Lukomski, S. Streptococcal Scl1 and Scl2 Proteins Form Collagen-like Triple Helices. *J. Biol. Chem.* **277**, 27312–27318 (2002).
 60. Mizuno, K., Hayashi, T., Peyton, D. H. & Bächinger, H. P. Hydroxylation-induced Stabilization of the Collagen Triple Helix. *J. Biol. Chem.* **279**, 38072–38078 (2004).
 61. Ramesh Babu, I. & Ganesh, K. N. Enhanced Triple Helix Stability of Collagen Peptides with 4R-Aminopropyl (Amp) Residues: Relative Roles of Electrostatic and Hydrogen Bonding Effects. *Annu. Rev. Biochem.* **64**, 2079–2080 (1995).
 62. Ellerbroek, S. M., Wu, Y. I. & Stack, M. S. Type I Collagen Stabilization of Matrix Metalloproteinase-2. (2001). doi:10.1006/abbi.2001.2345
 63. Eriksen, H. A. *et al.* Differently cross-linked and uncross-linked carboxy-terminal telopeptides of type I collagen in human mineralised bone. *Bone* **34**, 720–727 (2004).
 64. Brandt, J., Krogh, T. N., Jensen, C. H., Frederiksen, J. K. & Teisner, B. Thermal instability of the trimeric structure of the N-terminal propeptide of human procollagen type I in relation to assay technology. *Clin. Chem.* **45**, 47–53 (1999).
 65. Talari, A. C. S., Martinez, M. A. G., Movasaghi, Z., Rehman, S. & Rehman, I. U. Advances in Fourier transform infrared (FTIR) spectroscopy of biological tissues. *Appl. Spectrosc. Rev.* **52**, 456–506 (2017).
 66. Raman Spectroscopy of Biological Tissues. (2007). doi:10.1080/05704920701551530
 67. McColl, I. H. *et al.* A new perspective on ??-sheet structures using vibrational raman optical activity: From poly(L-lysine) to the prion protein. *J. Am. Chem. Soc.* **125**, 10019–10026 (2003).
 68. Riek, R., Hornemann, S., Wider, G., Glockshuber, R. & Wüthrich, K. NMR characterization of the full-length recombinant murine prion protein, *m* PrP(23-231). *FEBS Lett.* **413**, 282–288 (1997).
 69. Chou, P. Y. & Fasman, U. D. Prediction of protein conformation. *Biochemistry* **13**, 211–215 (1974).
 70. Jastrzebska, M., Wrzalik, R., Kocot, A., Zalewska-Rejda, J. & Cwalina, B. Journal of Biomaterials Science, Polymer Edition Raman spectroscopic study of glutaraldehyde-stabilized collagen and pericardium tissue Raman spectroscopic study of glutaraldehyde-stabilized collagen and pericardium tissue. *J. Biomater. Sci. Polym. Ed.*

- J. Biomater. Sci. Polym. Edn* **14**, 185–197 (2003).
71. Guilbert, M. *et al.* Probing non-enzymatic glycation of type I collagen: A novel approach using Raman and infrared biophotonic methods. *BBA - Gen. Subj.* **1830**, 3525–3531 (2013).
 72. Copeland, R. A. & Spiro, T. G. Ultraviolet Raman Hypochromism of the Tropomyosin Amide Ultraviolet Raman Hypochromism of the Tropomyosin Amide Protein. *J. Am. Chem. Soc.* **108**, 1281–1285 (1986).
 73. Gullekson, C., Lucas, L., Hewitt, K. & Kreplak, L. Surface-Sensitive Raman Spectroscopy of Collagen I Fibrils. *Biophysj* **100**, 1837–1845 (2011).
 74. Pande, J. *et al.* Raman, Infrared, and Circular Dichroism Spectroscopic Studies on Metallothionein: A Predominantly ‘Turn’-Containing Protein. *Biochem. Eur. J. Biochem. Eur. J. Biochem. J. Raman Spectrosc. Biopolym.* **25**, 5526–5532 (1986).
 75. Frushour, B. G. & Koenig, J. L. Raman scattering of collagen, gelatin, and elastin. *Biopolymers* **14**, 379–391 (1975).
 76. Gniadecka, M., Faurskov Nielsen, O., Christensen, D. H. & Wulf, H. C. Structure of Water, Proteins, and Lipids in Intact Human Skin, Hair, and Nail. (1998). doi:10.1046/j.1523-1747.1998.00146.x
 77. Ikoma, T., Kobayashi, H., Tanaka, J., Walsh, D. & Mann, S. Physical properties of type I collagen extracted from fish scales of *Pagrus major* and *Oreochromis niloticus*. *Int. J. Biol. Macromol.* **32**, 199–204 (2003).
 78. Bernerd, F. & Asselineau, D. UVA exposure of human skin reconstructed in vitro induces apoptosis of dermal fibroblasts: Subsequent connective tissue repair and implications in photoaging. *Cell Death Differ.* **5**, 792–802 (1998).
 79. Cowper, S. E. *et al.* Scleromyxoedema-like cutaneous diseases in renal-dialysis patients. *Lancet* **356**, 1000–1001 (2000).
 80. Zhang, Q. *et al.* Raman Microspectroscopic and Dynamic Vapor Sorption Characterization of Hydration in Collagen and Dermal Tissue. (2011). doi:10.1002/bip.21618
 81. Xiao, Y. *et al.* Wavelength-dependent conformational changes in collagen after mid-infrared laser ablation of cornea. *Biophys. J.* **94**, 1359–1366 (2008).
 82. Myllyharju, J. Intracellular post-translational modifications of collagens. *Top. Curr. Chem.* **247**, 115–147 (2005).
 83. Dyer, D. G. *et al.* Accumulation of Maillard Reaction Products in Skin Collagen in Diabetes and Aging. *Clin. Invest* **91**, 2463–2469 (1993).
 84. Ansari, N. A. & Rasheed, Z. Non-enzymatic glycation of proteins: From diabetes to cancer. *Biochem. Suppl. Ser. B Biomed. Chem.* **3**, 335–342 (2009).
 85. Ager, J. W., Nalla, I. R. K., Breeden, K. L. & Ritchie, R. O. Deep-ultraviolet Raman spectroscopy study of the effect of aging on human cortical bone. (2005). doi:10.1117/1.1924668
 86. Nguyen, T. T. *et al.* Raman comparison of skin dermis of different ages: Focus on spectral markers of collagen hydration. *J. Raman Spectrosc.* **44**, 1230–1237 (2013).
 87. Téllez S, C. A. Confocal Raman Spectroscopic Analysis of the Changes in Type I Collagen Resulting from Amide I Glycation. *Biomed. J. Sci.*

- Tech. Res.* **1**, (2017).
88. Fields, M., Spencer, N., Dudhia, J. & McMillan, P. F. Structural changes in cartilage and collagen studied by high temperature Raman spectroscopy. *Biopolymers* **107**, 1–8 (2017).
 89. Paschalis, E. P. *et al.* Spectroscopic Characterization of Collagen Cross-Links in Bone. *J. Bone Miner. Res.* **Volume 16**, 1739–1935 (2001).
 90. Buckley, K., Matousek, P., Parker, A. W. & Goodship, A. E. Raman spectroscopy reveals differences in collagen secondary structure which relate to the levels of mineralisation in bones that have evolved for different functions. *J. Raman Spectrosc.* **43**, 1237–1243 (2012).
 91. Zhang, Q. *et al.* Raman Microspectroscopic and Dynamic Vapor Sorption Characterization of Hydration in Collagen and Dermal Tissue. (2011). doi:10.1002/bip.21618
 92. Liu, H. *et al.* Raman spectroscopy combined with SHG gives a new perspective for rapid assessment of the collagen status in the healing of cutaneous wounds. *Anal. Methods* **8**, 3503–3510 (2016).
 93. Yan, W. *et al.* Raman spectroscopy enables noninvasive biochemical identification of the collagen regeneration in cutaneous wound healing of diabetic mice treated with MSCs. *Lasers Med. Sci.* **32**, 1131–1141 (2017).
 94. Sun, J. *et al.* Detection of Redox State Evolution during Wound Healing Process Based on a Redox-Sensitive Wound Dressing. *Anal. Chem.* **90**, 6660–6665 (2018).
 95. Pereira, L., Soto, C. A. T., Santos, L. Dos, Favero, P. P. & Martin, A. A. Confocal Raman Spectroscopy as an Optical Sensor to Detect Advanced Glycation End Products of the Skin Dermis. *Sens. Lett.* **13**, 791–801 (2015).
 96. Avery, N. C. & Bailey, A. J. The effects of the Maillard reaction on the physical properties and cell interactions of collagen. *Pathol. Biol.* **54**, 387–395 (2006).
 97. Dominguez, L. J., Barbagallo, M. & Moro, L. Collagen overglycosylation: A biochemical feature that may contribute to bone quality. (2005). doi:10.1016/j.bbrc.2005.02.050
 98. Peterkofsky, B. Ascorbate requirement for hydroxylation and secretion of procollagen: relationship to inhibition of collagen synthesis in scurvy. *Am. J. Clin. Nutr.* **54**, 1135S–1140S (1991).
 99. Mikulíková, K. *et al.* Advanced Glycation End-Product Pentosidine Accumulates in Various Tissues of Rats with High Fructose Intake. *Physiol. Res* **57**, 89–94 (2008).
 100. Eerola, I. *et al.* TYPE X COLLAGEN, A NATURAL COMPONENT OF MOUSE ARTICULAR CARTILAGE Association with Growth, Aging, and Osteoarthritis. *ARTHRITIS B KHkUMATISM* **41**, 1287–1295 (1998).
 101. Pizzo, S. V, Lehrman, M. A., Imber, M. J. & Guthrow, C. E. The clearance of glycoproteins in diabetic mice. *Biochem. Biophys. Res. Commun.* **101**, 704–708 (1981).
 102. Death, A. K., Fisher, E. J., McGrath, K. C. Y. & Yue, D. K. High glucose alters matrix metalloproteinase expression in two key vascular cells: Potential impact on atherosclerosis in diabetes. *Atherosclerosis* **168**,

- 263–269 (2003).
103. Meerwaldt, R. *et al.* The clinical relevance of assessing advanced glycation endproducts accumulation in diabetes. *Cardiovascular Diabetology* **7**, (2008).
 104. Lapolla, A., Mosca, A. & Fedele, D. The general use of glycated haemoglobin for the diagnosis of diabetes and other categories of glucose intolerance: Still a long way to go. (2011). doi:10.1016/j.numecd.2011.02.006
 105. Gkogkolou, Paraskevi & Bohm, M. Advanced Glycation end Products. (2017). doi:10.4161/derm.22028
 106. Mezentsev, A. V, Bruskin, S. A., Soboleva, A. G., Sobolev, V. V & Piruzian, E. S. Pharmacological Control of Receptor of Dvanced Glycation End-Products and its Biological Effects in Psoriasis. *Int J Biomed Sci www.ijbs.org* **9**, (2013).
 107. Van Zuijlen, P. P. M. *et al.* Collagen morphology in human skin and scar tissue: no adaptations in response to mechanical loading at joints. *Burns* **29**, 423–431 (2003).
 108. Verhaegen, P. D. H. M. *et al.* Differences in collagen architecture between keloid, hypertrophic scar, normotrophic scar, and normal skin: An objective histopathological analysis. *Wound Repair Regen.* **17**, 649–656 (2009).
 109. Forjuoh, S. N. Burns in low- and middle-income countries: A review of available literature on descriptive epidemiology, risk factors, treatment, and prevention. *Burns* **32**, 529–537 (2006).
 110. Peck, M. D., Kruger, G. E., van der Merwe, A. E., Godakumbura, W. & Ahuja, R. B. Burns and fires from non-electric domestic appliances in low and middle income countries. *Burns* **34**, 303–311 (2008).
 111. World Health Organization. The Global Burden of Disease: 2004 update. *2004 Updat.* 146 (2008). doi:10.1038/npp.2011.85
 112. Harrison, C. A. & MacNeil, S. The mechanism of skin graft contraction: An update on current research and potential future therapies. *Burns* **34**, 153–163 (2008).
 113. Harrison, C. A. *et al.* Use of an in Vitro Model of Tissue-Engineered Skin to Investigate the Mechanism of Skin Graft Contraction. *Tissue Eng.* **12**, 061004065151003 (2006).
 114. Tuszyński, N. G., Knight, L., Piperno, J. & Walsh. Structural Integration of Skin Equivalents Grafted to Lewis and Sprague-Dawley Rats. *J. Invest. Dermatol.* **81**, 429–436 (1983).
 115. Thornton, D. J. A., Harrison, C. A., Heaton, M. J., Bullock, A. J. & MacNeil, S. Inhibition of Keratinocyte-Driven Contraction of Tissue-Engineered Skin In Vitro by Calcium Chelation and Early Restraint But Not Submerged Culture. *J. Burn Care Res.* **29**, 369–377 (2008).
 116. Schneider, J. C., Holavanahalli, R., Helm, P., Goldstein, R. & Kowalske, K. Contractures in Burn Injury: Defining the Problem. *J. Burn Care Res.* **27**, 508–514 (2006).
 117. Osman, N. I., Hillary, C., Bullock, A. J., MacNeil, S. & Chapple, C. R. Tissue engineered buccal mucosa for urethroplasty: Progress and future directions. *Adv. Drug Deliv. Rev.* **82**, 69–76 (2015).
 118. Patterson, J. M., Bullock, A. J., MacNeil, S. & Chapple, C. R. Methods

- to reduce the contraction of tissue-engineered buccal mucosa for use in substitution urethroplasty. *Eur. Urol.* **60**, 856–861 (2011).
119. Bhargava, S., Patterson, J. M., Inman, R. D., MacNeil, S. & Chapple, C. R. Tissue-Engineered Buccal Mucosa Urethroplasty-Clinical Outcomes. *Eur. Urol.* **53**, 1263–1271 (2008).
 120. Bhargava, S. & Chapple, C. Tissue-engineered buccal mucosa for substitution urethroplasty. *BJU Int.* **93**, 807–11 (2004).
 121. Ueda, M. S., Kaneda, T. S., Nagayama, M. S. & Oka, T. S. CLINICAL EVALUATION OF REVERSED DERMIS GRAFT FOR RECONSTRUCTION OF ORAL MUCOSA. *Nagoya J. Med. Sci* **48**, 33–45 (1986).
 122. Freedlander, E. & Scheker, L. R. The long term results of intra-oral split-skin grafting. *Br. J. Plast. Surg.* **35**, 376–383 (1982).
 123. Huang-Lee, L. L. H., Cheung, D. T. & Nimni, M. E. Biochemical changes and cytotoxicity associated with the degradation of polymeric glutaraldehyde derived crosslinks. *J. Biomed. Mater. Res.* **24**, 1185–1201 (1990).
 124. Cheung, D. T. & Nimni, M. E. Mechanism of Crosslinking of Proteins by Glutaraldehyde I: Reaction with Model Compounds. *Connect. Tissue Res.* **10**, 187–199 (1982).
 125. Gniadecka, M. *et al.* Water and Protein Structure in Photoaged and Chronically Aged Skin. *J. Invest. Dermatol.* **111**, 1129–1133 (1998).
 126. Suh, H., Lee, W. K., Park, J. C. & Cho, B. K. Evaluation of the Degree of Cross-linking in UV Irradiated Porcine Valves. *Yonsei Med. J.* **40**, 159–165 (1999).
 127. Menter, J. M., Patta, A. M., Sayre, R. M., Dowdy, J. & Willis, I. Effect of UV irradiation on type I collagen fibril formation in neutral collagen solutions. *Photodermatol Photoimmunol Photomed* **17**, 114–120 (2001).
 128. Sionkowska, A. Modification of collagen films by ultraviolet irradiation.
 129. Behring, J., Junker, R., Walboomers, X. F., Chessnut, B. & Jansen, J. A. Toward guided tissue and bone regeneration: morphology, attachment, proliferation, and migration of cells cultured on collagen barrier membranes. A systematic review. *Odontology* **96**, 1–11 (2008).
 130. Chamberlain, L. J., Yannas, I. V, Hsu, H. P., Strichartz, G. & Spector, M. Collagen-GAG substrate enhances the quality of nerve regeneration through collagen tubes up to level of autograft. *Exp. Neurol.* **154**, 315–329 (1998).
 131. Hwang, Y. J. & Lyubovitsky, J. G. The structural analysis of three-dimensional fibrous collagen hydrogels by raman microspectroscopy. *Biopolymers* **99**, 349–356 (2013).
 132. Frushour, B. G. & Koenig, J. L. Raman Spectroscopic Study of Poly (P-benzyl-L- Aspartate) and Sequential Polypeptides. *Biopolymers* **14**, 2115–2135 (1975).
 133. Bonifacio, A. & Sergo, V. Effects of sample orientation in Raman microspectroscopy of collagen fibers and their impact on the interpretation of the amide III band. *Vib. Spectrosc.* **53**, 314–317 (2010).
 134. Jer Hwang, Y. *et al.* 013-Pos Board B799 The Effects of Zero-Length and Non-Zero Length Cross-Linking Reagents on the Optical Spectral Properties and Structures of Collagen Hydrogels 1014-Pos Board B800



- Phasor Analysis with a New Widefield Photon-Counting Flim Detector Measurements of Cell Mass Distribution during Cell Division with Quantitative Phase Microscopy. *Biophysj* **102**, 202a (2012).
135. Wang, Y.-N., Galiotis, C. & Bader, D. L. Determination of molecular changes in soft tissues under strain using laser Raman microscopy. *J. Biomech.* **33**, 483–486 (2000).
136. Hwang, Y. J., Granelli, J. & Lyubovitsky, J. G. Multiphoton optical image guided spectroscopy method for characterization of collagen-based materials modified by glycation. *Anal. Chem.* **83**, 200–206 (2011).
137. Yamauchi, M. & Sricholpech, M. Lysine post-translational modifications of collagen. *Essays Biochem.* **52**, 113–133 (2012).
138. Saito, M. & Marumo, K. Collagen cross-links as a determinant of bone quality: A possible explanation for bone fragility in aging, osteoporosis, and diabetes mellitus. *Osteoporosis International* **21**, 195–214 (2010).
139. Wallace, J. M., Ron, M. S. & Kohn, D. H. Short-Term Exercise In Mice Increases Tibial Post-Yield Mechanical Properties While Two Weeks of Latency Following Exercise Increases Tissue-Level Strength Running Title: Enhanced Post-Yield Properties with Exercise, Increased Tissue Strength With Latency Enhanced Post-Yield Properties with Exercise, Increased Tissue Strength With Latency. *Calcif Tissue Int. Apr* **184**, 297–304 (2009).
140. Hammond, M. A. & Wallace, J. M. Exercise prevents β -aminopropionitrile-induced morphological changes to type I collagen in murine bone. *Bonekey Rep.* **4**, 645 (2015).
141. Knott, L. & Bailey, A. J. Collagen cross-links in mineralizing tissues: A review of their chemistry, function, and clinical relevance. *Bone* **22**, 181–187 (1998).
142. Paschalis, E. P. *et al.* Lathyrism-induced alterations in collagen cross-links influence the mechanical properties of bone material without affecting the mineral. *Bone* **49**, 1232–1241 (2011).
143. Paschalis, E. P. *et al.* Distribution of Collagen Cross-Links in Normal Human Trabecular Bone. *J. Bone Miner. Res.* **18**, 1942–6 (2003).
144. Nyman, J. S. *et al.* AGE-RELATED EFFECT ON THE CONCENTRATION OF COLLAGEN CROSSLINKS IN HUMAN OSTEONAL AND INTERSTITIAL BONE TISSUE. *Bone* **39**, 1210–1217 (2006).
145. Paschalis, E. P. Fourier transform infrared analysis and bone. (2009). doi:10.1007/s00198-009-0857-6
146. Mandair, G. S. & Morris, M. D. Contributions of Raman spectroscopy to the understanding of bone strength. *Bonekey Rep.* **4**, 620 (2015).
147. Raghavan, M., Sahar, N. D., Kohn, D. H. & Morris, M. D. Age-specific profiles of tissue-level composition and mechanical properties in murine cortical bone. (2012). doi:10.1016/j.bone.2011.12.026
148. Gamsjaeger, S., Robins, S. P., Tatakis, D. N., Klaushofer, K. & Paschalis, E. P. Identification of Pyridinoline Trivalent Collagen Cross-Links by Raman Microspectroscopy. *Calcif. Tissue Int.* **100**, 565–574 (2017).
149. Robins, S. P. Biochemistry and functional significance of collagen cross-linking: Figure 1. *Biochem. Soc. Trans.* **35**, 849–852 (2007).
150. Eyre, D. R., Paz, M. A. & Gallop, P. M. CROSS-LINKING IN

- COLLAGEN AND ELASTIN. *Ann. Rev. Biochem* **53**, 717–48 (1984).
151. GOBERDHAN, N. J., DAWSON, R. A., FRKEDLANDER, E. & NEIL, S. M. A calmodulin-like protein as an extracellular mitogen for the keratinocyte. *Br. J. Dermatol.* **129**, 678–688 (1993).
 152. Rheinwald, J. G. & Green, H. Formation of a keratinizing epithelium in culture by a cloned cell line derived from a teratoma. *Cell* **6**, 317–330 (1975).
 153. Mian, S. A., Colley, H. E., Thornhill, M. H. & Rehman, I. u. Development of a Dewaxing Protocol for Tissue-Engineered Models of the Oral Mucosa Used for Raman Spectroscopic Analysis. *Appl. Spectrosc. Rev.* **49**, 614–617 (2014).
 154. Ponec *et al.* Triglyceride metabolism in human keratinocytes cultured at the air-liquid interface. *Arch. Dermatol. Res.* **287**, 723–730 (1995).
 155. Guilbert, M. *et al.* Probing non-enzymatic glycation of type I collagen: A novel approach using Raman and infrared biophotonic methods. (2013). doi:10.1016/j.bbagen.2013.01.016
 156. Rucker, R. B. *et al.* Copper , lysyl oxidase , and extracellular matrix protein. **67**, 996–1002 (1998).
 157. and, N. M. S. & Klinman*, J. P. 2,4,5-Trihydroxyphenylalanine Quinone Biogenesis in the Copper Amine Oxidase from *Hansenula polymorpha* with the Alternate Metal Nickel†. (2005). doi:10.1021/BI051176M
 158. Noblesse, E. *et al.* Lysyl Oxidase-Like and Lysyl Oxidase Are Present in the Dermis and Epidermis of a Skin Equivalent and in Human Skin and Are Associated to Elastic Fibers. *J Invest Dermatol* **122**, 621–630 (2004).
 159. Medalie, D. A. *et al.* DIFFERENCES IN DERMAL ANALOGS INFLUENCE SUBSEQUENT PIGMENTATION, EPIDERMAL DIFFERENTIATION, BASEMENT MEMBRANE, AND RETE RIDGE FORMATION OF TRANSPLANTED COMPOSITE SKIN GRAFTS1. *Transplantation* **64**, (1997).
 160. Boyce, S. T., Supp, A. P., Wickett, R. R., Hoath, S. B. & Warden, G. D. Assessment With the Dermal Torque Meter of Skin Pliability After Treatment of Burns With Cultured Skin Substitutes. *J. Burn Care & 21*, 55–63 (2000).
 161. Woodley, D. T., Yamauchi, M., Wynn, K. C., Mechanic, G. & Briggaman, R. A. Collagen Telopeptides (Cross-Linking Sites) Play a Role in Collagen Gel Lattice Contraction. *J. Invest. Dermatol.* **97**, 580–585 (1991).
 162. Giampuzzi, M. *et al.* Down-regulation of lysyl oxidase-induced tumorigenic transformation in NRK-49F cells characterized by constitutive activation of ras proto-oncogene. *J. Biol. Chem.* **276**, 29226–32 (2001).
 163. Redden, R. A. & Doolin, E. J. Collagen crosslinking and cell density have distinct effects on fibroblast-mediated contraction of collagen gels. *Ski. Res. Technol.* **9**, 290–293 (2003).
 164. Arem, A., Misiorowski, R. & Chvapil, M. Effects of Low-Dose BAPN on Wound Healing1.
 165. Hoffman, D. L., Owen, J. A. & Chvapil~, M. Healing of Skin Incision Wounds Treated with Topically Applied BAPN Free Base in the Rat1.
 166. Santos, C. R. & Schulze, A. Lipid metabolism in cancer. *FEBS J.* **279**,

- 2610–2623 (2012).
167. Huang, H. *et al.* BMP signaling pathway is required for commitment of C3H10T1/2 pluripotent stem cells to the adipocyte lineage. *Proc. Natl. Acad. Sci.* **106**, 12670–12675 (2009).
 168. Miana, M. *et al.* The lysyl oxidase inhibitor α -aminopropionitrile reduces body weight gain and improves the metabolic profile in diet-induced obesity in rats. *Dis. Model. Mech.* **8**, 543–551 (2015).
 169. Lakshmi, R. J. *et al.* Tissue Raman Spectroscopy for the Study of Radiation Damage: Brain Irradiation of Mice Tissue Raman Spectroscopy for the Study of Radiation Damage: Brain Irradiation of Mice. *Radiat. Res.* **157**, 175–182 (2002).
 170. Lau, D. P. *et al.* Raman spectroscopy for optical diagnosis in normal and cancerous tissue of the nasopharynx? preliminary findings. *Lasers Surg. Med.* **32**, 210–214 (2003).
 171. Heiden, M. G. Vander, Cantley, L. C. & Thompson, C. B. *Understanding the Warburg Effect: The Metabolic Requirements of Cell Proliferation. New Series* **324**, (2009).
 172. Liu, Y., Zuckier, L. S. & Ghesani, N. V. Dominant uptake of fatty acid over glucose by prostate cells: A potential new diagnostic and therapeutic approach. *Anticancer Res.* (2010).
 173. Price, D. T. *et al.* COMPARISON OF [18 F]FLUOROCHOLINE AND [18 F]FLUORODEOXYGLUCOSE FOR POSITRON EMISSION TOMOGRAPHY OF ANDROGEN DEPENDENT AND ANDROGEN INDEPENDENT PROSTATE CANCER. (2002).
 174. van B. Robertson, W. Metabolism of Collagen in Mammalian Tissues. *Biophys. J.* **4**, 93–106 (1964).
 175. Fioramonte, M. *et al.* Analysis of Secondary Structure in Proteins by Chemical Cross-Linking Coupled to Mass Spectrometry. doi:10.1002/pmic.201200040
 176. Dukor, R. K. *Vibrational Spectroscopy in the Detection of Cancer.*
 177. Nimni, M. E., Deshmukh, K., Gerth, N. & Bavetta, L. A. Changes in collagen metabolism associated with the administration of penicillamine and various amino and thiol compounds. *Biochem. Pharmacol.* **18**, 707–708 (1969).
 178. Jasin, H. E. & Ziff, M. Relationship Between Soluble Collagen and Urinary Hydroxyproline in the Lathyratic Rat. *Exp. Biol. Med.* **110**, 837–841 (1962).
 179. Irfan, M. Studies on factor V in animals. *J. Comp. Pathol.* **77**, 13–20 (1967).
 180. MARTIN, G. R., MERGENHAGEN, S. E. & PROCKOP, D. J. Influence of scurvy and lathyrism (odoratism) on hydroxyproline excretion. *Nature* **191**, 1008–9 (1961).
 181. Implications, C. Hydroxyproline and collagen metabolism. Clinical implications. *Ann Intern Med* **63**, 672–694 (1965).